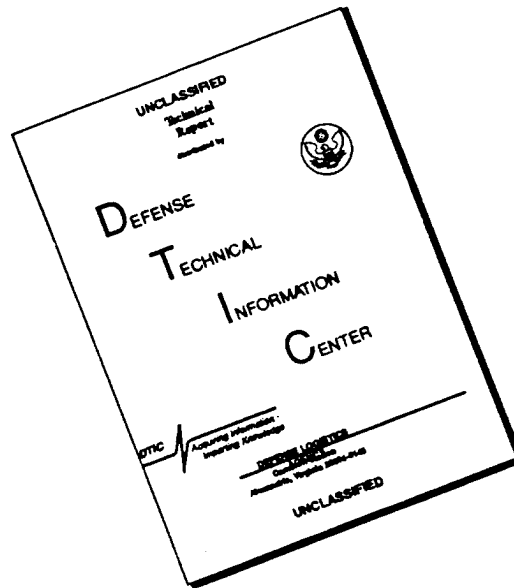




# DISCLAIMER NOTICE



THIS DOCUMENT IS BEST QUALITY AVAILABLE. THE COPY FURNISHED TO DTIC CONTAINED A SIGNIFICANT NUMBER OF PAGES WHICH DO NOT REPRODUCE LEGIBLY.

## GENERAL INSTRUCTIONS FOR COMPLETING SF 298

The Report Documentation Page (RDP) is used in announcing and cataloging reports. It is important that this information be consistent with the rest of the report, particularly the cover and title page. Instructions for filling in each block of the form follow. It is important to *stay within the lines* to meet *optical scanning requirements*.

**Block 1. Agency Use Only (Leave blank).**

**Block 2. Report Date.** Full publication date including day, month, and year, if available (e.g. 1 Jan 88). Must cite at least the year.

**Block 3. Type of Report and Dates Covered.** State whether report is interim, final, etc. If applicable, enter inclusive report dates (e.g. 10 Jun 87 - 30 Jun 88).

**Block 4. Title and Subtitle.** A title is taken from the part of the report that provides the most meaningful and complete information. When a report is prepared in more than one volume, repeat the primary title, add volume number, and include subtitle for the specific volume. On classified documents enter the title classification in parentheses.

**Block 5. Funding Numbers.** To include contract and grant numbers; may include program element number(s), project number(s), task number(s), and work unit number(s). Use the following labels:

<b>C</b> - Contract	<b>PR</b> - Project
<b>G</b> - Grant	<b>TA</b> - Task
<b>PE</b> - Program Element	<b>WU</b> - Work Unit Accession No.

**Block 6. Author(s).** Name(s) of person(s) responsible for writing the report, performing the research, or credited with the content of the report. If editor or compiler, this should follow the name(s).

**Block 7. Performing Organization Name(s) and Address(es).** Self-explanatory.

**Block 8. Performing Organization Report Number.** Enter the unique alphanumeric report number(s) assigned by the organization performing the report.

**Block 9. Sponsoring/Monitoring Agency Name(s) and Address(es).** Self-explanatory.

**Block 10. Sponsoring/Monitoring Agency Report Number.** (If known)

**Block 11. Supplementary Notes.** Enter information not included elsewhere such as: Prepared in cooperation with...; Trans. of...; To be published in.... When a report is revised, include a statement whether the new report supersedes or supplements the older report.

**Block 12a. Distribution/Availability Statement.** Denotes public availability or limitations. Cite any availability to the public. Enter additional limitations or special markings in all capitals (e.g. NOFORN, REL, ITAR).

**DOD** - See DoDD 5230.24, "Distribution Statements on Technical Documents."

**DOE** - See authorities.

**NASA** - See Handbook NHB 2200.2.

**NTIS** - Leave blank.

**Block 12b. Distribution Code.**

**DOD** - Leave blank.

**DOE** - Enter DOE distribution categories from the Standard Distribution for Unclassified Scientific and Technical Reports.

**NASA** - Leave blank.

**NTIS** - Leave blank.

**Block 13. Abstract.** Include a brief (*Maximum 200 words*) factual summary of the most significant information contained in the report.

**Block 14. Subject Terms.** Keywords or phrases identifying major subjects in the report.

**Block 15. Number of Pages.** Enter the total number of pages.

**Block 16. Price Code.** Enter appropriate price code (*NTIS only*).

**Blocks 17. - 19. Security Classifications.** Self-explanatory. Enter U.S. Security Classification in accordance with U.S. Security Regulations (i.e., UNCLASSIFIED). If form contains classified information, stamp classification on the top and bottom of the page.

**Block 20. Limitation of Abstract.** This block must be completed to assign a limitation to the abstract. Enter either UL (unlimited) or SAR (same as report). An entry in this block is necessary if the abstract is to be limited. If blank, the abstract is assumed to be unlimited.

**A RADIATIVE TRANSFER MODEL TO ANALYZE RADIOMETER  
DATA IN THE ATMOSPHERIC WINDOW**

by

**Keith James Duffy**

**A thesis submitted to the faculty of  
The University of Utah  
in partial fulfillment of the requirements for the degree of**

**Master of Science**

**Department of Meteorology**

**The University of Utah**

**March 1996**

**Copyright © Keith James Duffy 1996**

**All Rights Reserved**

## ABSTRACT

A radiation model was developed to calculate radiance in a plane parallel, vertically nonhomogeneous, nonscattering atmosphere. The radiance model was developed to analyze data collected by a vertically pointed radiometer with a receiver bandwidth of 9.5-11.5  $\mu\text{m}$ . These radiometer readings are used in conjunction with backscatter readings from a vertically aligned polarization diversity lidar system to compute various cirrus cloud properties such as infrared (IR) emittance. The model used the correlated k-distribution method (CKD) to calculate absorption coefficient functions and account for the nonhomogeneity of the atmosphere.

Transmittance and radiance results from this CKD model were compared with results from FASCODE3, a popular and highly accurate line-by-line (LBL) radiation model. Several different atmospheric profiles, ranging from subarctic to tropical, were compared to determine the accuracy and efficiency of the CKD model with respect to the LBL model. At the highest resolutions, the CKD model was 15-100 times faster than the LBL model. Despite the increased efficiency, the CKD model transmittance errors from the earth surface to 30 km were less than 0.4% with respect to the LBL model in temperate and arctic profiles. Errors were less than 2% in the tropical profile. The CKD model downwelling radiance errors from the surface to 30 km were less than 2% with respect to the LBL model for tropical and temperate profiles. In arctic conditions, radiance errors were as high as 8.5% below 2 km, but tapered off to 3% at cirrus cloud levels. In temperate atmospheres, the CKD model could be run as much as 300 times faster, while still calculating radiance values to within 0.6% of the LBL model.

levels. In temperate atmospheres, the CKD model could be run as much as 300 times faster, while still calculating radiance values to within 0.6% of the LBL model.

The study also showed that  $O_3$  and  $CO_2$  were important contributors to downwelling radiance in the atmospheric window region of the IR spectrum. Additionally, the study suggests that atmospheric emission from above typical cirrus cloud level also may be critical to the accurate calculation of downwelling radiance. These discoveries will potentially increase the accuracy of cirrus cloud emittance calculations since these factors were ignored in previous studies of this nature.

## TABLE OF CONTENTS

ABSTRACT .....	iv
LIST OF TABLES .....	viii
LIST OF FIGURES .....	ix
ACKNOWLEDGMENTS .....	xii
1. INTRODUCTION .....	1
1.1 The LIRAD Method .....	2
1.2 Applications of the LIRAD Method .....	7
1.3 The Correlated K-Distribution Method .....	8
1.4 Determining the Importance of Ozone Emission .....	9
1.5 Importance of the FARS LIRAD Study .....	12
2. THE LIRAD METHOD .....	15
2.1 The Lidar .....	15
2.2 The Infrared Radiometer .....	22
2.4 Summary .....	24
3. CALCULATION OF RADIANCE IN A NONHOMOGENEOUS ATMOSPHERE USING THE CORRELATED K-DISTRIBUTION METHOD .....	25
3.1 The Need for an Alternative to LBL Models .....	25
3.2 The K-Distribution Method in Homogeneous Atmospheres .....	27
3.3 Application of the K-Distribution Method to Nonhomogeneous Atmospheres .....	31
4. A DESCRIPTION OF THE FARS CORRELATED K-DISTRIBUTION MODEL .....	37
4.1 Model Features .....	38
4.2 Calculating IR Radiance with the FARS CKD Model .....	40
5. CKD MODEL PERFORMANCE VERSUS LINE-BY-LINE MODEL .....	61
5.1 Testing Methods .....	61
5.2 Transmittance Comparison .....	63



5.3 Radiance Comparisons.....	68
5.4 Upwelling Angle Varying Radiance Results.....	74
5.5 Emittance Results .....	76
5.6 G Resolution Sensitivity Test .....	82
5.7 Height Resolution Sensitivity Test.....	85
5.8 Above Cloud Contributions to Downwelling Radiance .....	86
6. CONCLUSIONS .....	89
REFERENCES.....	93

## LIST OF TABLES

<u>Table</u>	<u>Page</u>
3.1 Absorption Lines in the Atmospheric Window .....	26
3.2 CKD Model Pressure Levels .....	36
4.1 Parameters Contained in Absorption Coefficient Files .....	48
5.1 Individual Gas Transmittance Errors .....	64
5.2 Individual Gas Radiance Errors .....	69
5.3 Errors Resulting from Planck Function Approximations .....	74
5.4 Upwelling Radiance Varying Angle Test .....	75
5.5 Delta G Resolution Sensitivity Test .....	84
5.6 Height Resolution Sensitivity Test .....	85

## LIST OF FIGURES

<u>Figure</u>	<u>Page</u>
1.1 Time versus intensity diagram (bottom) of cloud and atmospheric backscatter coefficient for the afternoon of February 5, 1995, as recorded by the FARS ruby lidar system. Top portion show radiometric temperature at the same time as measured by the vertically oriented PRT-5 pyranometer. ....	4
1.2 Components of IR downward vertical radiation: (a) measured by a vertically pointing infrared radiometer ( $I_m$ ). $I_{ec}$ - radiance exiting the cloud base, $I_{cls}$ - radiance emitted by the clear atmosphere below ( $I_{bc}$ ), within ( $I_{aic}$ ), and above ( $I_{aac}$ ) the cloud, and (b) exiting the base of a typical cirrus cloud ( $I_{ec}$ ). $I_{ms}$ - radiance emitted non-vertically by the cloud but scattered into the radiometer's field of view (FOV). $I_c$ represents radiance emitted by the cloud in the downward vertical direction. $I_s$ represents radiance emitted by the earth's surface that is scattered by the cloud into the radiometer's FOV.....	6
1.3 Transmittance as a function of height in the 9.25-12.0 $\mu\text{m}$ spectral band for: (a) subarctic winter (SAW) profile, and (b) midlatitude summer (MLS) profile.....	10
1.4 Downwelling IR radiance in the atmospheric window region from the surface to 30 km at a spectral resolution of 0.004 $\text{cm}^{-1}$ . The normalized filter function of the FARS PRT-5 Pyranometer is superimposed. The higher radiance values in the 1000-1050 $\text{cm}^{-1}$ range is due to ozone emission.....	13
2.1 Illustration of a typical lidar backscatter profile. The lower curve represents the attenuated or measured lidar backscatter coefficient, while the upper curve represents the true or corrected backscatter coefficient. The shaded area represents the attenuated or measured integrated backscatter, while the area under the upper curve represents the true or corrected integrated backscatter.....	18
3.1 The CKD process. (a) Absorption coefficient as a function of $\nu$ for $\text{CO}_2$ at 100 mb and 220 K in the atmospheric window region of the IR spectrum. (b) Probability function $f(k)$ of the absorption coefficient. (c) Cumulative probability function, $g(k)$ , as a function of $k_\nu$ . (d) The inverse function of (c), the absorption coefficient as a function of the cumulative probability .....	29

3.2	Temperature and pressure dependence of the mass absorption coefficients, $k_v$ . (a) Temperature dependence of $k_v$ , for $\text{CO}_2$ in the atmospheric window region at 100 mb. The range of temperatures represents the extremes expected in the lower stratosphere and troposphere. (b) Pressure dependence of $k_v$ in the atmospheric window region at 220 K. The pressures represent the extreme upper and lower bounds of the area for this LIRAD study.....	34
4.1	Flow chart for the FARS CKD model radiative transfer solution process, outlining the major steps of calculating radiation. ....	41
4.2	Equivalent $k$ functions, $k(g)$ , and their finite representation by; (a) a low resolution CKD model, (b) a higher resolution model, and (c) a variable resolution model. ....	45
4.3	The wavenumber dependence of the Planck function over the bandwidth of the FARS IR radiometer for a range of tropospheric temperatures.....	56
4.4	Downwelling radiance as a function of wavenumber for the major gas emitters in the spectral region of the FARS IR radiometer. Although the magnitude of the radiances may vary considerably with pressure and temperature, the overall shape of the radiance function for each gas remains fairly constant. ....	57
4.5	Downwelling radiance for the major emitting gases ( $\text{H}_2\text{O}$ , $\text{CO}_2$ , $\text{O}_3$ , and water vapor continuum) in the spectral region of the FARS IR radiometer (see inserted filter function) for; (a) downwelling radiance in a midlatitude summer atmosphere, and (b) downwelling radiance in a subarctic winter atmospheric profile. The emission spectrum varies considerably for the combined gases. ....	59
5.1	Comparison of the FARS CKD and FASCODE3 LBL models transmittance calculations for; (a) subarctic winter, (b) US Standard, (c) midlatitude summer, and (d) tropical profiles.....	66
5.2	Transmittance errors from 0 to 30 km for the FARS CKD model for; (a) subarctic winter, (b) US Standard, (c) midlatitude summer, and (d) tropical profiles.....	67

5.3	Comparison of FARS CKD model and FASCODE3 LBL model downwelling radiance calculations for; (a) subarctic winter, (b) US Standard, (c) midlatitude summer, and (d) tropical profiles. ....	70
5.4	Downwelling vertical radiance errors from 0 to 30 km for the FARS CKD model for; (a) subarctic winter, (b) US Standard, (c) midlatitude summer, and (d) tropical profiles. ....	71
5.5	Emittance errors from the FARS CKD model for various emittances and typical cirrus cloud heights in a US Standard atmospheric profile. Cirrus mid-cloud heights are shown by the various lines (see inserted legend). ....	78
5.6	Emittance errors from the FARS CKD model for various emittances and typical cirrus cloud heights in a subarctic winter atmospheric profile. Cirrus mid-cloud heights are shown by the various lines (see inserted legend). ....	79
5.7	Emittance errors from the FARS CKD model for various emittances and typical cirrus cloud heights in a midlatitude summer atmospheric profile. Cirrus mid-cloud heights are shown by the various lines (see inserted legend)... ..	80
5.8	Contribution of downwelling vertical radiance from above cirrus cloud base for several different atmospheric profiles. Contributions are in percentage of total downwelling vertical radiance. ....	88

## **ACKNOWLEDGMENTS**

I would like to express my appreciation to Professor Ken Sassen for his guidance, support, and advice that made this research possible. I would also like to thank Dr. Krueger and Dr. Liou for their assistance. I would especially like to express my thanks to Professor Qiang Fu for all of the time he spent teaching me the finer points of atmospheric radiation and the CKD method, and for his guidance in general. Finally, I would like to thank Gina, my wife and inspiration, for the infinite amount of patience, love, and support she has provided me over the past few years.

The FARS cirrus cloud research program has been supported by Grants ATM-8914348 from the National Science Foundation and NAG-11314 from the National Aeronautics and Space Administration. Additional support for developing cirrus cloud property retrieval methods has come from Grant DEFG0394ER61747 from the Environmental Sciences Division of the Department of Energy, as part of the Atmospheric Radiation Measurement Programs.

## CHAPTER 1

### INTRODUCTION

Cirrus clouds play a major role in the radiative balance of the earth-atmosphere system (EAS). Climatological studies have shown that they cover approximately 20% of the earth and may exist over any part of the world. Unlike lower clouds, it is believed that, overall, cirrus may have a warming effect on the earth and its atmosphere. They reflect back into space some of the solar radiation that would otherwise warm the earth and its atmosphere. This process is often called the solar albedo effect, and it serves to cool the EAS. At the same time, due to their cold temperatures and location high in the atmosphere, they absorb the thermal infrared (IR) radiation emitted by the earth and lower atmosphere and re-emit much less. This reduces the amount of IR radiation lost to space and warms the EAS. This effect is commonly referred to as the greenhouse effect (Herman et al., 1980). The difference between the greenhouse effect and the solar albedo effect is the cloud radiative forcing (CRF). A positive CRF means that the net effect of the cloud is to warm the earth-atmosphere system. A negative CRF means that its net effect is to cool the earth-atmosphere system. (Platt and Gambling, 1971; Platt, 1973; Liou, 1980; and Liou, 1992).

A very important step in determining the radiative effects of a cloud is to determine its infrared (IR) emittance. It is generally believed that most lower water and mixed phase clouds are optically thick in the IR spectrum and thus have emittances approaching unity. The ability to assume that a cloud has an emittance of unity greatly simplifies the process of determining the CRF of that cloud. Cirrus clouds, on the other hand, have highly variable visible and IR optical properties. Available evidence suggests

that anvil cirrus may be a few kilometers thick and have IR emittances approaching unity, while thin sub-visual cirrus (i.e., invisible to the unaided eye) may have emittances of much less than 0.1 (Sassen and Cho, 1992).

Their highly variable nature causes great difficulty when incorporating cirrus clouds into climatic and global circulation models. The radiative parameterizations are mostly very crude and often represent large sources of error in prognostic models. One way to improve the cirrus cloud parameterizations would be to classify the clouds into several groups depending upon their origin, location, and microstructure. Each category could have its own parameterized emittance and albedo.

In order to do this properly, there must be a method of analyzing large volumes of cirrus data to ensure accuracy in the derived radiative properties of each category. Unfortunately, due to the nature of cirrus clouds, this is not any easy task. The high altitude of cirrus clouds makes them difficult to study using in-situ and many ground based remote sensing techniques. Additionally it is difficult to model their complicated scattering characteristics due to their irregular crystal structure of the particles. For these reasons the study of cirrus cloud radiative properties has, until recently, lagged significantly behind that of other types of clouds (Liou, 1986; Liou, 1992).

## **1.1 The LIRAD Method**

### **1.1.1 The LIDAR**

In the late 1970s C. M. R. Platt and colleagues of the Commonwealth Scientific and Industrial Research Organization (CSIRO) in Australia, devised a method using the combined measurements of ruby lidar and an infrared (10-12  $\mu\text{m}$ ) radiometer to derive various radiative properties of cirrus clouds including emittance. This technique is now known as the LIdar-RADiometer, or LIRAD, method. The lidar observations provide detailed information about visible characteristics of the cloud.



The most important value is the isotropic backscatter coefficient  $B'_c(\pi, z)$ , which must be corrected for in-cloud attenuation to obtain a detailed vertical profile of the corrected isotropic backscatter coefficient  $B_c(\pi, z)$ . This coefficient can be integrated vertically to obtain the total cloud visible backscatter,  $\gamma(\pi)$ , using techniques described later. Once the total backscatter of the cloud has been determined, the effective mid-cloud height can be found. Using the most representative radiosonde data, the temperature of the mid-cloud is determined. This temperature provides a close approximation of the blackbody temperature ( $I_{bb}$ ) of the cloud which is necessary in order to find the infrared emittance (Platt, 1973; Platt, 1979).

Figure 1.1 shows a typical 1-hour sampling of a cirrus cloud observed with a ruby ( $0.694 \mu\text{m}$ ) lidar at the Facility for Atmospheric Remote Sensing (FARS) in Salt Lake City, Utah (Sassen and Cho, 1992). This figure is a time versus height display of the visible backscatter intensity of a typical cirrus cloud. From this display many properties of the cloud can be observed. The displacement of the lidar trace from the background gives a relative indication of  $B_c(\pi, z)$ . Additionally, the cloud base, top, and thickness are readily apparent.

### 1.1.2 Infrared Radiative Properties

The infrared radiometer measures vertical downwelling radiance in the atmospheric window region of the IR spectrum. This measured radiance can be converted to a blackbody temperature through the Planck function. The top of Fig. 1.1 shows a 1-hour trace of the mid-infrared radiance measured by a PRT-5 pyranometer at the FARS facility. Note how the temperature varies over the period. At 21:30 UTC the cloud base is at 7 km and the measured radiative temperature is around  $-80^\circ\text{C}$ . Twenty-five minutes later at 21:55 UTC, the cloud base has dropped and the cloud has thickened considerably. By this time, the measured radiative temperature has increased to  $-40^\circ\text{C}$ . This is due to more IR

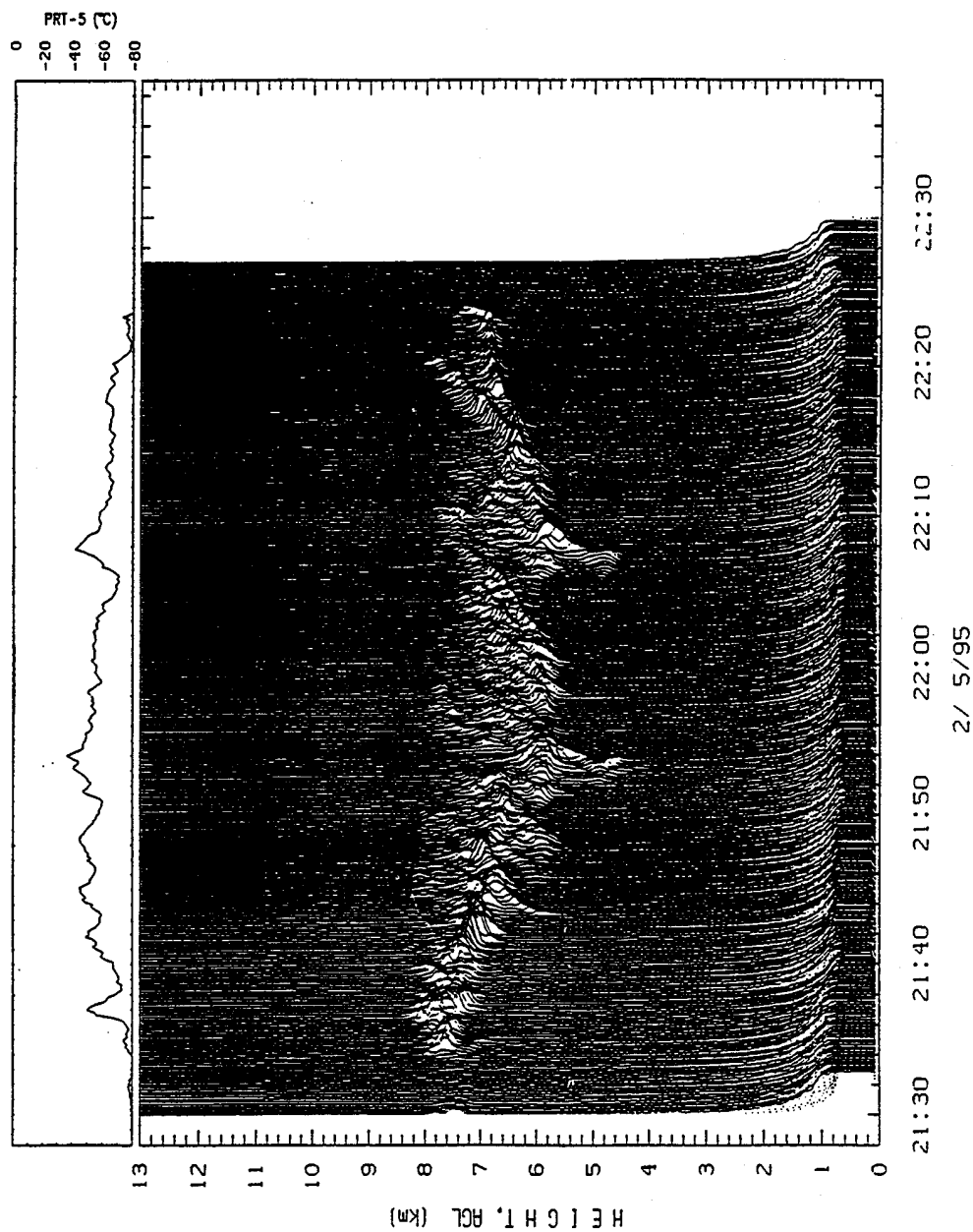


Figure 1.1. Time versus intensity diagram (bottom) of cloud and atmospheric backscatter coefficient for the evening of February 5, 1995 as recorded by the FARS ruby lidar system. Top portion shows radiometric temperature at the same time as measured by the vertically oriented PRT-5 pyranometer.

radiation being absorbed, emitted, and reflected back to the surface by the lower and thicker cirrus cloud. At the end of the period, the cirrus fibratus has left the radiometer field-of-view, revealing that the atmospheric background temperature is less than  $-80^{\circ}\text{C}$ . This quite cold, but not uncommon for an arid wintertime atmosphere.

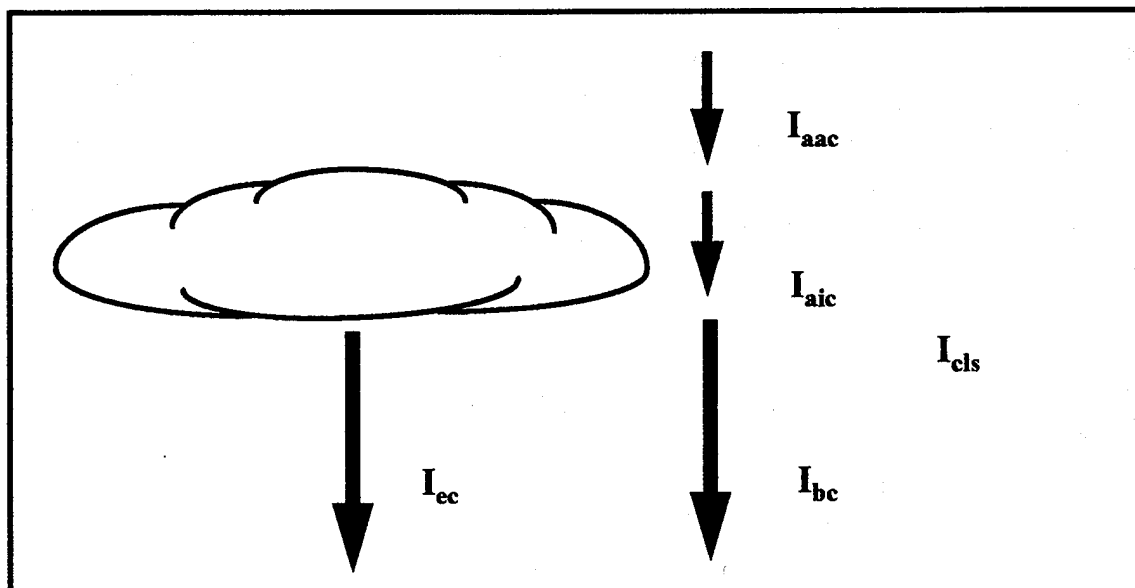
Figures 1.2a and 1.2b illustrate the different downwelling IR radiance components measured by such a radiometer. These components must be determined and subtracted from the measured IR radiance to obtain cloud radiance:

$$I_c = (I_m - I_{sr} \cdot T_{bc} - I_{aac} \cdot T_c - \phi \cdot I_{aic} - I_{bc}) / T_{bc}, \quad (1.1)$$

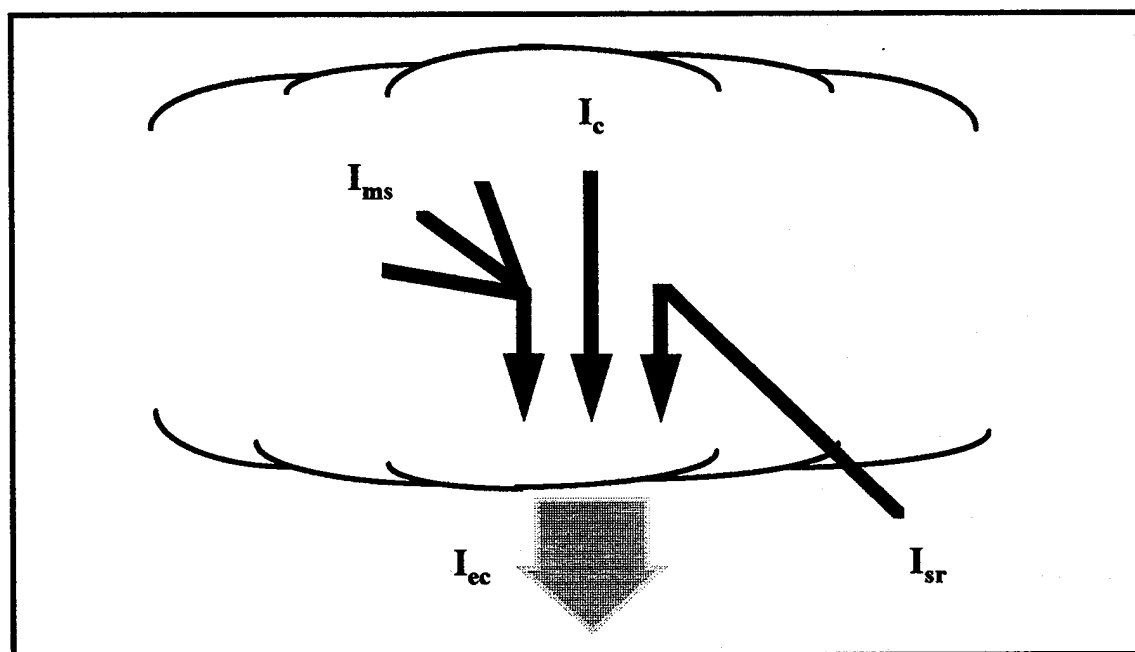
where  $I_c$  is the true cloud radiance;  $I_{sr}$  is the upwelling radiance from the surface of the earth that is scattered into the radiometer's field of view by the cirrus cloud;  $T_{bc}$  is the transmittance of the atmosphere below the cloud;  $I_{aac}$  is radiance that originates from above the cloud;  $T_c$  is the transmittance of the cloud particles;  $I_{aic}$  is the radiance that originates from the atmosphere between the top and the base of the cloud;  $\phi$  is a function that describes the attenuation of  $I_{aic}$  within the cloud itself, and  $I_{bc}$  is the radiance from below the cloud base. A derivation of Eq. (1.1) is provided in Chapter 2, and a description of how the components are obtained is provided in Chapter 4.

The primary purpose for using the LIRAD method here is to determine the absorption emittance of cirrus clouds,  $\varepsilon_a$ . The absorption emittance is the emittance due to absorption and emission of infrared radiation by cirrus cloud particles (i.e., it does not include scattering effects). The absorption emittance, which will from here on be represented by  $\varepsilon$ , is calculated simply by dividing the actual radiance,  $I_c$ , by the radiance of a blackbody emitter at the temperature of the cloud,  $I_{bb}$ :

$$\varepsilon = I_c / I_{bb}. \quad (1.2)$$



(a)



(b)

Figure 1.2. Components of IR downward vertical radiation: (a) measured by a vertically pointing infrared radiometer ( $I_m$ ).  $I_{ec}$  - radiance exiting the cloud base,  $I_{cls}$  - radiance emitted by the clear atmosphere below ( $I_{bc}$ ), within ( $I_{aic}$ ), and above ( $I_{aac}$ ) the cloud, and (b) exiting the base of a typical cirrus cloud ( $I_{ec}$ ).  $I_{ms}$  - radiance emitted non-vertically by the cloud but scattered into the radiometer's field of view (FOV).  $I_c$  represents radiance emitted by the cloud in the downward vertical direction.  $I_{sr}$  represents radiance emitted by the earth's surface that is scattered by the cloud into the radiometer's FOV.

## 1.2 Applications of the LIRAD Method

One of the eventual goals of the LIRAD study at FARS is to calculate cloud absorption emittance for many different classes of cirrus clouds. This requires construction of a radiative transfer model which reads the measured radiance from the PRT-5 radiometer, then, using current atmospheric soundings, calculates the quantities shown in Fig. 1.2a and 1.2b. These quantities are then subtracted from the measured downwelling vertical radiance as shown in Eq. (1.1). In order to do this, the radiative transfer model must not only compute absorption and emission by active gases, but it must also accurately model scattering by cirrus clouds without knowledge of the particle size distributions. The determination of cirrus cloud scattering properties is beyond the scope of this thesis and left for further study.

The principle purpose of this work is to build a clear-sky radiative transfer model that calculates the radiative quantities necessary to obtain cirrus cloud radiance. The model devised for this study calculates radiance and transmittance resulting from the emission and absorption of infrared radiation by the primary absorbing gases in the atmospheric window region. The primary absorbers/emitters in the operational mid-infrared window of the PRT-5 radiometer are water vapor, ozone, and carbon dioxide. This model has the ability to calculate the following components of Eq. (1.1),  $T_{bc}$ ,  $I_{aac}$ ,  $I_{aic}$ , and  $I_{bc}$ . Currently, various approaches are being considered to calculate the absorption and scattering quantities due to the cirrus cloud particles, themselves. When these two are combined, Eq. (1.2) will be solved, and the cirrus cloud emittance over the narrow spectral range of the radiometer will be known.

Obtaining the narrow band cirrus cloud absorption emittance is still only an intermediate step in deriving the most important radiative properties to be used in climatic studies. Two steps remain. This narrow band emittance must somehow be related to a broadband radiance, then converted to a flux value. Knowing the broadband flux of a

cloud provides all the information needed to understand the CRF. Detailed descriptions of how to derive the broadband radiative flux can be found in Platt and Dilley (1979) and Platt and Stephens (1980).

### 1.3 The Correlated K-Distribution Model

The most accurate way to calculate the clear-sky components of Figs. 1.2a and 1.2b is to use a line-by-line (LBL) model. A very sophisticated line-by-line model, such as the FASCODE models developed by the Air Force Geophysics Laboratory, can calculate atmospheric absorption and emission to a very high degree of accuracy (Clough et al., 1981; Clough et al., 1986; Clough et al. 1988; and Liou, 1992). However, this high degree of accuracy comes at a very large expense of time and computational power. Given the very large amount of data required to do meaningful studies of cirrus cloud emittance, the use of a sophisticated LBL model is not feasible. An alternate approach is needed to rapidly calculate absorption and emission without sacrificing too much accuracy. A relatively new approach for modeling atmospheric absorption and emission has this capability. This new method is called the correlated k-distribution (CKD) method. The correlated k-distribution method involves the spectral grouping of transmittances based on the absorption coefficient ( $k_v$ ) strengths (Goody et al., 1989; Lacis and Oinas, 1991; Fu, 1991; and Fu and Liou, 1992). It is described in Chapter 3.

Using this CKD method, a clear-sky radiative transfer model is constructed that calculates atmospheric transmittance as well as upwelling and downwelling radiances. Eventually, routines which simulate cirrus cloud scattering properties will be added to this CKD model providing a complete determination of cirrus cloud emittance. The CKD model is tailored to operate in the spectral band of the PRT-5 radiometer (9.25-12.0  $\mu\text{m}$ ) throughout the troposphere and lower stratosphere (0-30 km). A more detailed description of this model is presented in Chapter 4.

This model is tested against the FASCODE3 model for accuracy, and the results of this test are presented in Chapter 5. In addition to accuracy tests, the CKD model is run at several height and spectral resolutions to determine the optimal configuration for the purposes of the LIRAD study.

### 1.4 Determining the Importance of Ozone Emission

During the cirrus cloud emittance studies of Platt and colleagues, one important assumption was made that may not be applicable to the FARS research. Platt assumed that atmospheric emission from above the cirrus cloud base was negligible (Platt, 1973). This greatly simplified the computation of the cloud radiance in Eq. (1.1), reducing it to:

$$I_c = (I_m - I_{sr} T_{bc} - I_{bc}) / T_{bc} \quad (1.3)$$

This assumption was probably appropriate for his work, but it may not be appropriate in the FARS study for two reasons. First, FARS resides in a semi-arid region at high elevation (1520 m above mean sea level), while the CSIRO studies were all done in at a much lower elevation in a climate that tends to have much more water vapor in the atmosphere. Most water vapor resides in the lower troposphere while most ozone resides at 15-35 km above the earth's surface. Because the CSIRO site is located near a large body of water, the water vapor line and continuum absorption is likely to dominate over ozone emission. This is not necessarily the case however at the FARS site. Thus, because of the high altitude and relative lack of water vapor above the FARS site, ozone emission is more likely to be an important emitter of downwelling radiance.

Ozone emission is even more important in winter months when there is less water vapor in the atmosphere. This is clearly illustrated by Figs. 1.3a and 1.3b. Figure 1.3a shows the relative transmittances of O<sub>3</sub>, CO<sub>2</sub>, and H<sub>2</sub>O for a subarctic winter (SAW) profile. Ozone is clearly the dominant absorber here except in the bottom few kilometers

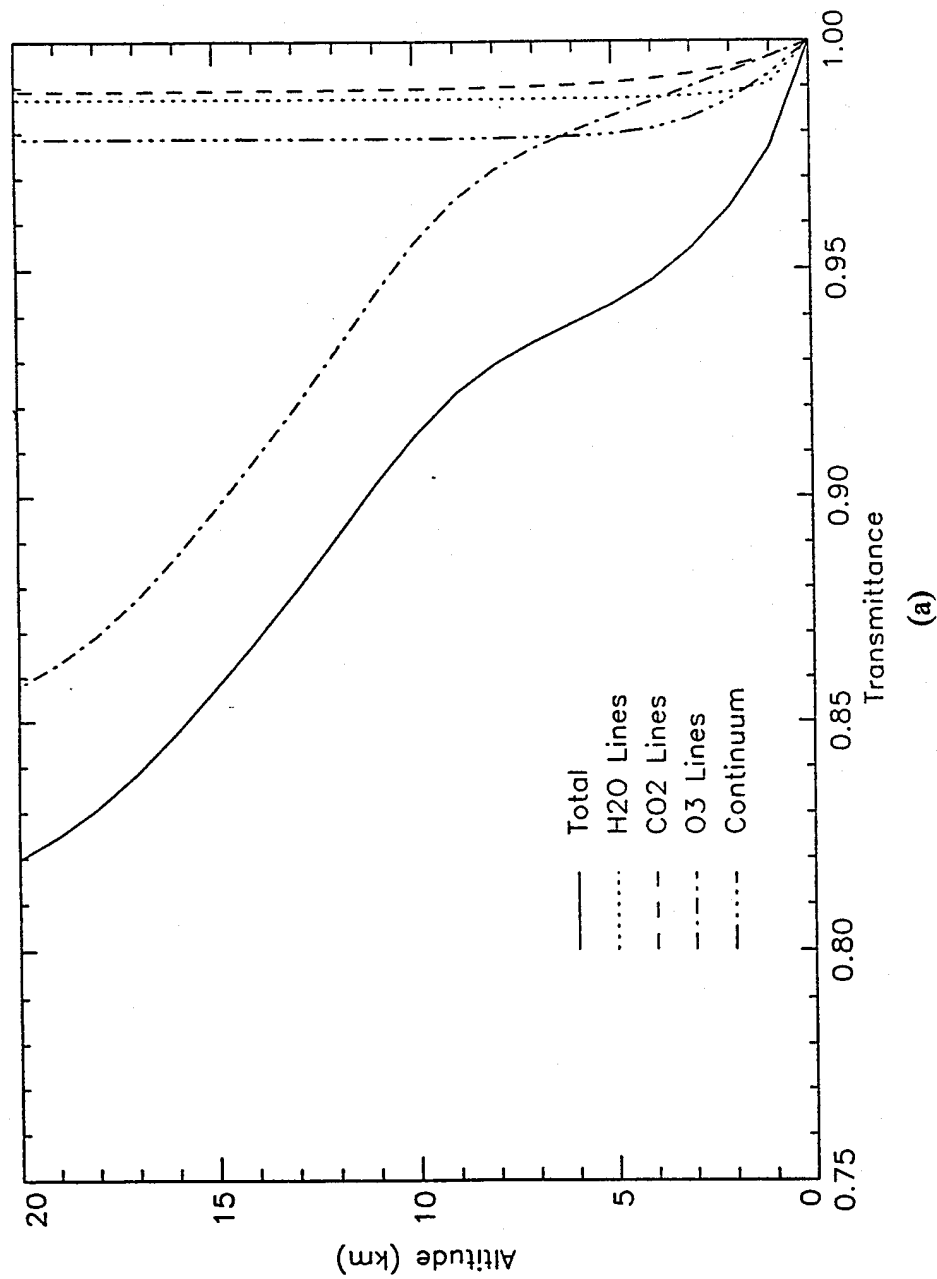


Figure 1.3. Transmittance as a function of height in the 9.25-12.0  $\mu\text{m}$  spectral band for: (a) subarctic winter (SAW) profile, and (b) midlatitude summer (MLS) profile.



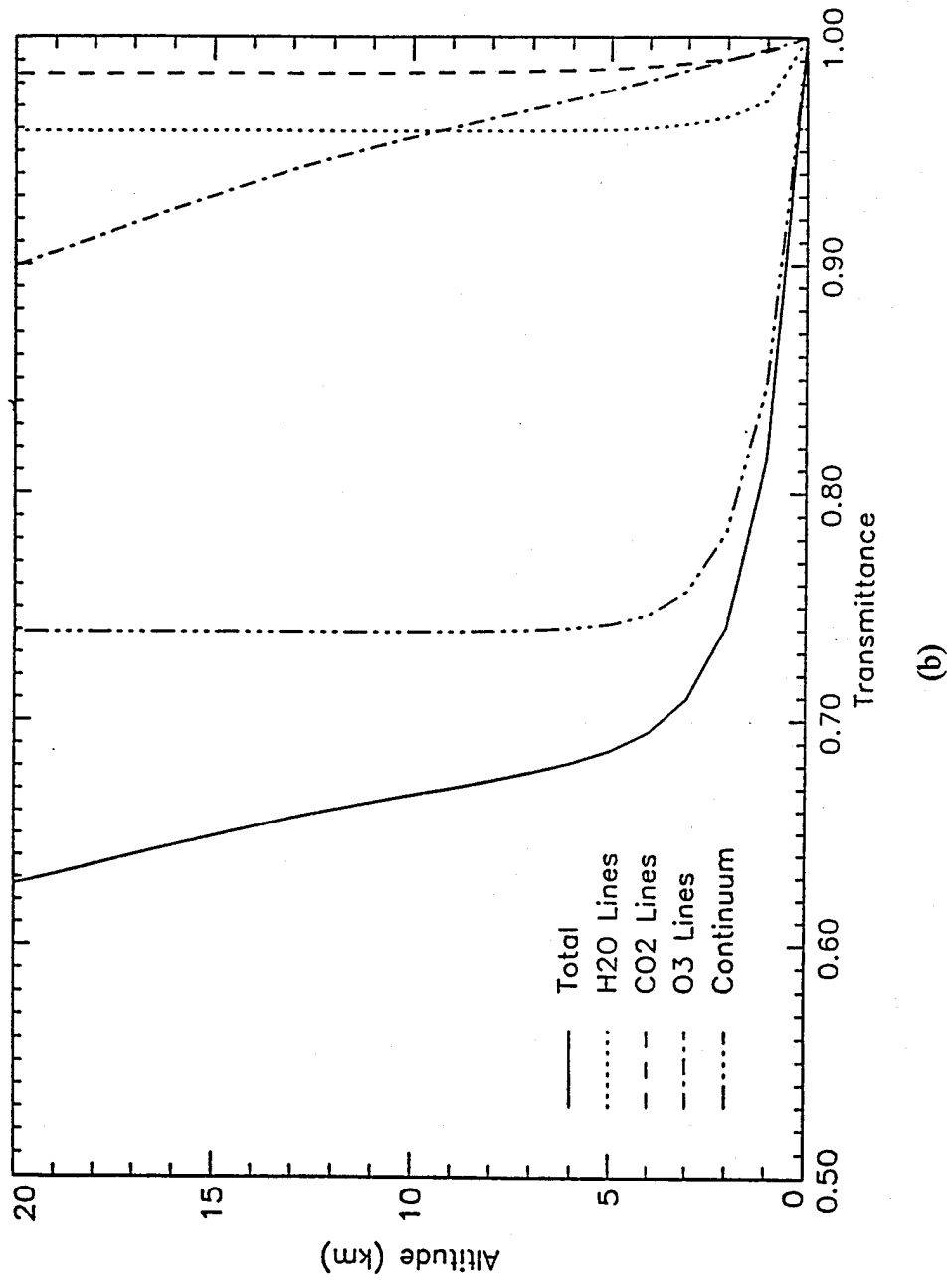


Figure 1.3 (continued)

of the atmosphere. The increased ozone absorption in this atmosphere is due to both the higher latitude and the lack of water vapor in the cold environment. Additionally, the concentration of ozone is higher in the winter. Figure 1.3b shows a mid-latitude summer (MLS) profile. Notice that the continuum absorption dominates absorption by all of the other species (Gallery et al., 1983; Anderson et al., 1986).

The other reason that Eq. (1.3) may not be appropriate for analysis of data from the FARS radiometer is that it appears to have a slightly different filter window than the radiometer used by Platt. The exact bandwidth of the radiometer used by Platt is not known to the author but was quoted as 10-12  $\mu\text{m}$  in Platt (1973) and Platt and Dilley (1979). Since the atmospheric window ozone band is centered at 9.6  $\mu\text{m}$  and ozone emission becomes negligible at wavelengths greater than 10.1  $\mu\text{m}$ , Platt's radiometer was not likely sensitive to ozone emission. The PRT-5 radiometer has a bandwidth of 9.25-12.0  $\mu\text{m}$  (833-1081  $\text{cm}^{-1}$ ). Figure 1.4 shows the filter function of the PRT-5 superimposed on a typical ozone emission spectrum. Although the ozone band is only on the edge of the PRT-5 window, it can still contribute significantly to radiances measured by that instrument under some conditions. For this reason it is unlikely that ozone can be ignored in the FARS study. Since regular ozone profiles are not available in most parts of the world, it is not possible to precisely calculate ozone emission at our location. Using standard atmospheric ozone profiles in conjunction with radiosonde data, one can determine whether or not ozone is a major contributor to downwelling atmospheric radiance at the surface. A brief experiment is presented at the end of Chapter 5 to determine whether or not ozone emission can be neglected.

### 1.5 Importance of the FARS LIRAD Study

The CSIRO LIRAD studies have opened the door to better understanding high cloud radiative parameters. There is, however, much to be gained by repeating and improving upon methods used during the CSIRO experiments. Advances in technology

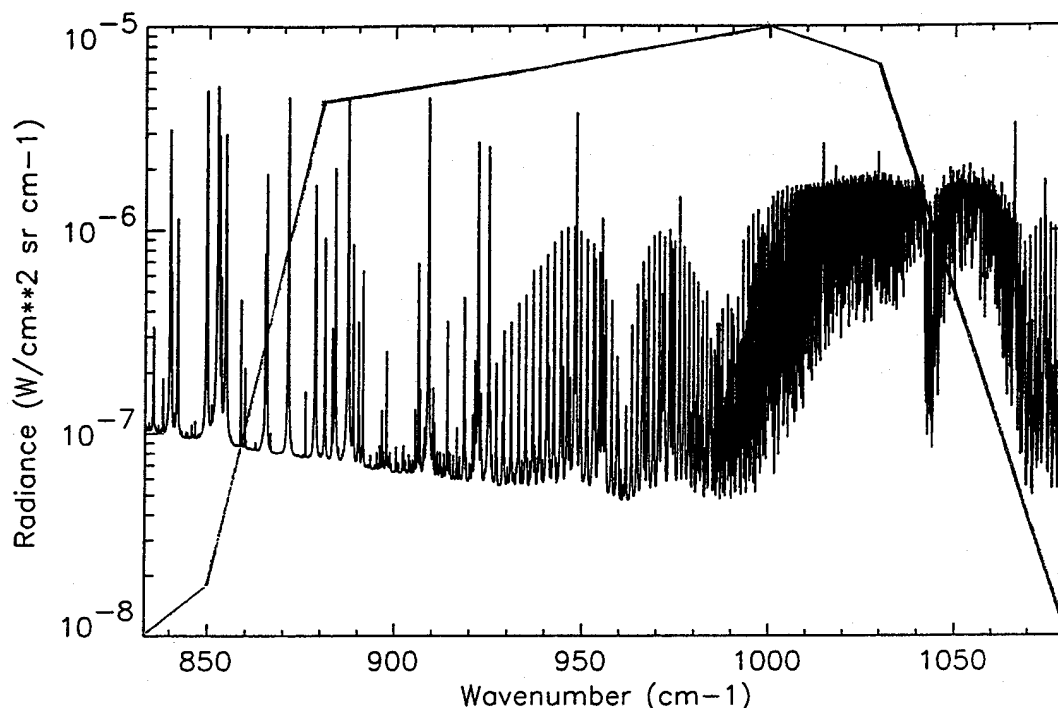


Figure 1.4. Downwelling IR radiance in the atmospheric window region from the surface to 30 km at a spectral resolution of  $0.004 \text{ cm}^{-1}$ . The normalized filter function of the FARS PRT-5 Pyranometer is superimposed. The higher radiance values in the  $1000\text{--}1050 \text{ cm}^{-1}$  range is due to ozone emission.

over the last decade have increased the accuracy of lidar and radiometer measurements. Additionally the YAG lidar system at FARS samples at a rate of 10 per second, much faster than the system used in the CSIRO experiments. This combined with thousands of hours of observation has resulted in a vast amount of cirrus cloud data available for study. These very large databases are necessary to conduct meaningful research due to the highly variable structures of various types of cirrus clouds.

Furthermore, the location of FARS is advantageous. As previously mentioned, the Facility for Atmospheric Remote Sensing resides in an arid region with relatively little atmospheric water vapor. The CSIRO facility on the other hand is located in a much more humid environment. As water vapor is a major emitter in the atmospheric window region,

this drier environment will lead to a lower background temperature for the IR radiometer. Lower background temperatures allow the IR radiometer to better detect thin cirrus.

Importantly, preliminary FARS data analysis has indicated that our local cirrus clouds appear to differ significantly from their counterparts in Australia and elsewhere (Sassen and Cho, 1992). Improvements to the models used to derive cloud scattering and atmospheric transmission should also lead to more accurate values of cirrus cloud emittance. Recent studies have shown that the CKD is an accurate method for calculating radiation in the 9.6  $\mu\text{m}$  ozone band where other methods fail. The radiative transfer model used in this study to calculate cirrus cloud radiance utilizes the CKD method. A combination of the above factors should allow the FARS LIRAD study to extend and improve upon the works of Platt and colleagues. Eventually, results from this study should lead to improvements in the cloud parameterizations used in general circulation models (GCM's). Observations at the FARS facility are also being used to test and improve satellite retrieval algorithms (Sassen and Cho, 1992).

## CHAPTER 2

### THE LIRAD METHOD

Chapter 1 briefly described the method of deriving the absorption emittance of a cirrus cloud. Equation 1.1 demonstrated that the narrow band emittance is simply found by dividing the actual cloud emittance ( $I_c$ ) by the blackbody emittance ( $I_{bb}$ ) of the cloud. This chapter describes in more detail how the components of  $I_c$  and  $I_{bb}$  are measured and derived. Detailed descriptions of the LIRAD method can be found in the series of papers by Platt et al. on the subject from 1971 through 1987. Several of these have already been mentioned, and for completeness, the others include Platt (1981), Platt and Dilley (1979), and Platt et al. (1987). A more detailed description of the radiative transfer model used to derive the components of  $I_{bb}$  is provided in Chapter 4.

#### 2.1 The Lidar

Lidar, which stands for Light Detection And Ranging, has been established as a very useful tool in the interrogation of the structure of cirrus clouds. The concentrated power of the laser beam allows the lidar to sample a relatively small volume even at heights up to 15 km. Additionally, unlike most low and mid-level clouds, the lidar pulse can usually penetrate an entire cirrus deck. This is due to the fact that cirrus clouds typically have much smaller particle concentrations than lower clouds. A typical cirrus has an ice water content of  $0.01\text{--}0.20\text{ g m}^{-3}$ , while a typical altocumulus or stratus deck has a liquid water content of  $0.20\text{--}0.50\text{ g m}^{-3}$  (Heymsfield and Platt, 1984). The size of the ice crystals in cirrus also contributes. Except in highly convective clouds, cloud droplets rarely exceed a radius of  $20\text{ }\mu\text{m}$ . Cirrus crystals on the other hand often have dimensions

from 20-1000  $\mu\text{m}$  (Liou, 1992). These larger particles scatter more energy in the forward direction. Polarization lidar, such as the ones at FARS, can also be used to discriminate between clouds in the liquid, mixed, and ice phases (Sassen, 1991). In the FARS LIRAD experiments, the lidar is simply used to find the effective mid-cloud height.

### 2.1.1 Instrumentation

The Facility for Atmospheric Remote Sensing, located near the edge of the University of Utah campus in Salt Lake City, Utah, currently has two polarization lidar systems. The first is a ruby polarization lidar which emits a maximum of 1.5 Joules at 0.694  $\mu\text{m}$ . The ruby lidar has a pulse rate frequency (PRF) of 0.1 Hz, a maximum range resolution of 7.5 m, and a narrow 1-3 mrad beamwidth. The second is a Nd:YAG polarization lidar system which emits up to 0.45 Joules at both 0.532  $\mu\text{m}$  and 1.06  $\mu\text{m}$ . This two color lidar system has a 0.5 mrad beamwidth, a maximum range resolution of 1.5 m, and a PRF of 10 Hz. The Nd:YAG system is mobile and has been used in field experiments such as the Atmospheric Radiation Measurement Program Intensive Observation Period conducted near Lamont, OK, in April 1994. The profiles shown in Fig. 1.1 are from the slower ruby lidar system.

### 2.1.2 Deriving the Blackbody Temperature

In order to solve for  $\epsilon$ , an accurate blackbody radiance is necessary. To get this value, a representative temperature of the cloud must be determined. A representative cloud height is determined from the lidar backscatter profile and then combined with atmospheric sounding data to obtain a representative cloud temperature. Depending on the desired accuracy, finding a cloud's blackbody temperature could be quite easy or very complicated. To a first approximation, one could simply use the temperature at the base of the cloud to calculate  $I_{bb}$ . This would be acceptable for a thin dense cloud, but would cause unacceptable errors in a cloud kilometers thick. A better method would be to note

the cloud base and top from the backscatter profiles and then use the mid-cloud height to find the temperature. The most accurate method would be to find the *effective* mid-cloud height to get the temperature. Finding the effective mid-cloud height is much more complicated. A brief explanation of how the effective mid-cloud height is determined follows.

Figure 2.1 is a representation of what a typical cirrus cloud visible backscatter profile might look like. Typically there is a strong low level return due to Rayleigh molecular and aerosols scattering off of particles in the boundary layer. This signal is usually ignored or gated out. As the distance increases and air density decreases, the return signal drops off dramatically until a cloud is observed. The point at which the return begins to increase again marks the cloud base height. It is clearly visible in Fig 2.1 as well as Fig 1.1. The displacement of the return signal from the z-axis at a given height represents the backscatter coefficient at that height. The higher of the two values in Fig. 2.1 is the true backscatter coefficient,  $B_c(\pi, z)$ . The lower value is the measured or attenuated backscatter coefficient,  $B_c'(\pi, z)$ . This results from the attenuation of the return signal as it passes through the cloud on the way up to level  $z$  and on the way back down to the receiver. To be more precise, one could subtract the molecular backscatter within the cloud to get a more accurate backscatter coefficient. The molecular backscatter could be found by extrapolating the below cloud return signal, but is typically very small and considered negligible.

The total area underneath the measured backscatter curve is the measured or attenuated integrated backscatter,  $\gamma_c'(\pi)$ . Likewise, the total area underneath the true backscatter curve is the true integrated backscatter,  $\gamma_c(\pi)$ . These values are found by integrating the backscatter coefficients from the bottom to the top of the cloud. Once  $\gamma_c(\pi)$  is found,  $B_c(\pi, z)$  is again integrated from the cloud base upwards until  $\gamma_c(\pi)/2$  is reached. This height is the effective mid-cloud height. This effective mid-cloud height is

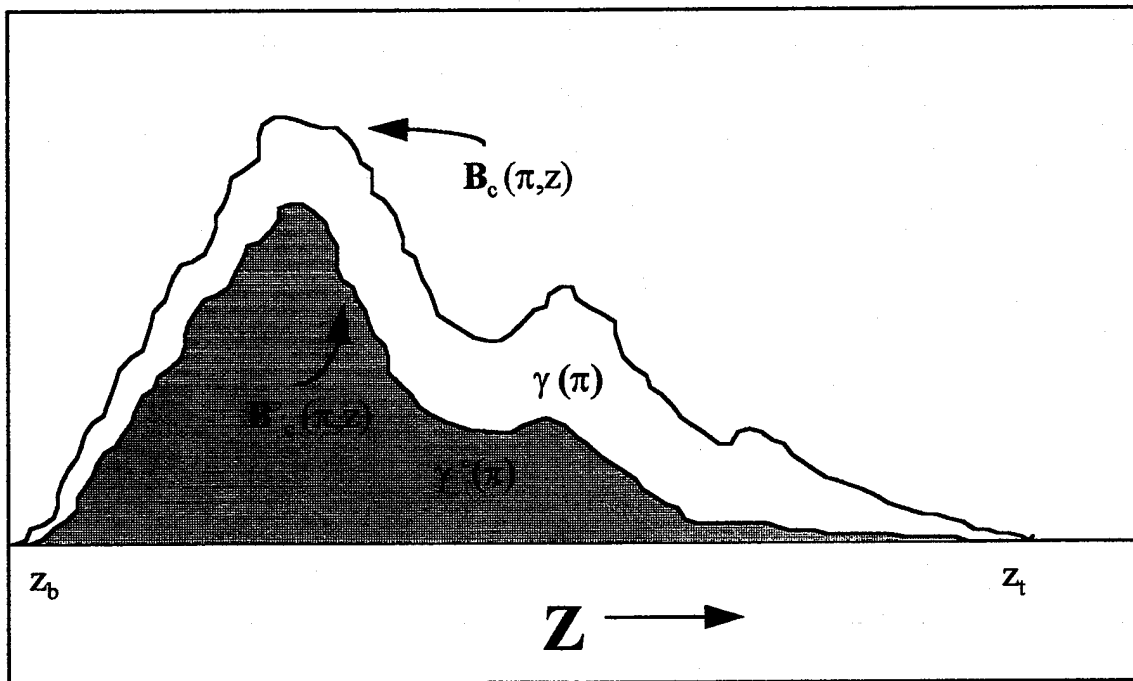


Figure 2.1. Illustration of a typical lidar backscatter profile. The lower curve represents the attenuated or measured lidar backscatter coefficient, while the upper curve represents the true or corrected backscatter coefficient. The shaded area represents the attenuated or measured integrated backscatter, while the area under the upper curve represents the true or corrected integrated backscatter.

combined with a nearby atmospheric sounding to determine a representative cloud temperature,  $T$ . This value is then input into a form of the Planck function to obtain the cloud's blackbody radiance ( $I_{bb}$ ):

$$I_{bb}(T) = 2h\nu^3 c^2 / [\exp(hc\nu/KT) - 1], \quad (2.1)$$

where  $c$  is the speed of light,  $K$  is the Boltzmann constant,  $h$  is Planck's constant,  $T$  is the representative cloud temperature, and  $\nu$  is the wavelength of the emission. The wavenumber,  $\nu$ , used in Eq. 2.1 is that of the radiometer.



### 2.1.3 Determining the True Backscatter Coefficient

The difficult part of this procedure is finding an accurate value for  $B_c(\pi, z)$ . The measured backscatter coefficient is given by:

$$B'_c(\pi, z) = B_c(\pi, z) \exp \left[ - \int_{z_b}^z 2\eta \sigma_c(z') dz' \right], \quad (2.2)$$

where  $\sigma_c(z')$  represents the volume extinction coefficient. Although  $\sigma_c(z')$  does include absorption and scattering of the beam by cloud particles, scattering processes dominate absorption by ice in the visible spectrum. The exponential portion of the equation represents the pulse attenuation of the lidar beam. Essentially, it represents twice the transmittance between the cloud base,  $z_b$ , and height  $z$ . Some of the energy scattered out of the beam during its passage through the cloud will be scattered back into the beam through multiple scattering processes. This effect is amplified by the fact that the receiver aperture may be large enough to collect diffraction-dominated forward scattering that stays within the laser pulse. The factor  $\eta$ , which is  $z$  dependent and usually between 0.5 and 1.0, accounts for this occurrence.

Correcting for pulse attenuation and obtaining a value for  $B_c(\pi, z)$  requires a combination of IR (radiometer) and visible (lidar) data. First,  $B'_c(\pi, z)$  is integrated through the cloud thickness ( $h$ ) to get the measured integrated backscatter:

$$\gamma'(\pi) = \int_{z_b}^{z+h} B'_c(\pi, z) \{ \exp[-2\eta \int_{z_b}^z \sigma_c(z'') dz''] \} dz. \quad (2.3)$$

At this time it is appropriate to introduce the backscatter to extinction ratio,  $\epsilon$ :

$$\epsilon = B_c(\pi, z) / \sigma_c(z). \quad (2.4)$$

This represents the ratio of the lidar energy scattered at  $180^\circ$  to the total amount of lidar energy scattered or absorbed at height  $z$ . The optical depth at height  $z$  is given by:

$$\tau_v(z-z_b) = \int_{z_b}^z \sigma_c(z'') dz'' . \quad (2.5)$$

Substituting Eqs. (2.4) and (2.5) into Eq. (2.3) and changing variables yields:

$$\gamma'(\pi) = k \int_{z_b}^{z_t} \exp(-2\eta\tau_v(z)) d\tau(z) . \quad (2.6)$$

Integrating this leads to a solution for the integrated backscatter coefficient in terms of the backscatter to extinction ratio and the visible optical depth:

$$\gamma'(\pi) = (k/2) \{1 - \exp[-2\eta\tau_v(\Delta z)]\} , \quad (2.7)$$

where  $\Delta z$  is the cloud depth. Note that the multiple scattering correction factor  $\eta$  has been brought outside the integrand. Although  $\eta$  is height dependent, it is assumed to be a constant for a given profile to simplify the solution  $\gamma'(\pi)$ . Platt and Dilley (1979) shows that  $\eta$  increases throughout a cloud and levels off after as the optical depths surpasses 1-2. However, it is possible to find a weighted mean value which allows for an accurate calculation of  $\gamma'(\pi)$ . The assumption is now made that the visible and IR absorption optical depths can be related by a constant:

$$\alpha = \tau_v(\Delta z)/\tau_i(\Delta z) . \quad (2.8)$$

Neglecting scattering in the infrared region, the infrared absorption emittance  $\varepsilon$  can be related to the infrared optical depth by:

$$\varepsilon = 1 - \exp[-\tau_i(\Delta z)]. \quad (2.9)$$

Substituting Eqs. (2.8) and (2.9) into Eq. (2.7) yields a value of the measured integrated backscatter in terms of  $\mu$  and  $\varepsilon$ :

$$\gamma'(\pi) = (\mu/2) [1 - \exp\{-2\alpha\eta \ln(1-\varepsilon)^{-1}\}]. \quad (2.10)$$

The  $\varepsilon$  used in Eqs. (2.9) and (2.10) are obtained from one of the simple methods described earlier (e.g., using the cloud base as the effective mid-cloud height). Thus an approximate relationship is developed between  $\gamma'(\pi)$  and  $\varepsilon$ . One can then find values of  $\mu$  by plotting  $\gamma'(\pi)$  versus  $\varepsilon$  from Eq. (2.10) and fitting a curve of  $\mu/2\eta$ . Now that a value of  $\mu/2\eta$  has been found, the measured backscatter coefficient can be corrected for pulse attenuation to find the true backscatter coefficient. This can be done by inverting Eq. (2.2) and solving through an iterative process as described by Platt (1973), or by solving for  $B_c(\pi, z)$  analytically as described by Davis (1969). Once  $B_c(\pi, z)$  is determined, the effective mid-cloud height is found by the precision method described in section 2.1.2. This of course eventually leads to  $I_{bb}$ .

During the process of correcting  $B_c(\pi, z)$ , several approximations are made. The multiple scattering factor and the backscatter to extinction ratio are assumed to be independent of  $z$ . Additionally the ratio of the visible and infrared optical depths were assumed to be constant for a given profile. Although these assumptions lead to a distortion of the  $B_c(\pi, z)$  profile, it is important to remember that here the LIRAD method is only being used to determine the effective mid-cloud height. Thus a value within 100-200 meters is sufficient to retrieve a representative value of  $I_{bb}$ , particularly since temperatures do not vary rapidly in the upper troposphere.

## 2.2 The Infrared Radiometer

Now that the solution for  $I_{bb}$  has been described, it is time to move on to the problem of finding  $I_c$ . This requires measurement of vertically downwelling radiance by a narrow beam infrared radiometer. Section 2.2.1 briefly describes the measurement process and the radiometer used at the FARS site. The quantity measured by the radiometer involves components other than the cloud radiance as Figs. 1.2a and 1.2b illustrate. The derivation of  $I_c$  from all of these components is described in section 2.2.2.

### 2.2.1 Instrumentation and Measurement

The instrument used at FARS to measure vertical downwelling radiance is a narrow-beam ( $0.14^\circ$ ) IR radiometer which is co-aligned with the lidar. It is capable of registering radiometric temperatures as low as  $-80^\circ\text{C}$ . Only on very cold, clear, and dry days will the atmospheric background temperature at Salt Lake City drop this low. The radiometer has a bandwidth of  $9.25\text{--}12.0\text{ }\mu\text{m}$ . This band is most suitable for studying high clouds since it lies within the atmospheric window region of the infrared spectrum. In this region, the atmosphere can be fairly transparent and the radiometer can see through it. Thus a cloud drifting over the receiver can be easily measured. Of course the atmosphere is not completely transparent in this band. The effects of atmospheric absorption by carbon dioxide, water vapor, and ozone are discussed later. Since the IR radiometer is co-aligned with the lidar, and it continuously records temperatures (i.e., radiances), the emittance for a cirrus cloud can be calculated at each lidar firing. This provides a detailed two-dimensional view of a cloud as it drifts over the site. The scanning capability of the Nd:YAG lidar allows for a limited three-dimensional view of the cloud.

### 2.2.2 Deriving the Cloud Radiance

As Fig. 1.2a illustrates, in a cloudy sky the vertical IR radiance measured at the surface will be comprised of two components:

$$I_m = I_{ec} \cdot T_{bc} + I_{cls} \quad (2.11)$$

As mentioned earlier,  $I_m$  is the radiance measured at the surface by the radiometer;  $I_{ec}$  the radiance exiting the base of the cloud resulting from scattering and absorption by ice crystals in the cloud;  $T_{bc}$  the transmittance of the atmosphere below the cloud; and  $I_{cls}$  the radiance emitted by absorbing gases in the atmosphere (Platt, 1973).

The cloud radiance exiting the cloud base,  $I_{ec}$ , has three components (see Fig. 1.2b). The primary component is  $I_c$ , which represents radiance resulting from cloud particle emission. A secondary component is  $I_{sr}$ , which represents upwelling surface radiance that gets scattered back into the receiver beam by the cloud. Finally,  $I_{ms}$  represents the multiple scattering of downwelling radiance from the cloud into the receiver beam (Platt and Gambling, 1971; Platt and Dilley, 1979; Platt and Stephens, 1980). This last component is very small and can be neglected with little loss of accuracy (Platt, 1973). It is negligible because scattering of IR by the relatively large ice crystals is highly forward peaked. The reason  $I_{sr}$  is large enough to be considered is that the temperature of the earth is much warmer than that of the upper troposphere and stratosphere, such that it emits much more energy. Thus the radiance exiting the cloud base can be accurately approximated by:

$$I_{ec} = I_c + I_{sr} \quad (2.12)$$

The atmospheric absorbing gas radiance,  $I_{cls}$ , also consists of three components. This clear-sky radiance is given by:

$$I_{cls} = I_{aac} \cdot T_c + \phi \cdot I_{aic} + I_{bc} \quad (2.13)$$

The first term in Eq. (2.13) represents the radiance emitted from above the top of the cloud ( $I_{aac}$ ) and attenuated by the cirrus ice crystals ( $T_c$ ). The second term represents the

radiance emitted by the absorbing gases inside the cloud layer ( $I_{aic}$ ) and attenuated by the ice crystals. The function describing this attenuation is  $\phi$ . The last term in Eq. (2.13) represents atmospheric emission between the cloud base and the earth's surface. It is usually the dominant of the three terms.

Substituting Eqs. (2.12) and (2.13) into Eq. (2.11) and rearranging results in a solution for the cloud radiance:

$$I_c = (I_m - I_{sr} \cdot T_{bc} - I_{aac} \cdot T_c - \phi \cdot I_{aic} - I_{bc}) / T_{bc} . \quad (2.14)$$

The first term in Eq. (2.14) is measured by the radiometer described earlier. The other terms must be derived from a radiative transfer model. Once Eq. (2.14) is solved, it is combined with the calculated blackbody radiance in Eq. (1.2) to obtain the absorption emittance. The other terms are obtained from a radiative transfer model described briefly in Chapter 1 and in more detail in Chapter 4.

## 2.3 Summary

The steps necessary to obtain a cirrus cloud narrow band absorption emittance have now been outlined. The IR radiometer and radiative transfer model are used to obtain the clouds true radiance. The lidar and aerological data are primarily used to determine the cloud blackbody radiance. The true radiance is simply divided by the blackbody radiance to get the emittance. Following in Chapters 3 and 4 is a description of the methods used to obtain the components of the true radiance of a cirrus cloud.

## **CHAPTER 3**

# **CALCULATION OF RADIANCE IN A NONHOMOGENEOUS ATMOSPHERE USING THE CORRELATED K DISTRIBUTION METHOD**

Attempting to accurately calculate radiative transfer over a large frequency spectrum, as required when analyzing IR radiance data from the PRT-5 Pyranometer, causes huge computational problems. The absorption coefficient,  $k_v$ , is highly dependent upon the wavenumber,  $v$ . Even in the atmospheric window where the PRT-5 operates (9.25-12  $\mu\text{m}$ ), there are over 46,000 different absorption lines. Table 3.1, which includes data extracted from the Hitran 1992 database developed by the Air Force Geophysics Laboratory, shows a breakdown of the absorption lines by species as well as a typical half-width for each.

### **3.1 The Need for an Alternative to LBL Models**

In order to accurately represent the absorption spectrum, one must sample the absorption coefficients at wave number intervals of less than the half-width. The half-width describes the broadening of spectral emission lines due to Doppler effects (Dopplerbroadening) and collisions with surrounding molecules (pressure broadening). The half-width may be expressed as a function of the pressure and temperature as:

$$\alpha = \alpha_0 (p/p_0)(T_0/T)^n, \quad (3.1)$$

Table 3.1

## Absorption Lines in the Atmospheric Window

Constituent	Number of Lines <sup>a</sup> at STP (cm <sup>-1</sup> )	Typical Half-width	Range of n Index
O <sub>3</sub>	44078	0.64	0.72-0.76
CO <sub>2</sub>	1898	0.07	0.75-0.79
H <sub>2</sub> O	423	0.65	0.64

a - Actually includes lines up to 25 cm<sup>-1</sup> on either side of the band that contribute to absorption in this region

n - Index that describes the temperature dependence of pressure broadening

where  $\alpha$  is the half-width,  $\alpha_0$  is the half-width at the reference pressure ( $p_0 = 1013$  mb) and reference temperature ( $T_0 = 273$  K), and  $n$  is an index which describes the temperature dependence of pressure broadening. These indices for the molecules of interest in this study are found in Table 3.1. At pressures as low as 10 mb, Eq. (3.1) shows that a sampling resolution as high as 0.001 will be necessary to properly represent the absorption spectrum. Since the PRT-5 radiometer has a receiver bandwidth of 248 cm<sup>-1</sup>,  $k_\nu$  will have to be sampled at almost 250,000 points in order to nominally represent the corresponding absorption spectrum. This can be accomplished by a LBL model such as FASCODE, but only at great computational expense. For most applications this simply is not feasible.

Many statistical band models such as the Goody and Malkmus models have been developed to combat this problem. They drastically reduce computational effort by getting rid of the wave number integration. However, for nonhomogeneous atmospheres, the one or two parameter approximation must be used to represent the  $k_\nu$  dependency upon  $p$  and  $T$ . This can lead to large deviations from results computed by LBL models, especially for the 9.6  $\mu$ m ozone band (Fu and Liou, 1992; Fu 1992).



## 3.2 The K Distribution Method in

### Homogeneous Atmospheres

One computationally efficient approach to solving radiative transfer problems that has been quite successful is the k-distribution method. The k-distribution method involves the ranking of absorption coefficients in a frequency interval by their strength. This is possible since spectral transmittance in a homogeneous atmosphere is independent of the ordering of the absorption coefficients. Therefore, using  $k_v$  as the independent variable, the transmittance can be calculated by an integration over k-space instead of an integration over  $v$ -space:

$$\frac{1}{\Delta v} \int_{\Delta v} e^{-k_v \rho dz} dv = T_v(z) = \int_0^\infty e^{-k \rho dz} f(k) dk, \quad (3.2a)$$

where  $f(k)$  is the k-distribution function of absorption coefficient over  $\Delta v$ , and:

$$\int_0^\infty f(k) dk = 1. \quad (3.2b)$$

A cumulative probability function,  $g(k)$ , can be defined as:

$$g(k) = \int_0^k f(k) dk, \quad (3.3)$$

where at  $k=0$ ,  $g=0$  and as  $k \rightarrow \infty$ ,  $g \rightarrow 1$  and  $dg(k) = f(k)dk$ . Since  $g(k)$  is a cumulative probability, it is a monotonically increasing and smooth function. Finally, since  $g(k)$  is a monotonically increasing and smooth function, there must be an inverse function of  $g(k)$  as  $k(g)$ . Thus using  $g$  as the independent variable in Eq. (3.2a) one gets an equation for transmittance:

$$T_v(z) = \int_0^1 e^{-k(g) \rho dz} dg. \quad (3.4)$$

The great advantage of using the  $g$ -space integration Eq. (3.4) over the  $\nu$ -space integration (first part of Eq. (3.1)) is that  $k(g)$  is a well behaved function. Thus the integration can be approximated by summation of much fewer intervals than the  $\nu$ -space integration. Depending on the accuracy needed for the particular application, the number of needed  $g$  intervals may range from a few to several hundred, resulting in huge savings in computational effort.

Figure 3.1(a)-(d) illustrates the process through which the absorption coefficients are transformed from a function of  $\nu$  to a function of  $g$ . Figure 3.1(a) shows absorption coefficients for  $\text{CO}_2$  in part of the atmospheric window region at 100 mb and 220 K. Figure 3.1(b) shows the probability function for  $k$  as a function of the absorption coefficient strength. Figure 3.1(c) shows the cumulative probability  $g$  as a function of  $k_\nu$ , and Fig. 3.1(d) shows  $k_\nu$  as a function of the cumulative probability (i.e. the inverse of Fig. 3.1(c)). These figures will be referenced in the following section which describes the process of arriving at  $k(g)$ .

The most accurate and time consuming method of calculating  $k_\nu$  values for use in the  $k$ -distribution model is to obtain the  $k_\nu$  values at a very high spectral resolution using a LBL model. This seems counterintuitive since the purpose of  $k$ -distribution is to avoid using lengthy LBL models. One must keep in mind, however, that the  $k_\nu$  values only need to be calculated once for each pressure, temperature, and absorbing species. In this research, a spectral resolution of  $0.0004 \text{ cm}^{-1}$  was found to be small enough to accurately represent the  $k(\nu)$  function.

The next step in the process is to break the range of  $k_\nu$  values into small intervals or bins (approximately 100 per order of magnitude strength). The large array of  $k_\nu$  is then spectrally integrated according to the equation below (Lacis and Oinas 1991):

$$f(k_i) = \frac{1}{\nu_2 - \nu_1} \sum_j^m \left| \frac{\Delta \nu_j}{\Delta k_i} \right| W(k_i, k_i + \Delta k_i), \quad (3.5)$$

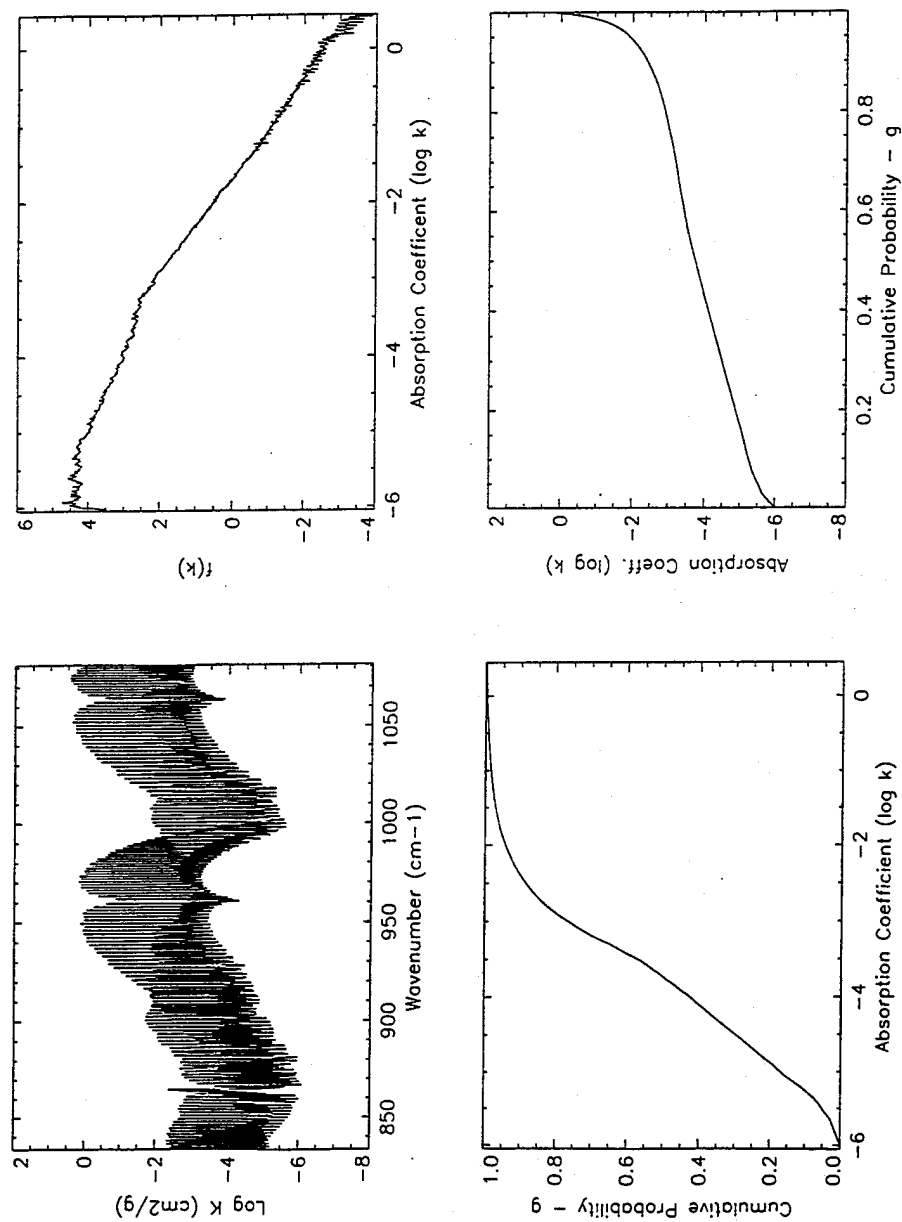


Figure 3.1. (a) Absorption coefficients as a function of  $\nu$  for CO<sub>2</sub> at 100 mb and 220 K in the atmospheric window region of the IR spectrum. (b) Probability function  $f(k)$  of the absorption coefficient. (c) Cumulative probability function,  $g(k)$ , as a function of  $k$ . (d) The inverse function of (c), the absorption coefficient as a function of the cumulative probability function.

where  $W$  is a window function such that  $W=1$  when  $k_i < k_v < k_i + \Delta k_i$  and  $W=0$  otherwise. The symbols  $k_i$  represent the strength bins, and  $m$  is the total number of  $k_v$  values sampled in step one. Thus  $f(k_i)$  represents the portion of the total  $v$  interval in which the absorption coefficient has a value between  $k_i$  and  $k_i + \Delta k_i$ . This is the  $k$ -distribution illustrated by Fig. 3.1(b). Next,  $f(k)$  is integrated from  $k_{\min}$  to  $k_{\max}$  to achieve a cumulative probability function  $g(k)$  as shown in Fig. 3.1(c). Finally  $g(k)$  is inverted to get  $k(g)$  as illustrated in Fig. 3.1(d). As Fig. 3.1(d) clearly demonstrates, the resulting  $k(g)$  function should be much easier to integrate than the ill behaved function in Fig. 3.1(a).

Though using Eq. (3.5) is the most mathematically correct method of getting  $k(g)$ , it is very cumbersome. A much simpler and equally valid method is to directly compute  $k(g)$  by sorting all of the discretely sampled  $k(v)$  values and placing them in order of increasing strength (Fu and Liou, 1992), i.e;

$$g(k) = n(0,k) / N, \quad (3.6)$$

where  $N$  is the total number of sampled points, and  $n(0,k)$  is the number of absorption coefficients between 0 and  $k$ . This function is easily inverted to obtain  $k(g)$ . This method is many times faster and is equally valid as the longer method if the sampling interval of  $k(\Delta v)$  is constant.

The monotonic and smooth features of the  $k(g)$  function can now be used to calculate a transmittance in a homogeneous path using Eq. (3.4). The integration in Eq. (3.4) is approximated by a finite number of  $g$  intervals. The lower  $g$  values, that is at  $g < 0.9$  or so, can be approximated by only a few intervals since in this region the  $k(g)$  function is slowly changing and since absorption in this region is weak (see fig 3.1(d)). This area represents weak line and far wing absorption. The area of the curve near  $g=1$  represents strong line absorption. As suggested by Fu (1991), the  $g$  interval spacing in this region should be closer in order to accurately represent the rapidly increasing  $k(g)$

function. Accurate representation of the  $k(g)$  function here is most important since most absorption occurs near  $g=1$ . As will be shown later,  $g$ -space resolution does have a large impact on the accuracy of a CKD model.

### 3.3 Application of the K Distribution Method to Nonhomogeneous Atmospheres

#### 3.3.1 The Correlated Assumptions

In order to use the  $k$ -distribution method for real atmospheres, it must be extended for use in nonhomogeneous paths. Scaling parameter approximations could be used to account for the variation of  $k(v)$  with pressure and temperature. These approximations have been demonstrated to work poorly in the upper atmosphere since the approximations are based on reference values that are usually set in at high temperatures and pressures. Furthermore it has been demonstrated that they do not work well in regions where ozone absorption is strong due to the inverted nature of the ozone profile. The correlated  $k$ -distribution method (CKD) as proposed by Lacis et al. (1979) performs much better in these situations. The fact that ozone is a strong absorber in the spectral range of the PRT-5 detector was a major factor in deciding to use a CKD model for this study.

The assumptions of the correlated  $k$ -distribution method are quite simple. The CKD method assumes that monochromatic absorption coefficients at different pressures and temperatures are correlated in the following situations:

- 1) If  $k(v_1) = k(v_2)$  at  $T_r$  and  $p_r$ , where  $T_r$  and  $p_r$  are reference values, then  
 $k(v_1) = k(v_2)$  at any other  $p$  and  $T$ .
- 2) If  $k(v_1) > k(v_2)$  at  $T_r$  and  $p_r$ , then  
 $k(v_1) > k(v_2)$  at any other  $p$  and  $T$ .

This essentially means that for a given  $v$  value, there is only one  $g$  at any height. Fu and Liou (1992) have shown that this CKD approach is exact in the single, weak, and strong

line limits thus making it physically superior to the Curtis-Godson two parameter approximation.

West et al. (1990), Lacis and Oinas (1991), and Fu and Liou (1992) have demonstrated that these correlated assumptions do not always hold for realistic atmospheric conditions. Deviations result from the fact that the line intensities and half-widths for different lines do not always have the same T-dependence. Also the overlap of lines tends to invalidate these correlated assumptions.

### 3.3.2 Calculating the Equivalent K Functions

Theoretically, these correlation problems could be eliminated simply by calculating tables of  $k(g)$  for input into the CKD model at very high p and T resolution. Since this is not feasible for computational reasons, temperature and pressure resolution must be chosen to keep the correlation errors to a minimum without sacrificing too much computation speed.

#### 3.3.2.1 Choosing the Temperature Values

The absorption coefficient is dependent upon temperature through both the line intensity and broadening functions. Chou and Kouvaris (1986) showed that  $\ln(k_v)$  could be represented by a quadratic function such as:

$$\ln(k) = a + bT + cT^2, \quad (3.7)$$

where the coefficients a, b, and c are calculated at 210, 250, and 290 K. They further demonstrated that at normal atmospheric temperatures, the error in  $k_a$  using Eq. (3.7) should be less than 1.0%. To maintain accuracy for a wider range of temperatures, a cubic function was used for this experiment, with the coefficients being calculated at 180,

220, 260, and 300 K. Figure 3.2a shows the temperature dependence of the CO<sub>2</sub>  $k$ -distribution in the window region at 100 mb.

### 3.3.2.2 Choosing the Pressure Values

The variation of the absorption coefficient with pressure occurs through the computation of the collision-broadened half-width as shown in Eq. (3.1). Calculating exactly how  $k_v$  varies with  $p$  is not so straightforward. As Chou and Kouvaris (1986) point out,  $k_v$  is proportional to  $p$  in the wings of absorption lines but proportional to  $1/p$  near line centers. This presents a dilemma as to how to interpolate  $k(p)$ .

Since absorption near the line centers tends to saturate over a short path length, accurate  $k_v$  values near these line centers are not as important as in the wings. Additionally, in the atmospheric window the spectral area covered by absorption lines is much smaller than that area covered by distant wings. Thus it is expected that  $p$  interpolation errors are minimized by linearly interpolating  $k_v$  with respect to pressure. Figure 3.2(b) shows the pressure dependence of equivalent  $k_v$  functions for CO<sub>2</sub> at a temperature of 220 K.

Chou and Kouvaris (1986) showed that using a pressure spacing of  $(\log \Delta p) = 0.2$  the maximum interpolation error for  $k_v$  would be around 5% and that a spacing of  $(\log \Delta p) = 0.1$  results in interpolation errors of around 1%. Since errors in  $k_v$  are less sensitive to  $p$  interpolation at line centers, it follows that overall errors in  $k_v$  using a  $(\log \Delta p) = 0.1$  spacing results in errors significantly less than 1%.

Based on these findings and the fact that this CKD model is only applied to altitudes less than 30 km (10 mb), the  $(\log \Delta p) = 0.1$  pressure spacing was chosen. Table 3.2 shows the pressures at which  $k(g)$  were calculated for this research. A resolution of  $(\log \Delta p) = 0.05$  was tested between 1000-500 mb, but the resulting differences in  $k$  values were negligible.

Overall, a table of  $k(g,p,T)$  values was created for 20 pressures and 4

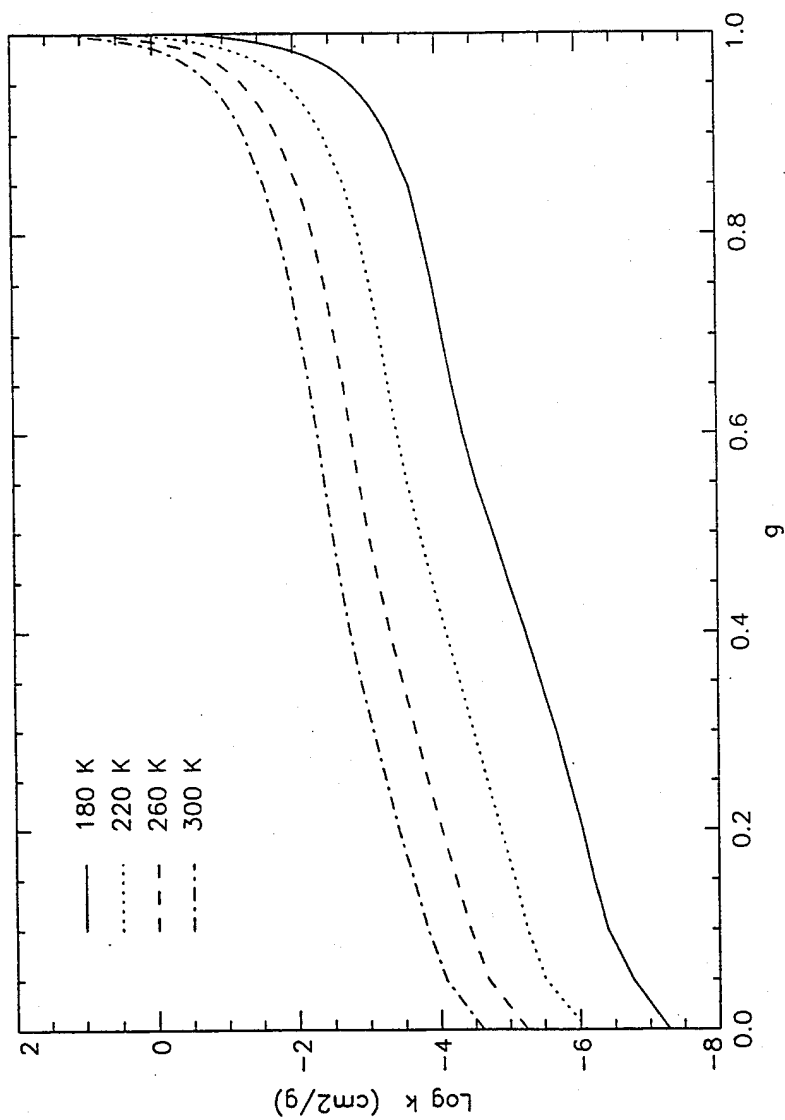


Figure 3.2. Temperature and pressure dependence of the mass absorption coefficients,  $k_v$ . (a) Temperature dependence of  $k_v$  for  $\text{CO}_2$  in the atmospheric window region at 100 mb. The range of temperatures represents the extremes expected in the lower stratosphere and troposphere. (b) Pressure dependence of  $k_v$  in the atmospheric window region at 220 K. The pressures represent the extreme upper and lower bounds of the area for this LIRAD study.



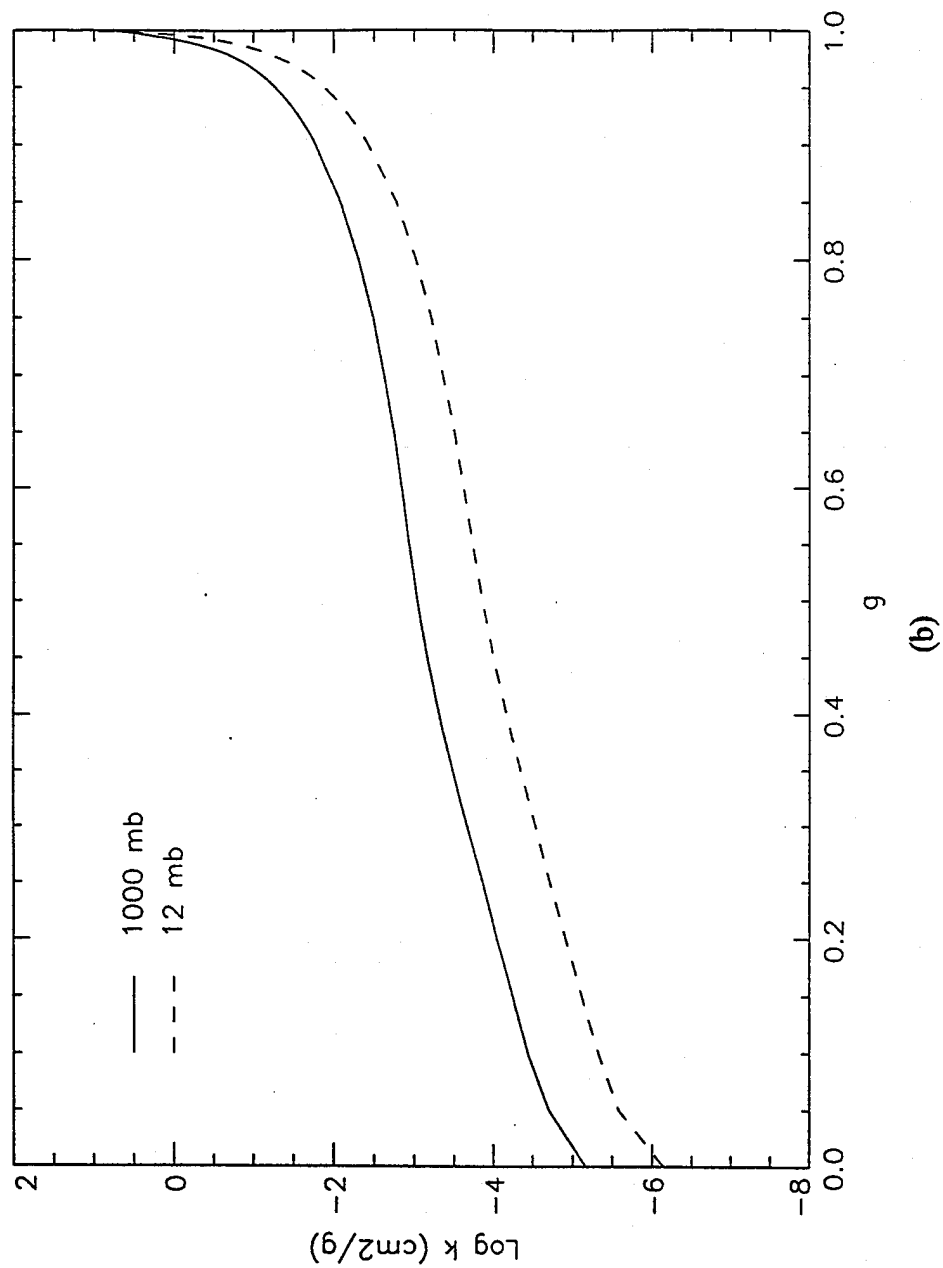


Figure 3.2 (continued)

temperatures. This required running a LBL program 80 times. Although this is a large expenditure of time and computational effort, it is certain that with the large volume of data to be processed, the CKD method will make this effort worthwhile.

Table 3.2

## CKD Model Pressure Levels

Pressures (mb) Used for Calculation of $k(g,p,T)$			
1000	316	100.0	31.6
794	255	79.4	25.5
631	199	63.1	19.9
501	158	50.1	15.8
398	126	39.8	12.6

## **CHAPTER 4**

### **DESCRIPTION OF THE FARS CORRELATED K-DISTRIBUTION MODEL**

The primary purpose of this study was to develop a radiative transfer model that would calculate many of the radiation components of Eq. (1.1), such as  $I_{sr}$  and  $I_{bc}$ , from data measured at the Facility for Atmospheric Remote Sensing. This would eventually lead to a solution for cirrus cloud emittance. The model needed to calculate upwelling and downwelling radiance in the spectrum of the atmospheric window. The model also needed to run much faster than a LBL model without sacrificing too much accuracy. Additionally the model was required to work in a variety of climates from a cold and dry winter to a subtropical summer. Finally, the model was required to have a domain from the surface and above up to the height of cirrus clouds in the lower stratosphere. For reasons stated in Chapter 3, the CKD method was the obvious choice of radiative transfer methods to build the model around.

The model constructed is called the Facility for Atmospheric Remote Sensing Correlated K-Distribution Model. Throughout the remainder of this thesis it is referred to as the FARS CKD model or simply the CKD model. This chapter will outline the process through which the model calculates the required radiative parameters such as upwelling radiance and downwelling below-cloud radiance. During this process some of the model strengths, weaknesses, and sources of error will be discussed. First is a brief description of the model features.

## 4.1 Model Features

The FARS CKD model is designed specifically to solve the radiative transfer equation in the spectral range of the FARS PRT-5 pyranometer, which is  $9.25\text{ }\mu\text{m}$  to  $12.0\text{ }\mu\text{m}$  (or  $883\text{ cm}^{-1}$ - $1081\text{ cm}^{-1}$ ). The model accommodates inputs either from local atmospheric sounding data or standard atmospheric profiles such as those provided by the U.S. Standard Atmosphere.

In addition to its fixed facility, FARS has a mobile lidar-radiometer ensemble that has been deployed in many field experiments such as the 1991 Project FIRE Intensive Field Operations campaign and the 1994 Atmospheric Radiation Measurement Regional Central States Intensive Observation Period. In the future it may even be deployed to tropical locations. This potentially requires a radiative transfer model which is accurate in a wide variety of conditions, from subarctic to tropical. Since it will primarily be used to analyze mid-latitude data, however, it has been tuned to work best under these conditions.

Since this model is designed to study mainly cirrus clouds, its domain must include altitudes up to the lower stratosphere. The FARS CKD model has a domain extending from the surface up to  $12.5\text{ mb}$ , or around  $30\text{ km}$ , depending on the temperature of the atmosphere. This upper boundary was chosen because it is high enough to incorporate virtually all  $\text{H}_2\text{O}$  and  $\text{CO}_2$  emission and most  $\text{O}_3$  emission. Although cirrus clouds rarely exist above  $15\text{ km}$ , at midlatitudes, a  $30\text{ km}$  ceiling is necessary when analyzing clear-sky data or very thin cirrus clouds where above-cloud emissions may be important. Altitudes higher than  $30\text{ km}$  were not included in order to reduce computational time and the time required to create absorption coefficient files, a very cumbersome process.

To alleviate fears that this  $30\text{ km}$  ceiling might compromise the accuracy of the model, a study was done to quantify the amount of downwelling radiance from ozone above  $30\text{ km}$ . The FASCODE LBL model was used to compare downwelling radiance (at the surface) from  $30\text{ km}$  against downwelling radiance from  $50\text{ km}$  in the infrared window. The  $50\text{ km}$  ceiling was chosen because virtually no ozone exists above this level. The

results showed that using an upper boundary of 30 km instead of 50 km reduced downwelling radiance in a clear sky by less than one percent. In cloudy atmospheres, the difference would be even less. Furthermore, errors are expected to be reduced even more when the filter is added to the model, because the filter cuts off much of the emission from ozone, the primary emitter above 30 km. Thus, using a model ceiling of 30 km is a good way of speeding up the model without much loss in accuracy.

The FARS CKD model was constructed to allow easy variation of the height and g-space resolutions. Variable height resolution is necessary to accommodate sounding data. Most of the tests in this study were run at 1-km, the resolution of the standard atmospheric profile data. A maximum of 150 layers is allowed. The g-space resolution is also variable. Up to 119 "g" values are allowed and varying  $\Delta g$  values can be used. The height and g-space resolutions as well as boundary conditions are read from an input file, which the user can edit easily.

When calculating  $I_{\pi}$  in Eq. (1.3) it will be necessary to calculate upwelling radiance at many different angles for input into the cirrus cloud scattering phase function. Although the best phase functions have yet to be determined, the model can calculate upwelling surface radiance at any zenith angle up to  $80^{\circ}$ . The user also has the option of using the diffusivity factor to calculate diffuse transmittance and upwelling flux.

The CKD radiative transfer model calculates transmittance functions for all the major emitters in the bandwidth of the PRT-5 radiometer, namely  $\text{CO}_2$ ,  $\text{H}_2\text{O}$ ,  $\text{O}_3$ , and the water vapor continuum. A major difference between this and previous LIRAD studies is that the previous studies have not included  $\text{CO}_2$  or  $\text{O}_3$  emission in their radiative transfer models. As will be shown, these constituents are important emitters and must be included to obtain a high degree of accuracy in calculating transmittance functions. The most important emitter in the window region is the water vapor continuum. The method for calculating continuum emission is a complicated issue described in subsection 4.2.2.4.

Two other gases that have minor absorption bands in the window region are  $\text{CH}_4$  and  $\text{N}_2\text{O}$ . Their contributions, however, are very small and since they emit at the edge of the PRT-5 detector window, their effects are substantially cut off by the filter. Hence they are not included in the CKD model.

The inclusion of aerosol absorption/emission is another matter that must potentially be dealt with. Although aerosol amounts are usually small above the FARS site, their emissions and scattering might contribute significantly to the downwelling radiance measured at the surface in very cold dry atmospheres where water vapor emission is small. This issue is further complicated by the fact that aerosol amounts can be quite variable and are not routinely measured. At this time aerosols have not been included in the model, but this is an area worth studying in the future.

## **4.2 Calculating IR Radiance with the FARS CKD Model**

### **4.2.1 The Process**

The process of calculating atmospheric radiance with the FARS CKD model involves much more than simply running the model. The FARS CKD radiative transfer solution process can be broken into three phases; the preexecution phase, the model execution phase, and the postexecution or analysis phase. The following sections will describe each phase and outline the major tasks within each phase. A diagram is provided in Fig. 4.1 to assist the reader in visualizing these tasks. The reader will find it helpful to refer to this diagram during the description of the process.

### **4.2.2 The Preexecution Phase**

The preexecution phase primarily involves preparing absorption coefficients and atmospheric profile data for input into the model. The preparation of absorption coefficient data is the most difficult and time consuming task in the entire process, and is one of the drawbacks of using the CKD method in a radiative transfer model. It is also a

# FARS CKD PROCESS

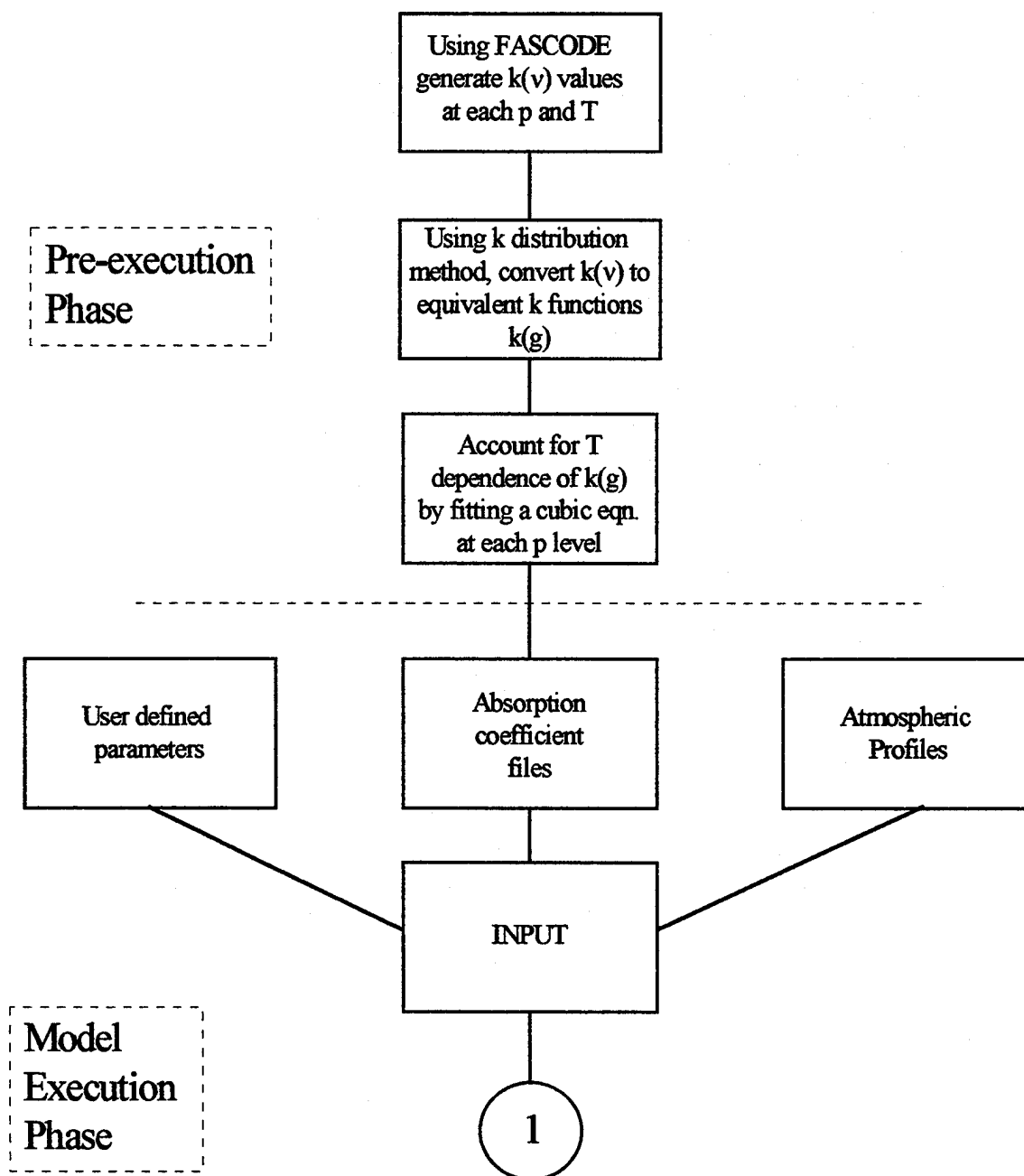


Figure 4.1. Flow chart for the FARS CKD model radiative transfer solution process, outlining the major steps of calculating radiation.

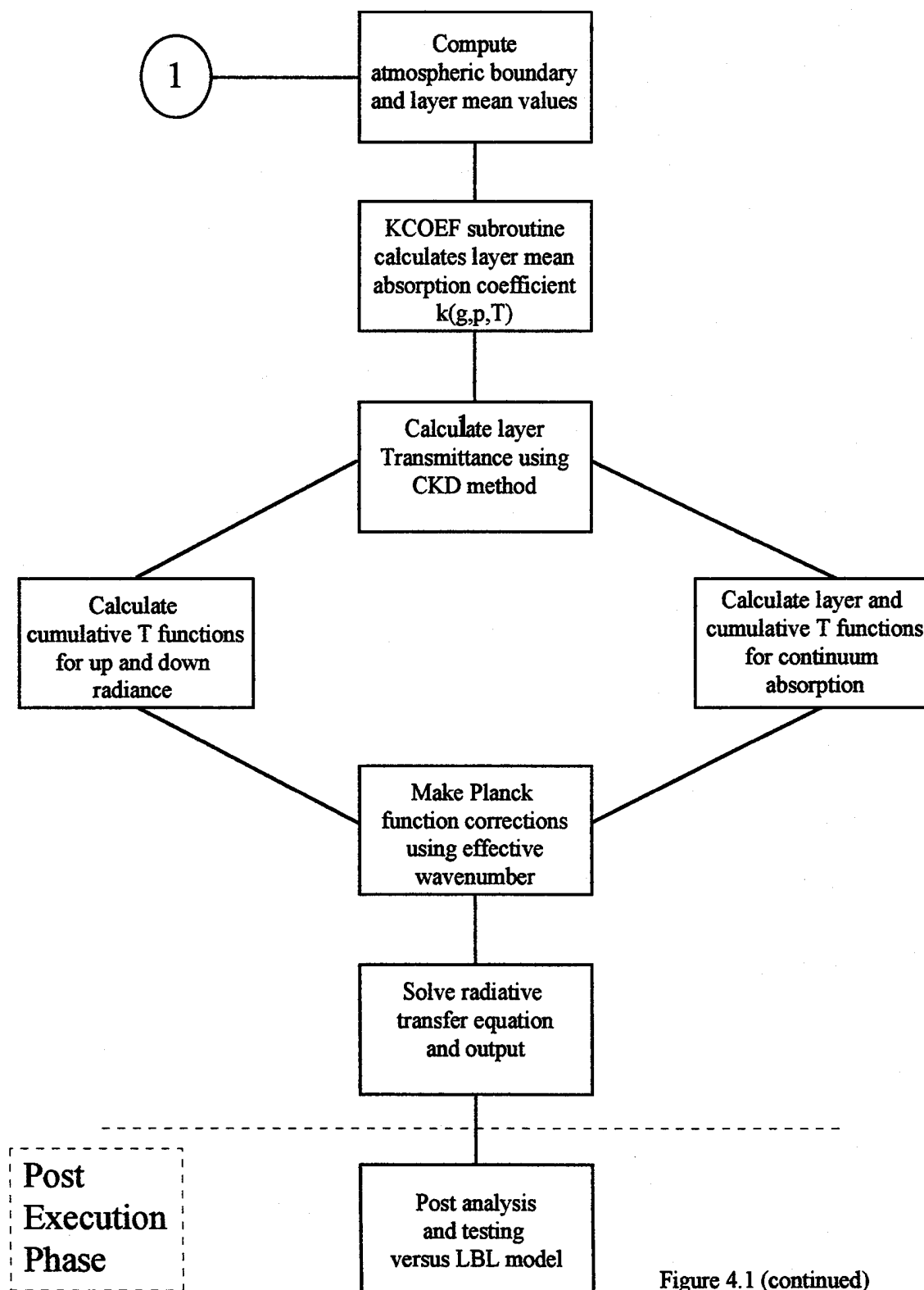


Figure 4.1 (continued)



most critical task. It is absolutely necessary that the radiative transfer model use accurate mass absorption coefficient data in order to reliably solve the radiative transfer equation.

The fundamental step in solving a radiative transfer problem is deriving transmittance functions for each layer in the atmosphere. As Eq. (4.1) shows, transmittance is exponentially dependent on the absorption coefficient, the atmospheric density, and the depth (amount of atmosphere) in a layer:

$$T_{\nu} = \frac{1}{\Delta \nu} \int_{\nu_1}^{\nu_2} \exp\left[-\int_{z_1}^{z_2} k(\nu, p, T) \rho dz\right] d\nu, \quad (4.1)$$

where  $\rho$  is the density of the absorbing gasses in that layer. The density and depth can be measured with a high degree of accuracy. Obtaining an accurate and representative layer absorption coefficient is not so easy, so great care must be taken in obtaining that value.

#### 4.2.2.1 Calculating Monochromatic Mass

##### Absorption Coefficients

The most accurate method of deriving these coefficients, and the method used in this study, is to derive them directly from a line-by-line model (Liou, 1992). After the absorption coefficients tables are derived, they are converted to cumulative probability functions using the CKD method as described in Chapter 3. The CKD method has already been discussed and will not be repeated, but a step-by-step process for incorporation of the derived absorption coefficients into the model is outlined below.

The LBL model from which the absorption coefficients are derived is version three of the FASCODE model created by the Air Force Geophysics Laboratory. The LBL model is altered slightly to calculate the mass absorption coefficient,  $k_{\nu}$ , instead of optical depth. The LBL model is then run for short homogeneous paths to calculate  $k_{\nu}$  at a very high spectral resolution. The spectral resolution is four times the Voigt half-width, which is dependent upon the gas, pressure and temperature (Liou, 1992). Spectral resolutions

varied from  $0.0004 \text{ cm}^{-1}$  at a height of 30 km to  $0.0262 \text{ cm}^{-1}$  at the earth surface. Since the bandwidth of the receiver is  $248 \text{ cm}^{-1}$ , each  $k_v(p,T)$  array could have as many as 620,000 values.

These  $k_v$  arrays are generated at each of the 20 pressure values in Table 3.2 and the 4 temperature values listed in section 3.3.2.1. This process is repeated for each of the three atmospheric constituents included in the model, resulting in 240 (20 pressures  $\times$  4 temperatures  $\times$  3 gases) mass absorption coefficient ( $k_v$ ) arrays, each containing between 10,000 and 620,000 values.

#### 4.2.2.2 Conversion to Equivalent K Functions

##### Using the K-Distribution Method

The next step in the preexecution phase is to apply the CKD method and create equivalent  $k$  functions at each pressure and temperature. First, each of the absorption coefficient values in each array are sorted in ascending order of strength. Next, using the short cut described in section 3.2 and Eq. (3.6), functions are created that describe the absorption coefficients for the radiometer bandwidth in terms of cumulative strength probability.

Before doing this, the user must decide upon the desired accuracy by choosing a  $g$ -space resolution. Just as spatial resolution in an atmospheric circulation model determines how accurately that model represents the atmosphere, the  $\Delta g$  resolution impacts how accurately the CKD model represents the absorption coefficient spectrum. Figure 4.2 illustrates this. In Fig. 4.2(a), a  $\Delta g$  of 0.2 is used and the absorption coefficient function is represented by  $k(g)$  at only five cumulative probability or  $g$  values. Figure 4.2(b) shows this same function represented by  $k(g)$  at 10  $g$  values, or a  $\Delta g$  of 0.1. Obviously, the 10 values in Fig. 4.2(b) represents the absorption coefficient function better than the five values in Fig. 4.2(a). This, of course, comes at the expense of computation time since each extra point represents an additional integration step.

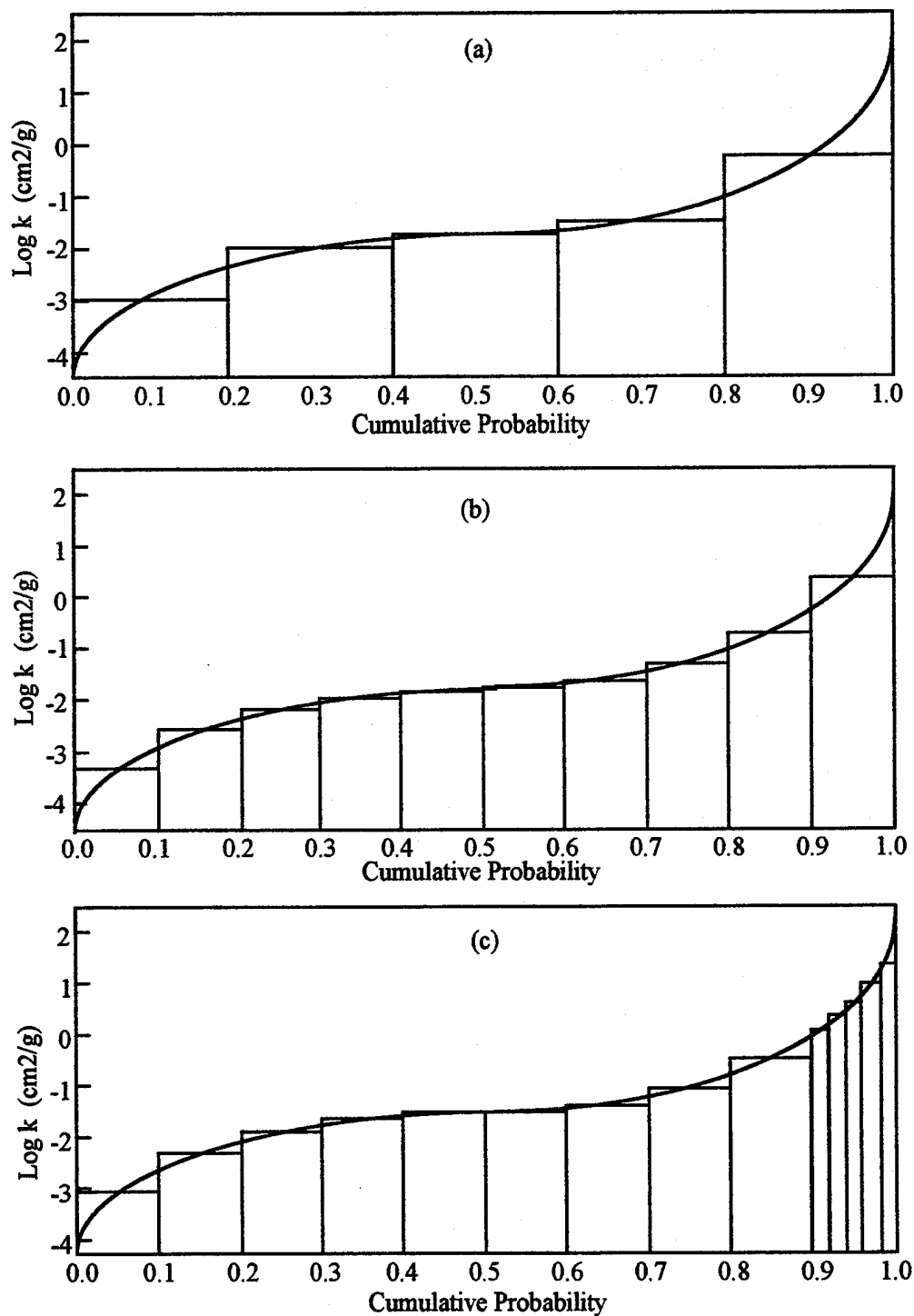


Figure 4.2. Equivalent  $k$  functions,  $k(g)$ , and their finite representation by; (a) a low resolution CKD model, (b) a higher resolution model, and (c) a variable resolution model.

One way to get the best of both worlds is to use a variable  $\Delta g$  resolution (see Fig. 4.2(c)). The lower values of  $k(g)$  on the left side of Fig. 4.2(c) represent absorption in the far wings of absorption lines. Here it is not necessary to represent the absorption spectrum with a great deal of accuracy. The high values of  $k(g)$  on the extreme right side of Fig. 4.2(c) show absorption very near absorption lines. The vast majority of absorption and emission takes place in this area so it must be represented accurately with a high  $\Delta g$  resolution. In Fig. 4.2(c) the lower  $k(g)$  values are represented at discrete points using a  $\Delta g$  of 0.1. At cumulative probabilities above  $g = 0.9$ , a  $\Delta g$  resolution of 0.02 is used. Now the entire absorption coefficient function is represented by 14 discrete points. So by increasing the integration steps by only 40% (10 steps to 14), the accuracy of the absorption coefficient function for the radiometer bandwidth is increased significantly over that in Fig. 4.2(b).

Most of the tests described in Chapter 5 used a  $\Delta g$  of 0.05 at  $g < 0.9$  and a  $\Delta g$  of 0.01 at  $g > 0.9$ . So, the absorption coefficient functions that were spectrally represented by 10,000 to 620,000 points are reduced to only 119 points. This process is repeated for each of the 240 arrays of  $k_v$  values derived from the LBL model. Thus the  $k$ -distribution representation of the model atmosphere absorption coefficient functions contains 28,560 data points (20 pressures  $\times$  4 temperatures  $\times$  3 gases  $\times$  119  $g$  values). This remains a considerable amount of data, but 1000 times less than the  $10^7$  values required by a spectral representation, with little loss in accuracy.

#### **4.2.2.3 Accounting for the Temperature Dependence**

##### **of the Absorption Coefficient**

The final process necessary to prepare the absorption coefficients for the CKD model is to account for the  $p$  and  $T$  dependence of the absorption coefficients. Section

3.3.2.1 showed that the relationship between the natural logarithm of the absorption coefficient ( $\ln(k)$ ) was roughly linearly dependent on the temperature. Thus,  $\ln(k)$  could be fit to a quadratic or cubic equation if values of  $\ln(k)$  were known at several temperatures within the normal atmospheric temperature range. In this study, absorption coefficient arrays were calculated for each pressure level at 180, 220, 260, and 300 K. Using the  $k$  values calculated at each of these temperatures, and the relationship;

$$\ln(k) = a + bT + cT^2 + dT^3, \quad (4.2)$$

the coefficients of the cubic ( $a$ ,  $b$ ,  $c$ , and  $d$ ) are calculated for each  $g$  value and pressure level. Now at each pressure level and for each constituent, only one array containing  $g$  values and the cubic coefficients is needed (instead of four) to describe the absorption coefficient function. In other words there are now 20 arrays for each constituent for a total of 60 arrays (20 pressures x 3 constituents). Each of the pressure arrays was then stacked into one array for each constituent so that only one file for each gas need be input into the model to completely describe the absorption coefficient function of that gas. This file is input into the FARS CKD model. Table 4.1 shows an example of what a typical absorption coefficient input file looks like. The headings  $a$ ,  $b$ ,  $c$ , and  $d$  refer to the coefficients used in Eq. (4.2).

Recall from subsection 3.3.2.2. that the absorption coefficient is roughly linearly dependent upon pressure. In the model, a simple linear interpolation is used to calculate the absorption coefficient at any pressure. Thus, the long and cumbersome task of crunching the absorption coefficients into a mode suitable for input into the CKD model is complete.

Results from this method of calculating  $k$ -distribution functions were compared against functions created by Fu (1991) and Lacis and Oinas (1991) and yielded very simi-

Table 4.1

## Parameters Contained in Absorption Coefficient Files

g	Pressure (mb)	a	b	c	d
0.05	1000.0	-0.1335E+02	0.2975E-01	-0.5397E-04	0.5996E-06
0.05	794.3	-0.1358E+02	0.2976E-01	-0.5357E-04	0.5996E-06
0.05	630.1	-0.1382E+02	0.2976E-01	-0.5366E-04	0.5888E-06
0.05	501.2	-0.1405E+02	0.2976E-01	-0.5366E-04	0.5871E-06
0.05	398.1	-0.1428E+02	0.2976E-01	-0.5365E-04	0.5870E-06
0.05	316.2	-0.1451E+02	0.2976E-01	-0.5290E-04	0.5870E-06
0.05	251.2	-0.1474E+02	0.2977E-01	-0.5357E-04	0.5870E-06
0.05	199.5	-0.1497E+02	0.2977E-01	-0.5358E-04	0.5866E-06
0.05	158.4	-0.1520E+02	0.2977E-01	-0.5360E-04	0.5864E-06
.	.	.	.	.	.
.	.	.	.	.	.
.	.	.	.	.	.
0.50	1000.0	-0.1870E+00	0.3543E-01	-0.8877E-04	-0.2314E-06
0.50	794.3	-0.1890E+00	0.3545E-01	-0.8875E-04	-0.2314E-06
0.50	630.1	-0.1902E+00	0.3546E-01	-0.8911E-04	-0.2204E-06
.	.	.	.	.	.
.	.	.	.	.	.
.	.	.	.	.	.
1.00	19.9	0.1186E+02	-0.8985E-03	0.6980E-05	-0.2111E-06
1.00	15.9	0.1120E+02	-0.7934E-04	0.1618E-06	-0.4659E-06
1.00	12.7	0.1211E+02	-0.2090E-03	-0.2195E-05	-0.4713E-06

lar results. Only the description of the continuum function remains before execution of the model can begin.

#### 4.2.2.4 Continuum Function

The water vapor continuum is a major contributor to downwelling emission measured at the surface in the spectrum of the FARS IR radiometer. Recall that Fig. 1.3(b) showed that in a warm moist atmosphere, continuum absorption completely dominated emission from  $\text{CO}_2$ ,  $\text{H}_2\text{O}$ ,  $\text{O}_3$  absorption lines. Figure 1.3(a) showed that even in a cold dry atmospheric profile, continuum absorption was the primary emitter below 6 km. Therefore, properly choosing a method of calculating the continuum absorption is critical in determining the success or failure of a radiative transfer model calculating downwelling radiance in the window region.

Unfortunately, the exact cause of continuum absorption remains somewhat of a mystery. It is generally accepted that this continuum results from the accumulation of absorption in the far wings of many  $\text{H}_2\text{O}$  lines. This far-wing absorption apparently results from self-broadening and foreign collision broadening. Others have suggested that the water vapor dimer  $(\text{H}_2\text{O})_2$  may be responsible for the continuum (Clough et al., 1981).

Nevertheless, several parameterizations have been devised to describe continuum absorption. For instance, Roberts et al. (1976) developed a parameterization in which the continuum absorption coefficient is a function of wavelength, temperature, pressure, and the partial pressure of water vapor. It is a relatively simple parameterization that is popular in other radiative transfer models. In the FASCOD3P model, the continuum absorption coefficient is calculated using molecular densities derived from the atmospheric profiles and self-broadening and foreign broadening coefficients (Clough et al., 1981). Both methods were tried in the FARS CKD Model, and continuum absorption calculations

using the two methods sometimes differed significantly. For further information on the FASCOD3P continuum function, refer to the program documentation.

Since the objective of this work was to test the CKD model against the LBL model for speed and accuracy and NOT to test different continuum calculation methods, our model used the FASCOD3P continuum subroutine in the tests presented in Chapter 5. The subroutine was slightly altered to calculate absorption for only the bandwidth of the PRT-5 radiometer. In future improvements to the model, the differing versions of the continuum calculation should be tested to determine the most appropriate one.

The derivation of simplified and spectrally independent absorption coefficients was indeed long and cumbersome, but it must only be done once. Now the execution of the FARS CKD model can begin.

#### **4.2.3 The Execution Phase**

The execution phase and computer code of the FARS CKD model proceeds in five steps; data input, atmospheric path calculations, transmittance calculations, radiative transfer solution, and output. Again refer to Fig. 4.1 to follow the major steps of the model. This subsection describes each of these steps in varying levels of detail.

##### **4.2.3.1 Data Input**

The data input section begins by reading data from a user input file. This data file allows the user to:

- 1) Specify the upper and lower boundaries and resolution of the model.
- 2) Choose upwelling radiance and its angle and surface emittance.
- 3) Specify the  $\Delta g$  resolution(s).

Next, the program inputs the atmospheric profile from either sounding data or a standard atmosphere. Since soundings contain only water vapor content and not CO<sub>2</sub> or O<sub>3</sub> content, the ozone values are chosen from a standard atmosphere most closely



representing the conditions at the time and place where the sounding was taken. These profiles range from cold and dry subarctic winter (SAW) to warm and moist tropical (TRO). Since  $\text{CO}_2$  is well mixed throughout the lower atmosphere, its mixing ratio is constant throughout each profile. Finally, the program reads the files containing the coefficients for the equivalent  $k$  function at each  $g$  value and pressure level.

#### 4.2.3.2 Path Length Calculation

Before calculating the path lengths for the layer transmittance functions, the heights, temperatures, and pressures of the input profile must be interpolated to the layer boundaries of the model as specified in the user input file. Next, mean layer values for temperature, pressure, and  $\text{H}_2\text{O}$ ,  $\text{CO}_2$ , and  $\text{O}_3$  density are calculated. These mean layer densities ( $\rho_m$ ) are eventually multiplied by the vertical layer depth ( $dz$ ) to obtain the path length for that layer.

#### 4.2.3.3 Transmittance Functions

Calculation of the transmittance functions is at the heart of the radiative transfer process. Since the CKD assumptions have been used to replace the spectral integration of Eq. (4.1), the transmittance for each species is now calculated by:

$$T_v = \int_0^1 \exp\left[-\int_{z_1}^{z_2} k(g_m, p_m, T_m) \rho_m dz\right] dg, \quad (4.3)$$

where  $g_m$ ,  $p_m$ ,  $T_m$ , and  $\rho_m$  refer to the mean layer values. First, a subroutine (see figure 4.1) interpolates for pressure to obtain the mean layer absorption coefficient. Next the layer optical depth,  $k(g_m, p_m, T_m) \rho_m \Delta z$  is calculated. This optical depth is then integrated vertically to obtain the total transmittance for each  $g$  value. This  $T_g$  is somewhat equivalent to a monochromatic transmittance, since  $v$ -space has been replaced by  $g$ -space.

The vertical integration is accomplished simply by multiplying the transmittances of each respective layer:

$$T_{g(total)} = T_{g_1} \times T_{g_2} \times T_{g_3} \times \cdots \times T_{g_{(n-1)}} \times T_{g_n} \quad (4.4)$$

where n represents the number of layers. Finally, the  $T_{g(total)}$  values are integrated through g to get the total atmospheric transmittance for each gas:

$$T_{(total)} = \sum_1^j T_{g(total)} \Delta g \quad (4.5)$$

where j is the number of g values that are integrated over. With the individual species transmittances calculated, the only task that remains is to combine the individual transmittances of H<sub>2</sub>O, CO<sub>2</sub>, O<sub>3</sub>, and water vapor continuum into an overall transmittance function. To do this, one must take into consideration overlapping absorption bands.

#### 4.2.3.4 The Overlap of Absorption Bands

The mean spectral transmittance for the different gases in this study can be expressed as:

$$T_v(1,2,3,4) = 1/\Delta v \int_{v_1}^{v_2} [T_v(1) \times T_v(2) \times T_v(3) \times T_v(4)] dv \quad (4.6)$$

where the numbers 1, 2, 3, and 4 represent H<sub>2</sub>O, CO<sub>2</sub>, O<sub>3</sub> and the water vapor continuum respectively. If the transmittances of the different gases are uncorrelated, then:

$$T_v(1,2,3,4) = \int_{v_1}^{v_2} T_v(1) dv / \Delta v \times \int_{v_1}^{v_2} T_v(2) dv / \Delta v \times \int_{v_1}^{v_2} T_v(3) dv / \Delta v \times \int_{v_1}^{v_2} T_v(4) dv / \Delta v, \quad (4.7)$$

or more simply:

$$T_v(1,2,3,4) = T_v(1) \times T_v(2) \times T_v(3) \times T_v(4). \quad (4.8)$$

Based on this equation, the total transmittance could be expressed in g space as:

$$T_v(1,2,3,4) = \int_0^1 \int_0^1 \int_0^1 \int_0^1 \exp\left\{-\int_0^1 (k_1\rho_1 + k_2\rho_2 + k_3\rho_3 + k_4\rho_4) dz\right\} dg_1 dg_2 dg_3 dg_4 \quad (4.9)$$

Equations (4.8) and (4.9) are based on the assumption that there is no interaction of the gases, but this is not always the case. As shown by Wang and Ryan (1983) and by Fu (1991), when absorption bands overlap, some errors may result from using the multiplication approximation of Eq. (4.8). Nonetheless, the FARS CKD model uses this multiplication approximation in order to save much computational effort. Since the absorption bands in the window region are rather weak, it is unlikely that errors resulting from this approximation are significant. Some tests are presented in Chapter 5 that determine the extent of these errors. Finally, with the total combined transmittance functions computed, the solution of the radiative transfer equation can begin.

#### 4.2.3.5 The Radiative Transfer Equation

Downwelling radiance in the vertical direction may be expressed in z coordinates as:

$$I_v^-(z) = B_v(z_T)T_v(z_T - z_B) - \int_{z_B}^{z_T} B_v(z)[dT_v(z - z_B)/dz]dz, \quad (4.10)$$

where  $I_v^-$  represents downwelling vertical radiance,  $B_v(z_T)$  represents blackbody radiance (Planck function) from the top of the atmosphere,  $z_T$  is the top of the atmosphere (TOA), and  $z_B$  is the earth's surface. Equation (4.10) shows that downwelling radiance at level z is a combination of radiance emitted from the TOA and attenuated to that point (term 1) and emission from the intervening atmosphere (term 2). In the FARS CKD model, the TOA is at 30 km, and since virtually no downwelling IR radiance is emitted at this height, the first

term may be neglected. This simplifies the radiative transfer equation for vertical downwelling radiance to:

$$I_v^-(z) = - \int_{z_B}^{z_T} B_v(z) [dT_v(z - z_B) / dz] dz. \quad (4.11)$$

Equation (4.11) illustrates how critical the calculation of transmittance functions is. The upwelling radiance can be expressed as:

$$I_v^+(z) = B_v(z_B) T_v(z_B - z) - \int_{z_T}^{z_B} B_v(z) [dT_v(z - z_T) / (\mu dz)] dz, \quad (4.12)$$

Where  $\mu$  is the cosine of the azimuth angle. This factor was included since in the future upwelling radiance from all angles will be needed to calculate the IR radiance reflected by the cirrus clouds into the radiometer field of view. The first term in Eq. (4.12) will be the dominant contributor assuming that the earth surface emits as a blackbody in the IR spectrum.

The FARS CKD model uses Eqs. (4.11) and (4.12) to calculate the desired values of  $I_{bc}$  and  $I_{bc}$ . The model utilizes standard integration techniques such as the Simpson rule. This simple technique is sufficient since absorption in the atmospheric window is relatively weak, and slowly changing absorption in adjacent layers will not cause large errors in  $dT/dz$ . One problem that must be dealt with when solving the radiative transfer equation over a wide bandwidth is the dependence of the Planck function,  $B(T, \nu)$ , on wavenumber.

#### 4.2.3.6 The Planck Function Problem

Equation (4.13) shows the dependence of the Planck function on wavenumber:

$$B_\nu(T) = 2h\nu^3 c^2 / [\exp(hc\nu/KT) - 1], \quad (4.13)$$

where  $c$  is the speed of light,  $K$  is the Boltzmann constant, and  $h$  is Planck's constant. Figure 4.3 clearly illustrates this dependence for the bandwidth of the FARS IR radiometer. The figure shows that at a typical atmospheric temperature, the blackbody radiance could change by a factor of two depending on the wavenumber chosen.

A crude solution to this dilemma would be to simply assume that each gas emits evenly across the  $833\text{ cm}^{-1}$  to  $1081\text{ cm}^{-1}$  range. One could then choose the mid-point of this range ( $957\text{ cm}^{-1}$ ) to use in the Planck function. This is not the optimal solution, however. Figure 4.4 shows that each gas does not emit evenly across the spectrum. Carbon dioxide and ozone emit more at higher wavenumbers, whereas water vapor emission is skewed towards lower wavenumbers. The use of a central wavenumber would thus result in an overcalculation of  $\text{CO}_2$  and  $\text{O}_3$  emission and an undercalculation of  $\text{H}_2\text{O}$  emission. The best solution for this problem involves finding an effective emission wavenumber ( $\nu_{\text{eff}}$ ) for each species. Then an overall  $\nu_{\text{eff}}$  is computed based on the emission contribution from each gas.

The calculation of the  $\nu_{\text{eff}}$  for the individual gases involves a relatively simple five step process, which is outlined below.

1. At a given pressure and temperature, integrate the monochromatic radiance spectrally to get the total radiance for the  $833\text{-}1081\text{ cm}^{-1}$  bandwidth ( $I_{\text{Total}}$ ).
2. Integrate spectrally again until  $1/2 I_{\text{Total}}$  is reached. The wavenumber where this occurs is the effective emission wavenumber of that gas for that  $p$  and  $T$ .
3. Repeat this process for a range of pressures and temperatures. Although the radiance values for an individual gas will change significantly based on the  $p$  and  $T$ , the basic shape of the radiance function will remain almost the same. Thus, the effective emission wavenumber,  $\nu_{\text{eff}}$ , will vary only  $10\text{-}15\text{ cm}^{-1}$  among the whole range of atmospheric temperatures and pressures. For example, it is obvious from Fig. 4.4 that the ozone emission is much stronger around  $1000\text{ - }1050\text{ cm}^{-1}$  than at other wavenumbers. Using the procedures in steps 1 and 2, at temperatures ranging from  $180\text{ - }300\text{ K}$  and

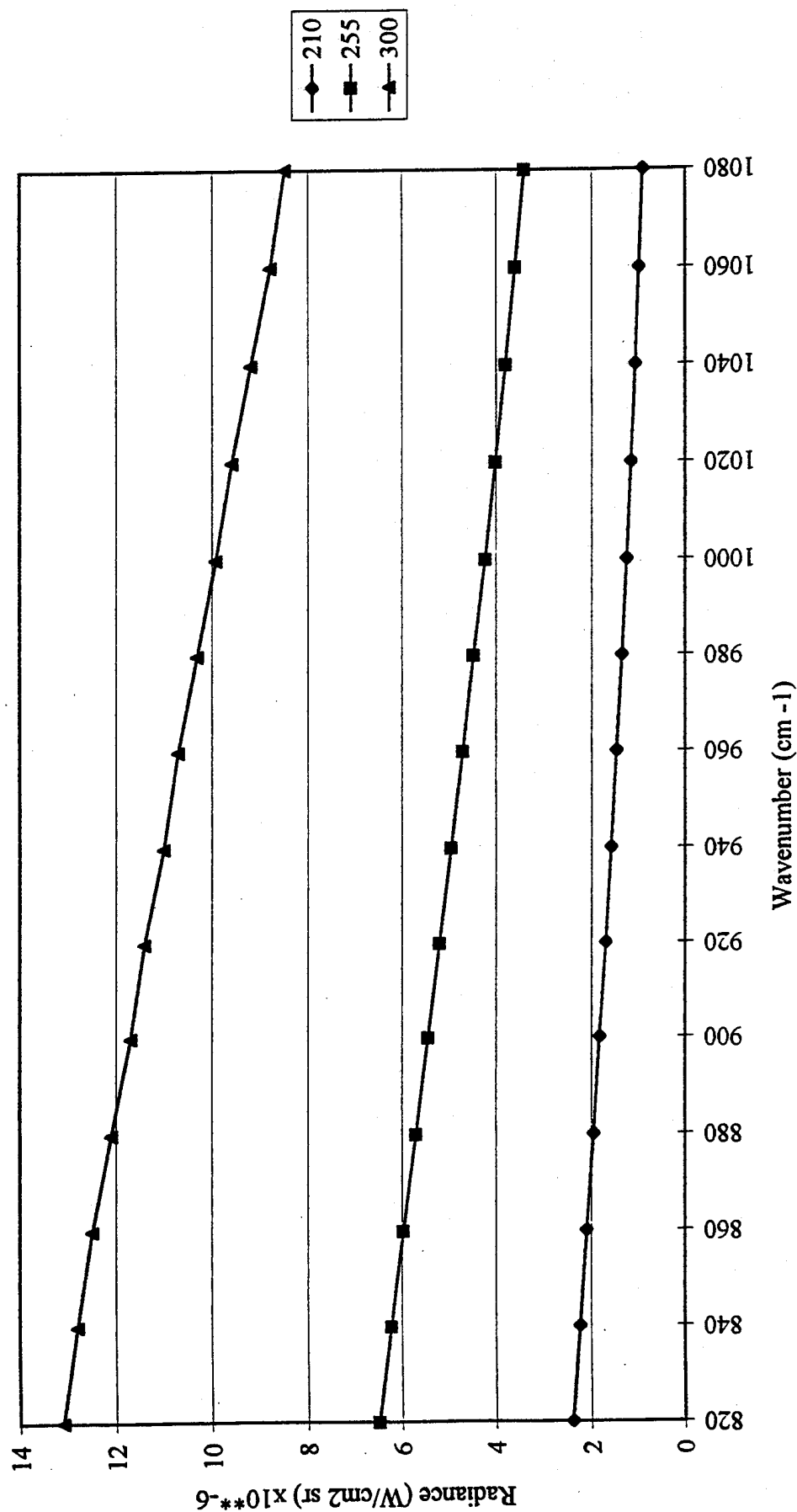


Figure 4.3. The wavenumber dependence of the Planck function over the bandwidth of the FARS IR radiometer for a range of tropospheric temperatures

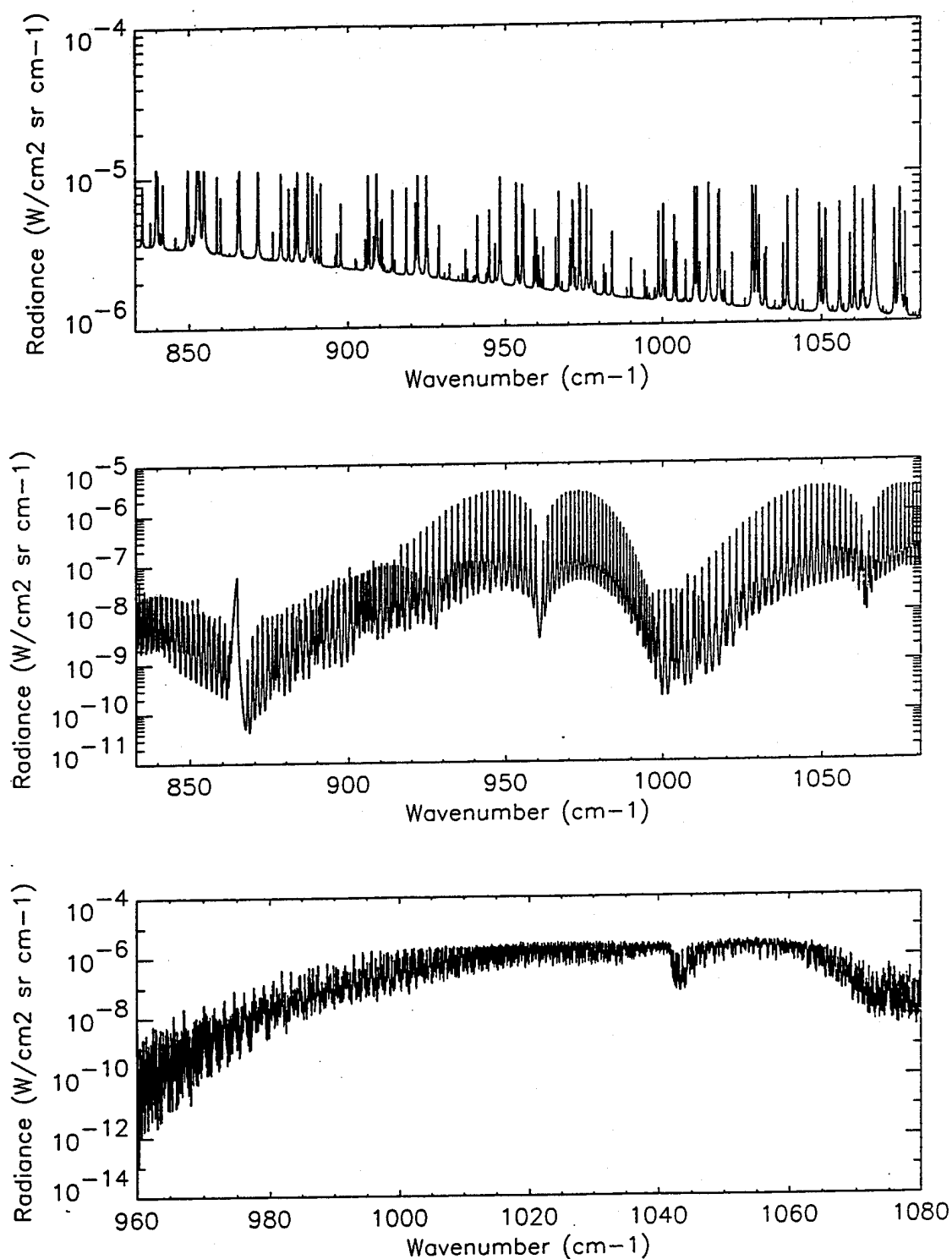


Figure 4.4. Downwelling radiance as a function of wavenumber for the major gas emitters in the spectral region of the FARS IR radiometer. Although the magnitude of the radiances may vary considerably with pressure and temperature, the overall shape of the radiance function for each gas remains fairly constant.

pressures from 12.5 - 1000 mb, the  $\nu_{\text{eff}}$  only varied from about  $1029 \text{ cm}^{-1}$  to  $1043 \text{ cm}^{-1}$ .

4. Once this range is narrowed down, the  $\nu_{\text{eff}}$  is tuned to give the most accurate results for a wide variety of atmospheric conditions. This tuning is done by inserting transmittance functions from the LBL model into the CKD model radiative transfer scheme. The whole range of effective wavenumbers is then inserted into the Planck function. The radiance results from each  $\nu_{\text{eff}}$  is subsequently compared to the radiance values yielded by the LBL model for the same profile. This process was repeated for a range of atmospheric profiles from subarctic winter (SAW) to tropical (TRO).

5. The wavenumber that yielded results closest to the LBL across the range of atmospheric profiles is chosen as the effective emission wavenumber for that gas. This  $\nu_{\text{eff}}$  is the wavenumber used in the Planck function to calculate blackbody radiance for individual gases. For ozone, the  $\nu_{\text{eff}}$  turns out to be  $1037.2 \text{ cm}^{-1}$ .

Chapter 5 shows some tests that outline the magnitude of errors resulting from using the effective wavenumber process just described. As it turns out, this method was quite accurate. However, this did not solve all of the Planck function related problems. Although at first it might appear that this was sufficient to deal with the problem of the  $\nu$  dependence of the Planck function, Fig. 4.5 indicates that it is not. Notice how the overall shape of the downwelling radiance function changes between the midlatitude summer (MLS) and subarctic winter (SAW) profiles. This change occurs because the MLS profile has more water vapor and the SAW profile has more ozone. It is obvious at a glance that the effective emittance wavenumber for the combined gases are significantly different for the two profiles. That is, the combined  $\nu_{\text{eff}}$  varies with the amount of each gas in the atmosphere. This results in significantly erroneous output from the Planck function if the same  $\nu_{\text{eff}}$  were used for both profiles.

The best way to deal with this problem is to find a combined gas effective emission wavenumber which is based on: (1) the percentage of absorption from each gas, and (2)



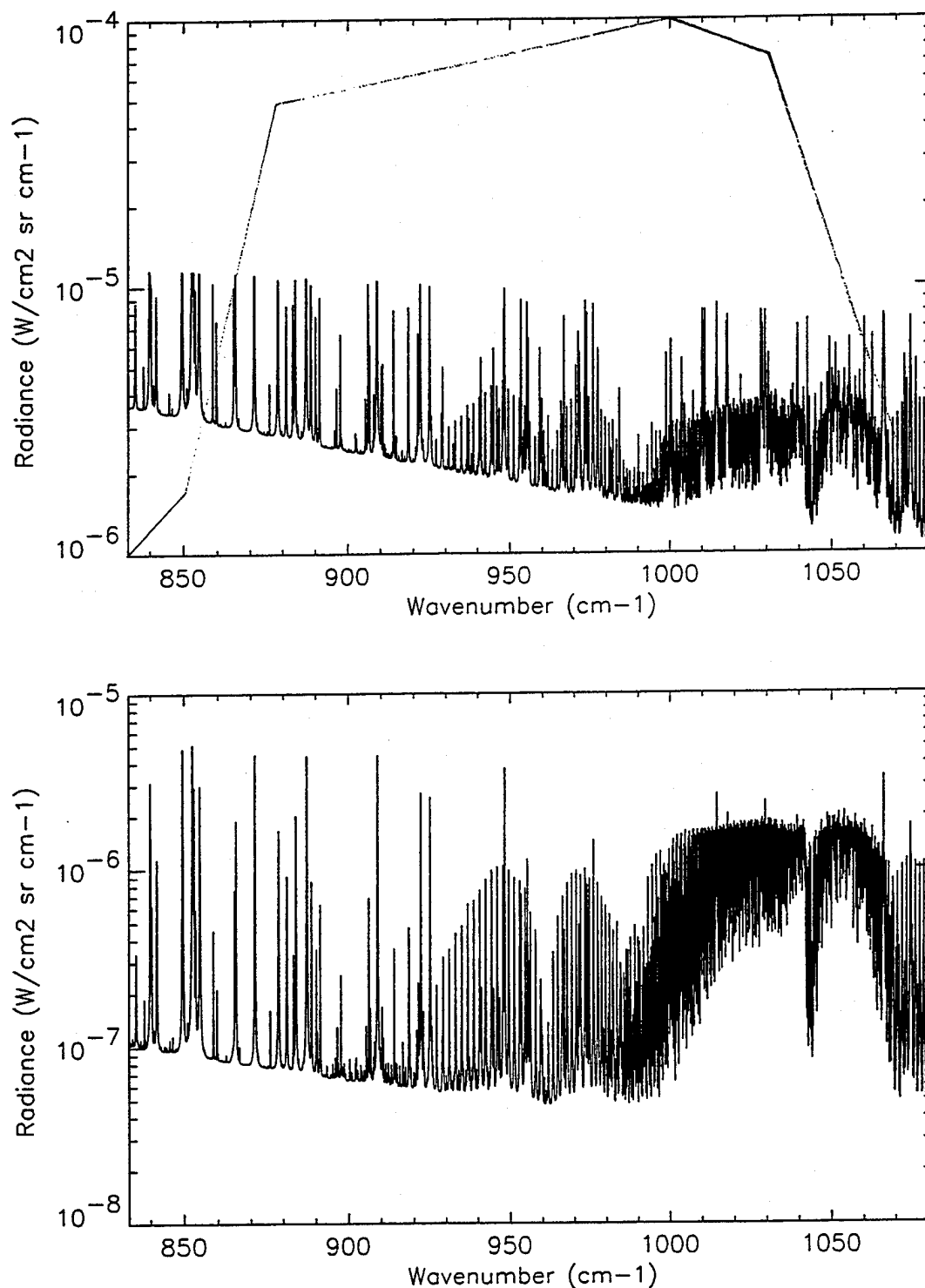


Figure 4.5. Downwelling radiance in for the major emitting gases ( $\text{H}_2\text{O}$ ,  $\text{CO}_2$ ,  $\text{O}_3$ , and the water vapor continuum) in the spectral region of the FARS IR radiometer (see inserted filter function) for; (a) downwelling radiance in a midlatitude summer atmospheric profile, and (b) downwelling radiance in a subarctic winter atmospheric profile. The emission spectrum varies considerably for the combined gases.

the distance of the  $v_{\text{eff}}$  for each gas from the center of the radiometer's bandwidth ( $957.2 \text{ cm}^{-1}$ ). The equation for the combined gas effective emission wavenumber is:

$$v_{\text{eff(combined)}} = A_1 (v_{\text{eff(1)}} - 957.2 \text{ cm}^{-1}) + A_2 (v_{\text{eff(2)}} - 957.2 \text{ cm}^{-1}) + A_3 (v_{\text{eff(3)}} - 957.2 \text{ cm}^{-1}) + A_4 (v_{\text{eff(4)}} - 957.2 \text{ cm}^{-1}), \quad (4.14)$$

where  $A$  is the absorption ( $1 - T$ ) of each gas,  $957.2 \text{ cm}^{-1}$  is the center of the FARS IR radiometer bandwidth, and the numbers 1, 2, 3, and 4, represent  $\text{H}_2\text{O}$ ,  $\text{CO}_2$ ,  $\text{O}_3$ , and the water vapor continuum respectively. Since the tuning was already done when determining the  $v_{\text{eff}}$  of each individual gas, no further tuning is necessary. Equation (4.14) proved to be an effective way of dealing with the Planck function problem as results in Chapter 5 will show.

#### 4.2.4 The Postexecution Phase

After the radiative transfer equation is solved, the resulting radiance values are stored for further analysis. The transmittance and radiance functions have been tested against the FASCODE3 LBL model, since this LBL model is the most accurate method of calculating clear sky atmospheric transmittance and radiance. The various quantities tested are single gas transmittance, combined transmittance, single gas radiance (up and down), combined radiance (up and down), and emittance. Chapter 5 outlines these tests as well as some g-space and vertical resolution tests. As the FARS CKD model is further developed to include cirrus cloud scattering phase functions, output radiance will be used to solve Eq. (1.1) and obtain the emittance of cirrus clouds.

## **CHAPTER 5**

### **CKD MODEL PERFORMANCE VERSUS LINE-BY-LINE MODEL**

The best way to assess the accuracy of the FARS CKD model is to compare its results with those from a line-by-line (LBL) model. As discussed earlier, line-by-line methods are the most accurate means known to solve radiative transfer problems. The LBL model chosen as the standard for this research was FASCD3P, the latest version of FASCODE produced by the Air Force Geophysics Laboratory. For clarification during the following comparisons, the FASCD3P model will be referred to as the LBL model, and the FARS CKD model will be referred to simply as the CKD model. Since this LBL model is known to very accurately calculate line-of-sight radiances and transmittances under most atmospheric conditions, the comparisons between the CKD model and LBL model should provide an excellent measure of the true accuracy of the our model. For this reason, when CKD and LBL results are compared in sections 5.2-5.4, the LBL results are considered the target, and the terms "accurate" and "error" suggest how closely the CKD model results resemble the LBL model results.

#### **5.1 Testing Methods**

The CKD model was tested against the LBL results using four different standard atmospheric profiles including tropical (TRO), midlatitude (MLS), US Standard (USS), and subarctic winter (SAW) profiles. Results for all four profiles are not always discussed for the sake of brevity. In the transmittance and radiance tests, the models were compared looking from the surface to various altitudes up to 30 km. The radiance and transmittance

calculations for individual gases were compared at only 6, 10, 14, and 30 km. These represent the heights of low, middle, and high cirrus clouds and the top of the model's atmosphere. An error analysis is presented along with the results. The sources of various errors are indicated and suggestions of how these errors might be reduced are also presented.

There are intentionally no comparisons presented for the CKD versus vs LBL model continuum transmittances since the same function was used in each model to calculate the continuum transmittance. Only slight errors were introduced into the continuum transmittance as a result of the modifications made to the continuum subroutine when incorporating it into the CKD model.

An experiment was also devised to estimate the error in emittance resulting from the CKD model. Although it is not possible to exactly calculate the emittance error without knowing the scattering characteristics of the cloud, a method is presented that yields a good estimate.

In addition to downwelling radiance, the CKD model also calculates upwelling radiance from the earth surface at any angle. A comparison of the upwelling radiances at several different angles is presented here also. Finally, results from height resolution and g resolution sensitivity tests are briefly presented. The computational gain resulting from coarse resolution is weighted against the resulting loss in accuracy to determine the optimum resolution for the CKD model.

In the following transmittance, radiance, and emittance comparisons, the CKD model was run with a z resolution of 1.0 km and a  $\Delta g$  resolution of 0.01 at  $g < 0.9$  and a  $\Delta g$  of 0.001 at  $g > 0.9$ . The LBL model was run with a z resolution of 1.0 km and a v resolution that varied with height so that the spectral resolution was four samples per mean Voigt half-width.

## 5.2 Transmittance Comparison

### 5.2.1 Individual Gas Comparison

The first quantity tested was the transmittance of individual gases and all the gases combined. The CKD model calculated the band transmittance quite accurately for all profiles and all heights. Table 5.1 compares the individual and total transmittance values at 6, 10, 14, and 30 km. Transmittance errors for  $\text{H}_2\text{O}$  and  $\text{CO}_2$  were less than 0.10% for all cirrus cloud altitudes, and less than 0.33% for the model ceiling. Errors for ozone were slightly larger as expected but still less than 0.50% in all cases. This indicates that the method for acquiring the equivalent  $k$  functions,  $k(g)$ , was quite satisfactory, and that the  $k$ -distribution method is very accurate for determining absorption properties of individual gases in the atmospheric window.

The concern about using the multiplication approximation to deal with the overlap of absorption lines of different gases (see section 4.2.3.4) turned out to be unfounded. Errors resulting from the multiplication approximation were very small. Table 5.1 illustrates the transmittance errors for the combined gases (lines only). Referring to the surface-to-14 km SAW profile results for example, the individual species errors for  $\text{H}_2\text{O}$ ,  $\text{CO}_2$ , and  $\text{O}_3$  lines are 0.0%, -0.02%, and -0.27% respectively. Summing these errors results in a total error of -0.29%. However, the actual line total error in this case was -0.39%. Thus, a -0.10% error resulted from the multiplication approximation. Once again the agreement between the LBL and CKD models was very good, with transmittance errors of less than 0.40% in all cases.

Sometimes, the multiplication approximation errors canceled out errors in the individual gases. For example, in the 0-30 km MLS profile, the individual gases had errors of 0.13%, -0.24%, and -0.36%. Thus, a combined error of -0.73% would be expected without the multiplication approximation. However, the CKD model yielded a combined error of only -0.19%, because the multiplication error of 0.54% canceled the individual

Table 5.1  
Individual Gas Transmittance Errors

Lower	Upper	H <sub>2</sub> O	CO <sub>2</sub>	O <sub>3</sub>	All lines
U. S. Standard Atmosphere					
0	6	-0.05%	-0.03%	-0.12%	-0.19%
0	10	-0.05	-0.03	-0.16	-0.25
0	14	-0.04	-0.02	-0.25	-0.37
0	30	-0.33	-0.25	-0.38	-0.20
Midlatitude Summer Atmosphere					
0 km	6 km	0.02%	-0.05%	-0.14%	-0.17%
0	10	0.01	-0.06	-0.21	-0.28
0	14	-0.06	-0.04	-0.28	-0.38
0	30	-0.13	-0.24	-0.36	-0.19
Subarctic Winter Atmosphere					
0 km	6 km	-0.05%	-0.04%	-0.09%	-0.16%
0	10	-0.03	-0.02	-0.20	-0.29
0	14	0.00	-0.02	-0.27	-0.39
0	30	0.00	-0.05	-0.42	-0.30
Tropical Atmosphere					
0 km	6 km	0.13%	-0.04%	-0.08%	-0.07%
0	10	0.11	-0.04	-0.18	-0.16
0	14	0.11	-0.04	-0.21	-0.20
0	30	0.01	-0.22	-0.32	-0.08

gas transmittance errors.

The major source of error in computing transmittance functions was the continuum function. As discussed in Chapter 4, the continuum function used in the CKD model was the same one used in the LBL model, so one would expect no error in continuum computation. However, some slight modifications were made to the function so it would work specifically for the IR radiometer bandwidth. These modifications led to some small errors. The lines in Figure 5.1 represent transmittances between the surface and various heights up to 30 km. The figure clearly shows that the agreement between the two models is very good in all but the tropical atmosphere, where the CKD model underestimated the transmittance at all levels. Due to the method in which the LBL model incorporates continuum absorption into the total absorption calculation, it is impossible to explicitly compare the continuum transmittance functions of the LBL and CKD models. The errors resulting from the continuum function are calculated instead by subtracting errors in the "lines only" column of Table 5.1 from the errors in the "total transmittance" displayed in Fig 5.2.

The error resulting from the continuum function alteration seem to depend largely upon the amount of water vapor in the profile. Continuum errors in the relatively cold and dry USS profile range between -0.01% and +0.19%. The continuum error in the TRO profile is much larger ranging from -1.75% at 6 km to -0.58% at the top of the model atmosphere. Although the data already taken with the lidar/radiometer ensemble are in much drier atmospheres, these potentially large errors may have to be reduced if LIRAD experiments are done in a tropical environment in the future.

### 5.2.2 Total Transmittance Comparison

Figure 5.1 shows comparisons between the LBL and CKD model transmittance functions for all four atmospheric profiles. The lines in Fig. 5.1 represent transmittances

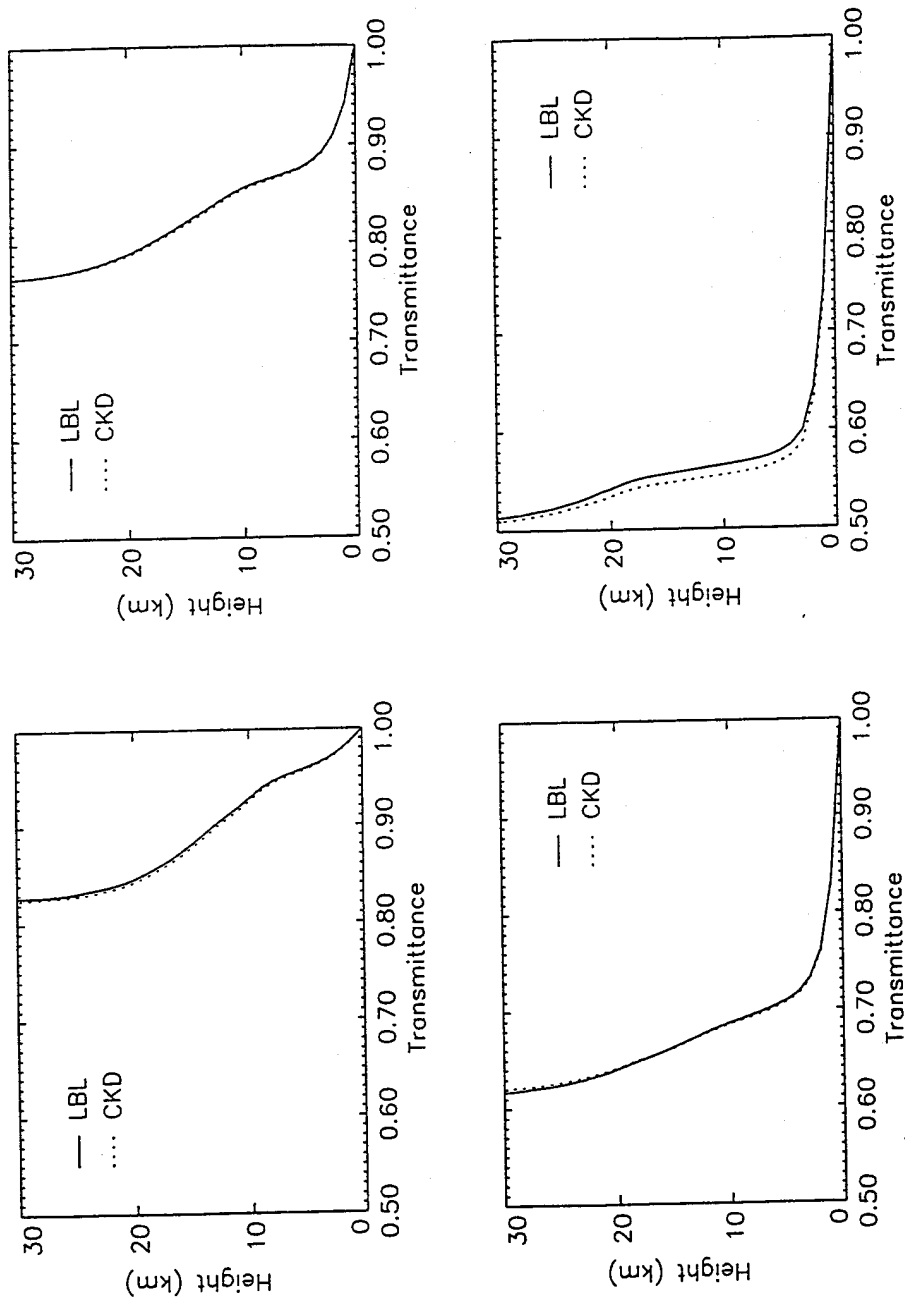


Figure 5.1. Comparison of the FARS CKD and FASCODE3 LBL models transmittance calculations for; (a) subarctic winter, (b) US Standard, (c) midlatitude summer, and (d) tropical atmospheric profiles.



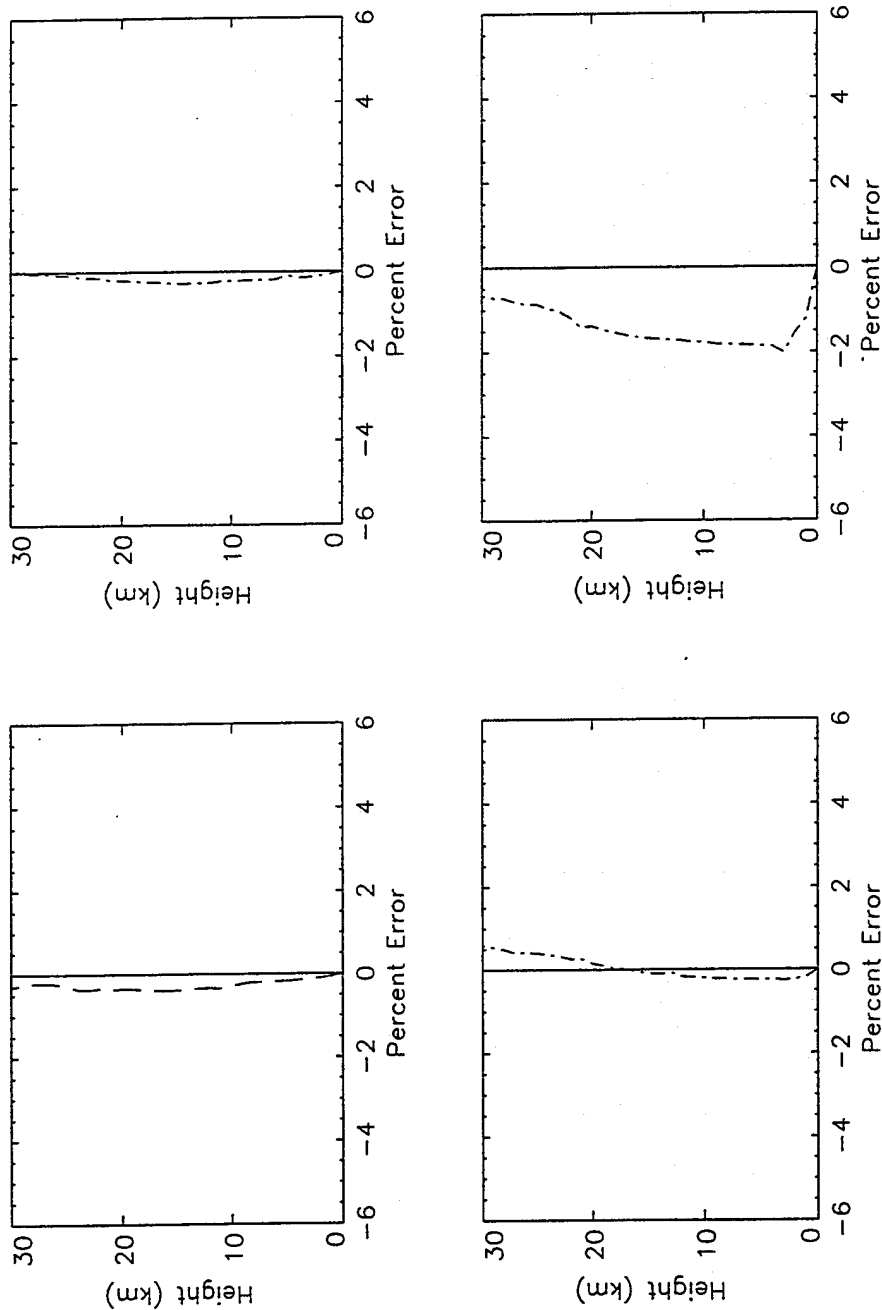


Figure 5.2. Transmittance errors from 0 to 30 km for the FARS CKD model for; (a) subarctic winter, (b) US Standard, (c) midlatitude summer, and (d) tropical atmospheric profiles.

between the surface and various heights up to 30 km. The figure clearly shows that the agreement between the two models is very good in all but the tropical atmosphere, where the CKD model tends to underestimate the transmittance at all levels. This error in the tropical profile was largely due to modifications made to the continuum function when incorporating it into the CKD model. Figure 5.2 shows the CKD model error as a function of height. This figure also clearly demonstrates the outstanding performance of the CKD model. In all but the tropical profile, the transmittance function errors were less than half a percent at all heights.

### 5.3 Radiance Comparisons

Calculation of the downwelling radiance values introduces other potential errors. As described in Chapter 4, the transmittance functions are applied to the radiative transfer equation to calculate total downwelling radiance at the surface. Recall, the CKD model is utilized to compute the quantities  $I_{\text{sr}}$ ,  $I_{\text{ec}}$ , and  $I_{\text{cls}}$ . The values shown in Table 5.2 represent individual gas and combined gas downwelling radiance errors. Figure 5.3 shows the downwelling surface radiance contribution for a clear sky in several atmospheric profiles, as computed by the CKD (dotted lines) and the LBL (solid lines) models. Figure 5.4 shows the CKD model errors for these same profiles.

#### 5.3.1 Total Downwelling Radiance Comparisons

Figure 5.3 illustrates how the clear sky radiance is much greater in the warm moist environments such as the tropical profile than in the cold and dry environments. A comparison of Fig. 5.3(d) with 5.3(a) shows that the tropical atmosphere up to 30 km emits over  $10.5 \text{ W/m}^2\text{sr}$ , while the subarctic winter atmosphere emits only about  $0.9 \text{ W/m}^2\text{sr}$ . In other words, the tropical atmosphere emits over 10 times as much downwelling radiation as the subarctic winter atmosphere. Figure 5.3 also shows where in the atmosphere this radiation comes from. In the warm and moist MLS (Fig. 5.3(c))

Table 5.2  
Individual Gas Radiance Errors

Lower	Upper	H <sub>2</sub> O	CO <sub>2</sub>	O <sub>3</sub>	All Lines
U.S. Standard					
0 km	6 km	-0.68%	-1.29%	-1.31%	0.43%
0	10	-0.49	-1.20	-2.30	0.28
0	14	-0.38	-1.14	-1.62	0.41
0	30	-0.38	-1.05	-1.91	-0.10
Midlatitude Summer Atmosphere					
0 km	6 km	0.27%	-0.11%	-0.31%	1.84%
0	10	0.41	-0.09	-1.38	1.78
0	14	0.60	-0.07	-1.86	1.59
0	30	0.60	0.00	-2.02	1.30
Subarctic Winter Atmosphere					
0 km	6 km	6.28%	4.54%	0.66%	3.60%
0	10	6.38	4.36	0.03	2.65
0	14	6.40	4.47	0.52	2.45
0	30	6.45	4.59	-0.86	0.90
Tropical Atmosphere					
0 km	6 km	-1.62%	-0.75%	0.11%	0.31%
0	10	-1.40	-0.73	-0.51	0.53
0	14	-1.28	-0.69	-1.01	0.45
0	30	-1.28	-0.66	-0.53	0.46

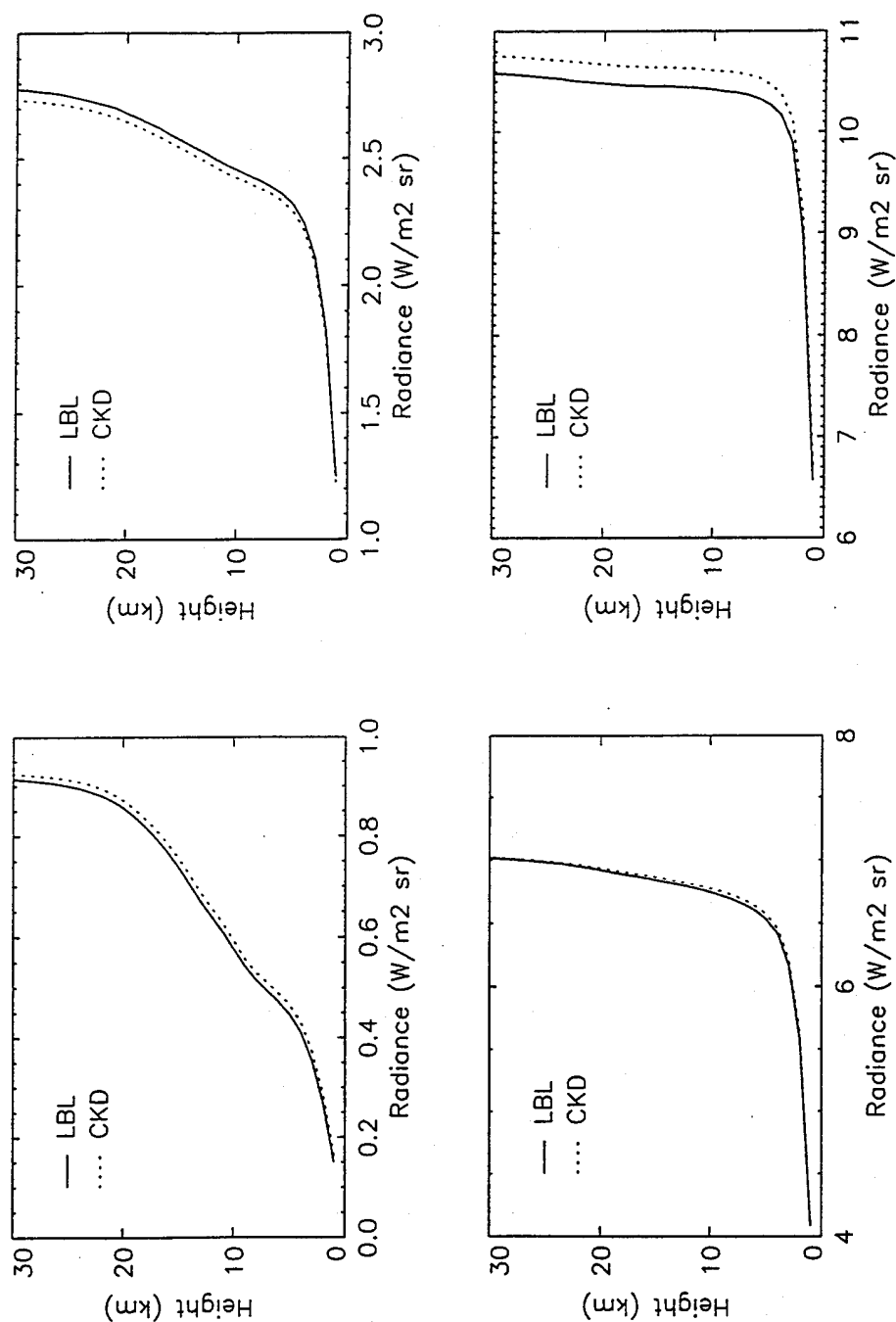


Figure 5.3. Comparison of FARS CKD model and FASCODE3 LBL model downwelling vertical radiance calculations for; (a) subarctic winter, (b) US Standard, (c) midlatitude summer, and (d) tropical atmospheric profiles.

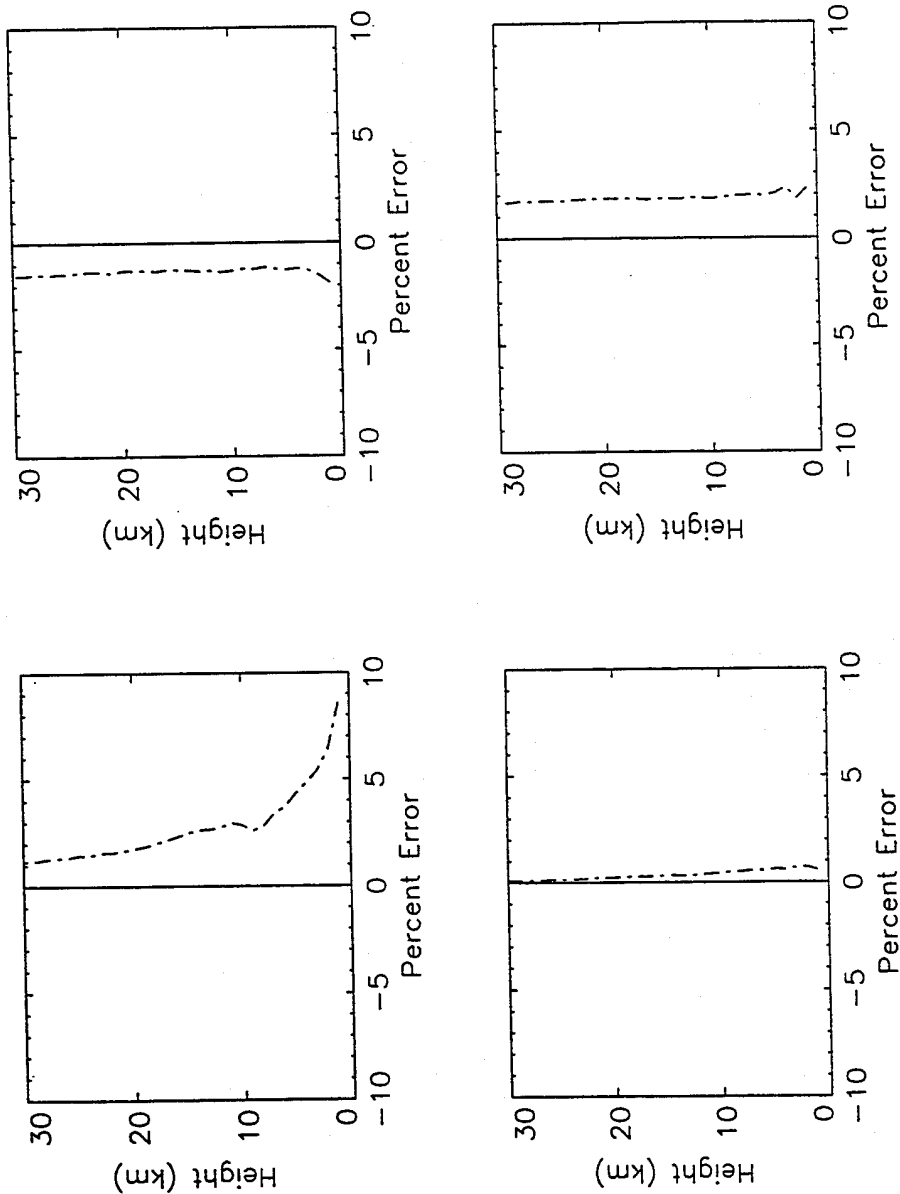


Figure 5.4. Downwelling vertical radiance errors from 0 to 30 km for the FARS CKD model for; (a) subarctic winter, (b) US Standard, (c) midlatitude summer, and (d) tropical atmospheric profiles.

and TRO (Fig. 5.3(d)) atmospheres, most of the radiance comes from the bottom 5 km of the atmosphere, with almost no contribution above this level. In the SAW (Fig 5.3(a)) and USS (Fig 5.3(b)) profiles, there are still significant radiance contributions at levels up to 20 km. It is apparent that some type of correction may have to be implemented to account for emission above the cloud level. This issue is addressed at the end of this chapter.

Overall, the CKD model was quite accurate at calculating downwelling atmospheric radiance. The CKD model overestimated radiance values in the SAW, MLS, and TRO atmospheres, but underestimated the radiance in the USS atmosphere. There is no apparent physical reason for this. This pattern is likely due to the tuning of the  $v_{\text{eff}}$  values as described in Chapter 4. Total downwelling radiance errors for the four atmospheric profiles are shown in Figure 5.4. The model appears to perform best in midlatitude climates as demonstrated by the USS (Fig. 5.4(b)) and MLS (Fig. 5.4(c)) profile results. This was one of the desired features of the model. The CKD model was able to calculate radiances within 1.5% and 0.5% for these profiles, respectively. Radiance errors tended to be considerably larger for the SAW profile especially in the bottom portion of the troposphere. Errors for the SAW calculations were as large as 8.6% at 1 km, but tapered off rapidly to around 3.5% at the lowest expected cirrus cloud level. This radiance error in the cold and dry SAW atmosphere is less an area of concern than if it were in a MLS or TRO atmosphere. The atmospheric emission is much smaller in the SAW profile and thus affects the total measured radiance much less. Despite the rather large transmittance errors in the TRO profile, the CKD model still managed to calculate  $I_{\text{cls}}$  within 2.0% of the LBL model. This was a rather fortunate result of the cancellation of some of the transmittance error by the Planck function error. Considering the wide band over which radiance is calculated and the computational savings, based on these results, the CKD model would have to be considered a very successful substitute for the LBL model.

### 5.3.2 Individual Gas Comparison

The errors in the FARS CKD model radiance calculations come primarily from three sources shown in Eq. (5.1): (1) errors carried over from the transmittance function,  $E_T$ , (2) errors from integration methods,  $E_{NP}$ , and (3) errors from the Planck function approximation,  $E_P$ :

$$E_{ckd} = E_T + E_{NP} + E_{ibl} . \quad (5.1)$$

Tables 5.1 - 5.3 provide some insight into the relative magnitude of each of these errors. The Planck function errors for total downwelling radiance were calculated using the following method. First, the total downwelling radiances were calculated for each level using the CKD model. Next, the radiance calculation routine in the CKD model was run using transmittance functions from the LBL model. This was done to "eliminate" errors carried over from the CKD model transmittance calculations. In other words, any radiance errors should then result from integration or the Planck function approximation. These resulting radiance values were called  $I_P$ . Each of these radiances was compared with the LBL radiance,  $I_{ibl}$ , to get the total CKD model radiance error, (as shown in Fig. 5.2) and the radiance error resulting from the Planck function approximation,  $E_P$ . The difference between these two is simply the error resulting from sources other than the Planck function approximation,  $E_{NP}$  (primarily from integration approximations). Since the individual species transmittances were calculated at only four levels, it is not possible to repeat this analysis for the individual species errors. Table 5.3 shows that the Planck function approximation described in Chapter 4 was successful in reducing Planck function errors to less than 2.5% for all of the tested atmospheric profiles.

The Planck function approximation was tuned so that resulting errors were smallest for mid-latitude type atmospheres, since they are the most likely to be encountered. Thus the MLS profile has Planck function approximation errors of less than

Table 5.3

## Errors Resulting from the Planck Function Approximation

Height	SAW	USS	MLS	TRO
5 km	+0.11%	-2.05%	-0.04%	-0.69%
10	-1.08	-2.40	-0.14	-0.67
15	-0.91	-2.35	-0.21	-0.67
20	-0.99	-2.25	-0.22	-0.65
25	-0.92	-2.23	-0.21	-0.65
30	-1.27	-2.24	-0.20	-0.67

0.25%. In three of the four profiles tested, the Planck function approximation errors somewhat canceled the integration, CKD approximation, and multiplication approximation errors. Therefore, in all but the SAW profile, the Planck function approximation error fortuitously resulted in a reduction of the total error.

#### 5.4 Upwelling Angle Varying Radiance Results

The CKD model was also designed to calculate upwelling radiance at any level up to 30 km and any angle up to  $80^\circ$ . This is necessary so that  $I_m$  can be corrected for the amount of earth-emitted energy scattered by a cirrus cloud into the radiometer receiver field of view ( $I_{sr}$ ). Table 5.4 shows comparisons of the LBL and CKD models upwelling radiance calculations. The models were compared at several different zenith angles for the USS and MLS profiles using a 1 km height resolution. The values in Table 5.4 represent upwelling radiance from the earth surface and intervening atmosphere to 10 km for the stated angle. The values below the radiances represent the percent difference between the CKD and LBL model radiances. In all cases the CKD model overestimated the radiances, and although errors were larger than expected they never exceeded 4%.

Although this portion of the model is important, its accuracy is not as critical as



Table 5.4  
Upwelling Radiance ( $\text{W/m}^2$ ) - Surface to 10 km

Angle (degrees)	USS Radiance		MLS Radiance
0	21.61	CKD	23.51
	21.15	LBL	22.98
	2.17%	Error	2.30%
10	21.50	CKD	23.52
	21.12	LBL	22.97
	1.80%	Error	2.40%
20	21.45	CKD	23.50
	21.11	LBL	22.92
	1.61%	Error	2.53%
30	21.21	CKD	23.40
	21.05	LBL	22.83
	0.76%	Error	2.50%
45	21.04	CKD	23.21
	20.89	LBL	22.60
	0.72%	Error	2.70%
60	21.05	CKD	23.02
	20.34	LBL	22.15
	2.48%	Error	3.93%

the downwelling radiance for several reasons. First, the earth's surface emits much more IR radiation than the atmosphere; thus errors resulting from the atmospheric model are likely to be overshadowed by Planck function errors. Second, the scattered upwelling radiance is only a secondary contributor to  $I_m$ , amounting to less than 10% of the total. Finally, the errors resulting from scattering calculations in the cirrus cloud are likely to far exceed the atmospheric emission errors. Additionally, the larger errors at the higher zenith angles in the MLS profile are of less concern since most of the backscatter comes from radiance emitted in the near-vertical direction. This is due to the shape of the phase function of cirrus ice crystals at the 9.25-11.0  $\mu\text{m}$  wavelengths. So, the 1-4% errors in the upwelling radiance calculations of the CKD model are concluded to be acceptable.

## 5.5 Emittance Results

The ultimate goal of the LIRAD method is to provide accurate estimations of cirrus cloud emittance. Although calculating cirrus emittance is beyond the scope of this work, there is a way to estimate the error in the emittance values resulting from the CKD model. The following experiment was devised to yield such an estimate.

Refer to the conceptual model of the LIRAD problem in Figs. 1.2a and 1.2b. Neglecting the minor contributions from surface reflected radiance,  $I_{sr}$ , or multiple scattered in cloud radiance,  $I_{ms}$ , the radiance measured at the earth's surface by a radiometer would be:

$$I_m = I_c T_{bc} + I_{cls}, \quad (5.2)$$

where  $T_{bc}$  is the transmittance of the atmosphere between the cloud and ground. Since  $I_c = \epsilon \cdot I_{bb}$ , then:

$$I_m = \epsilon I_{bb} T_{bc} + I_{cls}. \quad (5.3)$$

Using emittance values ranging from 0.05 to 1.0,  $I_m$  is calculated using values of  $T_{bc}$  and  $I_{bc}$  from the LBL model. Next, Eq. (5.2) is rearranged to calculate  $I_c$ :

$$I_c = (I_m - I_{bc}) / T_{bc} \quad (5.4)$$

Using the  $I_m$  just calculated from the LBL model, and the  $T_{bc}$  and  $I_{bc}$  values from a CKD model,  $I_c$  is computed. Next, this  $I_c$  computed from the CKD model is divided by  $I_{bb}$  to get the emittance value from the CKD model,  $\epsilon_{ckd}$ . Finally,  $\epsilon_{ckd}$  is compared to the emittance values originally used to calculate  $I_m$ . This yields the estimated emittance error caused by the CKD model as opposed to a LBL model:

$$\text{Emittance Error} = 100 \times (\epsilon_{ckd} - \epsilon_{lbl}) / \epsilon_{lbl} \quad (5.5)$$

This procedure is repeated for  $\epsilon_{lbl}$  values ranging from 0.05 to 1.0 and for several cloud heights representative of typical cirrus clouds in that atmospheric profile. Keep in mind that  $I_{sr}$  and  $I_{ms}$  not be included in these calculations (since the clouds have not yet been added to the model). Therefore, the resulting values will not exactly show errors resulting from the completed CKD model. However, since the excluded components are of only secondary importance, the error estimates from Eq. (5.5) should be a good indicator of how accurate the CKD model will prove to be at calculating cloud emittances.

Figures 5.5, 5.6, and 5.7 show the CKD model emittance error estimates as a function of the "true" cirrus cloud emittance ( $\epsilon_{lbl}$ ) and cloud height. Figure 5.5 shows emittance errors for a typical range of USS cirrus clouds heights, while Figs. 5.6 and 5.7 show the same errors for a typical range of cirrus cloud heights in SAW and MLS atmospheres, respectively. The most noticeable feature in both figures is that the errors are highly dependent on the emittance of the cloud. This is certainly understandable. As  $\epsilon$  decreases in Eq. (5.1),  $I_c$  gets smaller and  $I_{bc}$  becomes the dominating term. Therefore, overall cloud emittance errors will be more susceptible to errors in the computation of

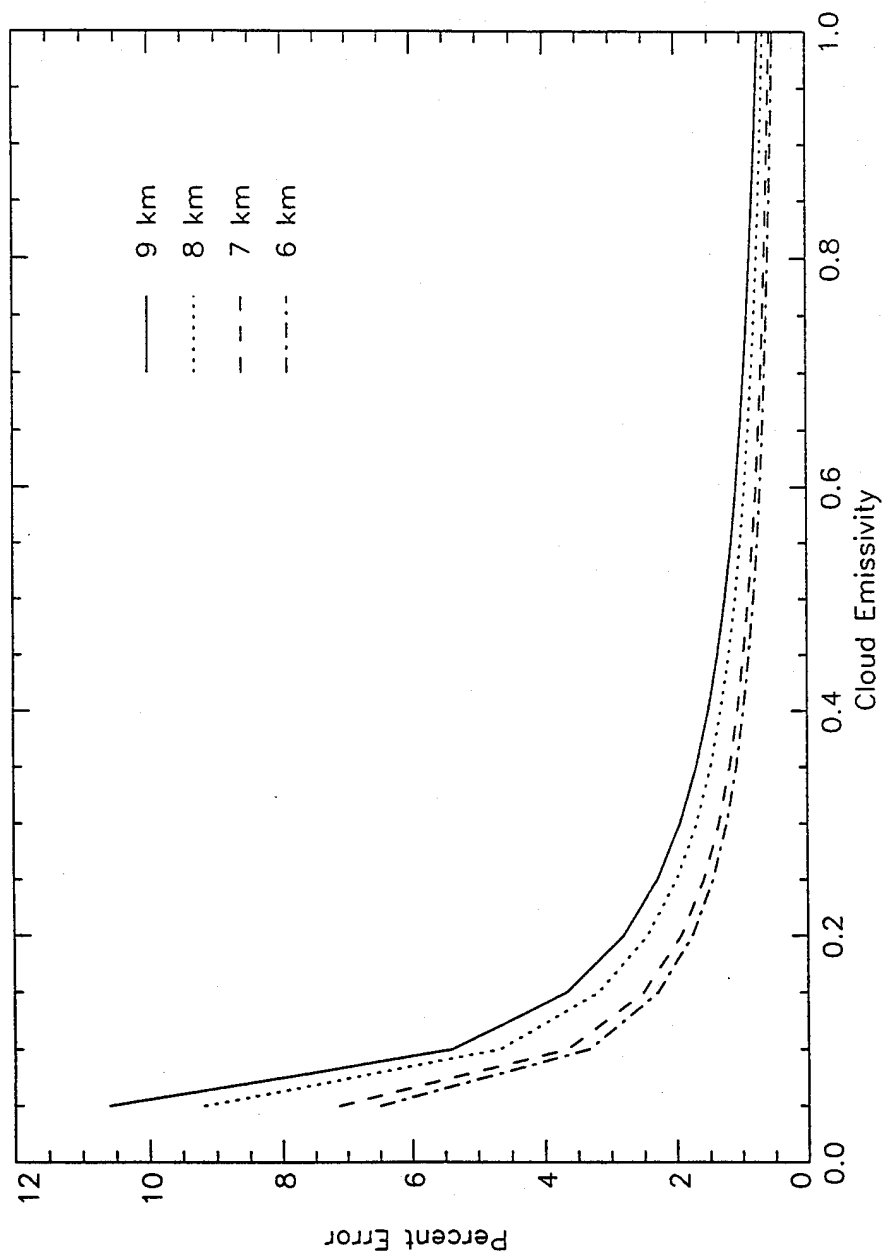


Figure 5.5. Emittance errors from the FARS CKD model for various emittances and typical cirrus cloud heights in a US Standard atmospheric conditions. Cirrus mid-cloud heights are shown by the various lines (see inserted legend).

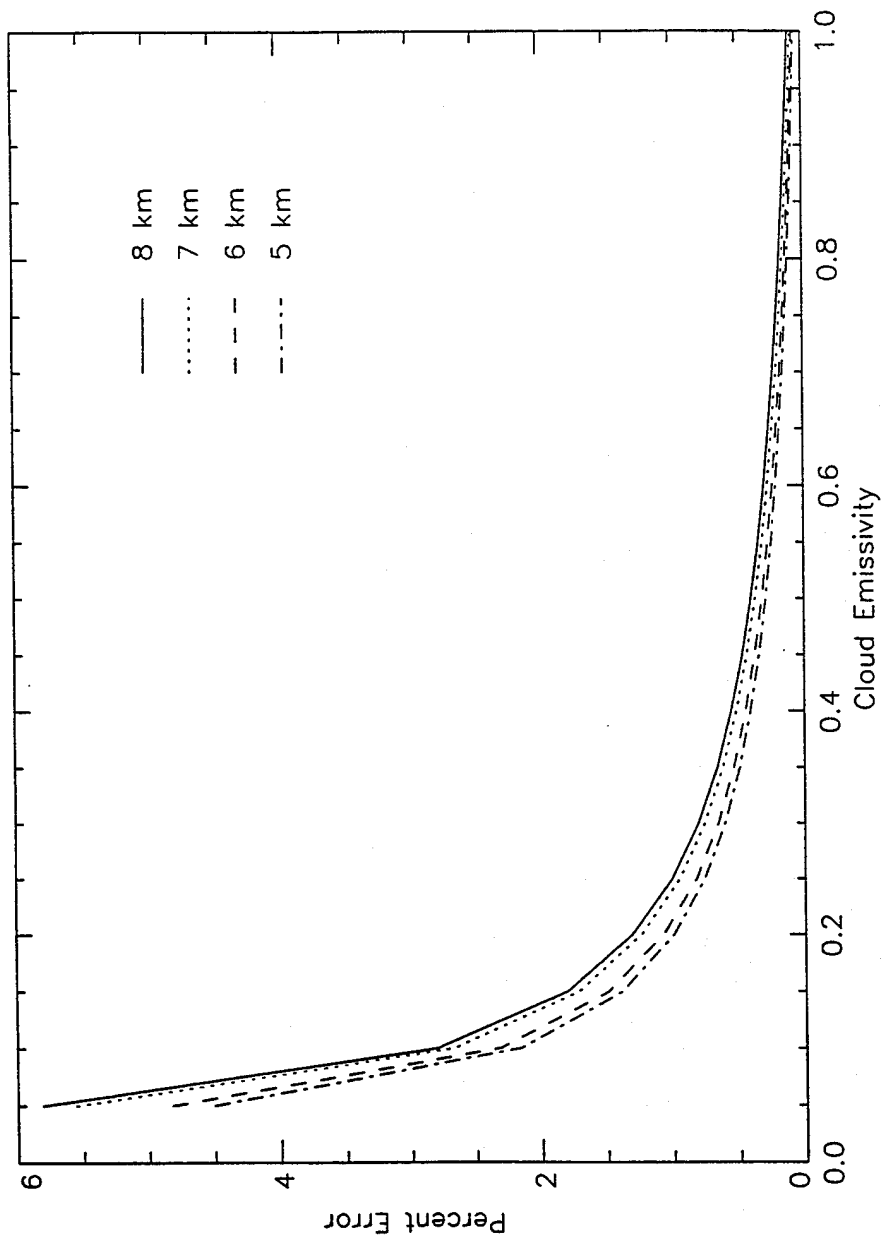


Figure 5.6. Emittance errors from the FARS CKD model for various emittances and typical cirrus cloud heights in a subarctic winter atmospheric profile. Cirrus mid-cloud heights are shown by the various lines (see inserted legend).

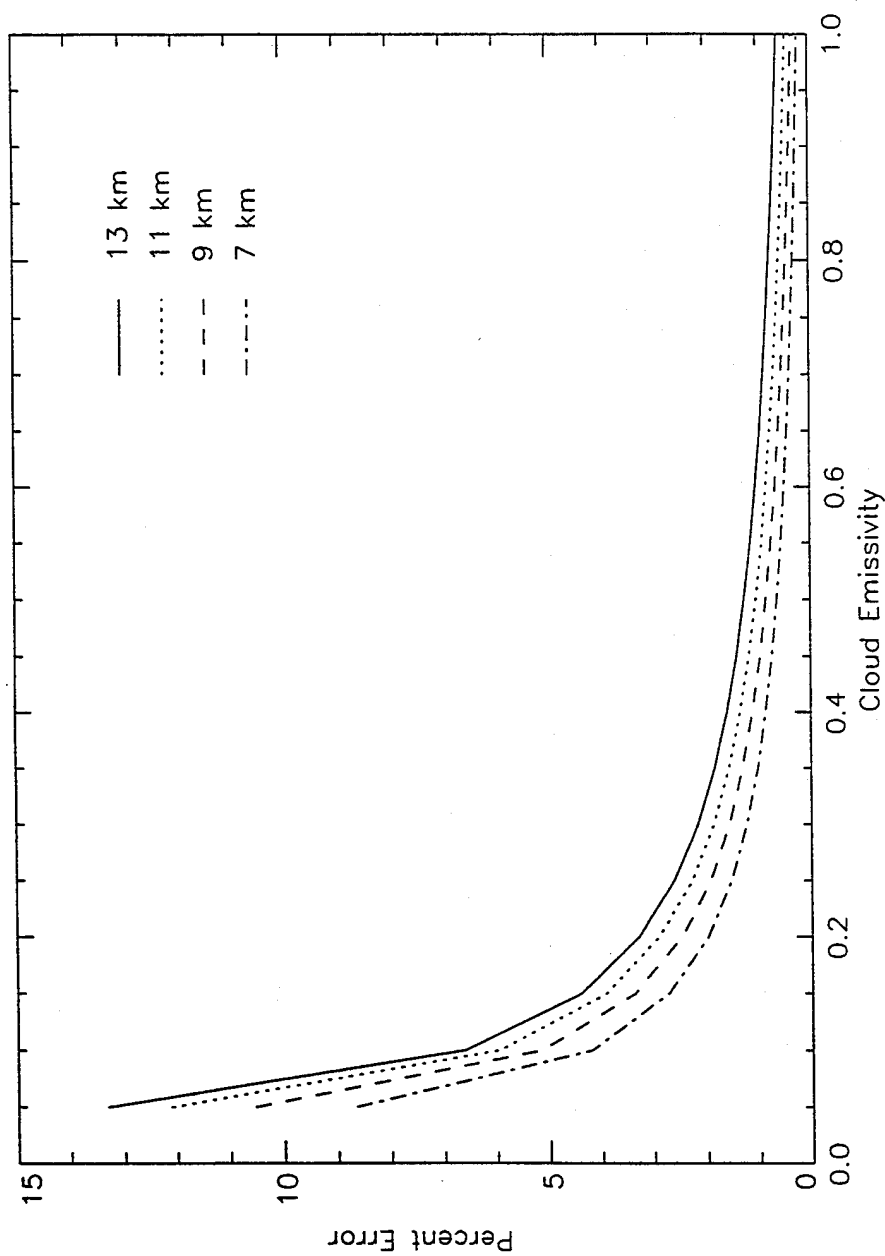


Figure 5.7. Emissance errors from the FARS CKD model for various emissances and typical cirrus cloud heights in a midlatitude summer atmospheric profile. Cirrus mid-cloud heights are shown by the various lines (see inserted legend).

atmospheric emission,  $I_{bc}$ . Another notable feature in both figures is that the error is also dependent upon the height of the cirrus cloud. With higher cloud bases, there is more atmosphere between the cloud and the IR radiometer. This increases the value  $I_{bc}$  and thus emittance errors become more susceptible to errors in  $I_{bc}$ .

In each atmospheric profile, errors were estimated for a range of cirrus cloud heights. In the summer at midlatitudes, typical cirrus clouds heights may range from 7-13 km. In a colder US Standard profile, typical cirrus cloud heights may range from around 6-9 km. In a subarctic winter atmosphere, cirrus clouds could be expected to range from 5-8 km. Emittance errors in the MLS profile were around 13% for high thin cirrus clouds ( $\epsilon = 0.05$ ) and less than 1% for optically thick cirrus clouds ( $\epsilon > 0.75$ ). Although cirrus cloud emittances are highly variable, studies have shown that mean values are in the 0.15-0.50 range (Platt, 1979). Error in this range of emittances for a MLS profile were between 1% and 4%.

Emittance errors in the USS profile, which is colder and has lower cloud heights, were somewhat smaller. Errors for high thin cirrus clouds were as high as 11%, whereas errors for optically thick clouds were less than 1%. Error estimates for typical cirrus cloud emittance were between 2% and 3%.

Emittance errors in the very cold and dry SAW profile reached only 6% at  $\epsilon = 0.05$  and were less than 0.25% for optically thick clouds. In the typical cirrus cloud emittance range, the errors were 0.20 - 1.5%.

A close comparison of the 7-km curves for MLS, USS, and SAW profiles shows that the errors are not only dependent on cloud height and emittance, but also the absorption/emission of the intervening atmosphere. Both the MLS and USS 7-km error curves are similar for optically thick cirrus clouds. For thinner clouds ( $\epsilon < 0.2$ ), however, the 7-km MLS cirrus cloud yielded errors from 2.0%-8.7%, while the USS cirrus yielded errors from 2.0% to 7.6%. The 7-km SAW cirrus cloud had emittance errors of only up to 5.6%. This clearly illustrates that the CKD model (or any such model, for that matter)

has the most difficulty calculating emittances for high thin cirrus clouds in warm moist atmospheres. Given the experimental error encountered when remotely sensing high thin cirrus clouds in highly absorbing atmospheres, these rather large errors seem of almost no great importance. This is another reason large volumes of cirrus data are needed in order to statistically estimate cirrus cloud emittances in a climatological sense.

## 5.6 G Resolution Sensitivity Test

The purpose of this study was not just to develop a method to accurately model atmospheric absorption and emission in the atmospheric window. The LBL model is well suited for that purpose. The model was also needed to compute the quantities economically. The results just presented show that the CKD model is accurate, but how efficient is it?

The major factor in the speed and accuracy of the CKD model is the  $g$  resolution. The more  $g$  values the CKD model incorporates, the more accurately it represents the true absorption spectrum. On the other hand, the computational time increases linearly with the addition of more  $g$  values. This factor is multiplied by the number of different absorbing gases in the wavenumber range of interest. The accuracy needed and time constraints of the user dictate what  $\Delta g$  resolution is used when running the CKD model.

The proper way to choose an optimal  $\Delta g$  resolution would be to decide upon a maximum allowable error. The  $g$  resolution would then be reduced with each model run until those error limits were exceeded. This would reveal the optimum  $\Delta g$  resolution. Unfortunately due to time constraints, a proper experiment of this sort could not be performed. A large amount of time is expended in generating the  $k(g)$  values in the first place. Instead, three different  $\Delta g$  resolutions were chosen, and their accuracy and computational speed were compared to determine which was the most appropriate for use in the LIRAD method. The results of this sensitivity test follow.



In the test, three different  $g$  resolutions were used. In all three cases, a low resolution was used at  $g < 0.9$  and a higher resolution was used at  $g > 0.9$ . The three resolutions were labeled low, medium, and high and are shown at the bottom of Table 5.5. Downwelling radiance from 10 and 30 km was calculated and compared to the LBL model results in column one. Since the LBL model was used as a basis for comparison, the errors in column one are naturally 0%. The relative speeds were calculated by dividing the LBL model run time by the corresponding CKD model run time. In other words the relative speed indicates how many times faster the CKD model ran than the LBL model. For instance, in the mid-latitude summer, 10 km, medium resolution case, the CKD model ran 111 times faster than the LBL model with an error of only 0.96%.

Table 5.5 shows that there is indeed a significant saving of time using the CKD model. The high resolution CKD model calculated the downwelling radiance 30 to 100 times faster than the LBL model with little loss in accuracy. Even the medium resolution model still calculated the radiance to within one percent while running up to 300 times faster. The MLS low resolution showed a significant degradation of accuracy while running only about 55% faster than the medium resolution model. It appears that at least for a MLS type atmosphere, the medium resolution model could be used if the time constraints warrant a model faster than the high resolution version.

The subarctic winter sensitivity test produced considerably less desirable results in the medium and low resolution versions. This is not unexpected since the CKD model was tuned to perform better in midlatitude environments. The 6 to 10% errors resulting from the medium resolution model are probably not worth the savings in time over the high resolution run. The 10-25% errors of the low resolution run are most certainly unacceptable. One should keep in mind, however, the results shown in the previous section. The emittance errors are much less sensitive to downwelling radiance errors in the SAW profile than in the MLS profile.

Table 5.5

## Delta G Resolution Sensitivity Test

	LBL Model	High	CKD Resolution Medium	Low
Midlatitude Summer Profile				
10 km Error	0.0%	0.44%	0.96%	2.65%
Speed	1	32.6	111.0	172.0
30 km Error	0.0%	0.08%	0.59%	2.40%
Speed	1	93.9	333.1	519.2
Subarctic Winter Profile				
10 km Error	0.0%	2.87%	10.62%	25.70%
Speed	1	13.73	102.3	158.5
30 km Error	0.0%	1.19%	6.00%	17.31%
Speed	1	87.4	294.5	454.7
Note:				
Resolution:	$0 < g < 0.9$	$0.9 < g < 1.0$	# of points	
High	0.05	0.001	119	
Medium	0.05	0.01	29	
Low	0.10	0.02	15	

## 5.7 Height Resolution Sensitivity Test

Another significant consideration when weighing the computational gain versus accuracy is the height resolution of the model. In this sensitivity test, the CKD model was run at three different height resolutions to calculate downwelling radiance from 10 and 30 km. In each test, the high  $\Delta g$  resolution as shown in Table 5.6 was used. The only standard atmospheric profile data available for direct input into the LBL model had 1.0 km resolution, so little would be gained by running it at a height resolution of 0.25 km. So testing was done by running the CKD model at 0.25, 0.5 and 1.0 km resolutions. The high resolution run was taken as the standard of comparison, and the medium and low resolution runs were compared to that.

Table 5.6 shows the errors and CPU run times for each resolution at 10 km and 30 km. Decreasing the resolution from 0.25 to 0.50 km resolution resulted in a 45-50% savings in computational effort. The ensuing errors were less than 1%. Decreasing the

Table 5.6

### Height Resolution Sensitivity Test

Subarctic Winter Profile			
	0.25 km	Z Resolution 0.50 km	1.00 km
10 km Error	0.00%	-0.85%	-2.56%
CPU Time	33.36	18.62	14.55
30 km Error	0.00%	-0.59%	-1.64%
CPU Time	77.03	38.08	28.03

Note: High G Resolution (119 points)  
Vertical Data Resolution - 0.25 km

resolution to 1.0 km, resulted in a 56 to 64% savings in CPU time. The resulting errors were in the 1.5-2.5% range. For the purposes of this LIRAD study, a higher accuracy of the 0.25 km resolution is probably worth doubling the cost of CPU time. Once the LIRAD experiment is fully designed, and the operational constraints better known, a more educated decision can be made on this issue.

### 5.8 Above Cloud Contributions to Downwelling Radiance

In anticipation of further work on this project, one final experiment was conducted to discern whether or not above-cloud-base downwelling emission should be considered in the LIRAD studies. Recall that Platt and colleagues in their studies neglected any clear sky radiance above the cloud base when determining cloud radiance. This greatly simplified the calculation of  $I_c$  in Eq. (1.1), reducing the solution to:

$$I_c = (I_m - I_{sr} T_{bc} - I_{bc}) / T_{bc} . \quad (5.6)$$

It is not really possible to determine with certainty whether or not the above-cloud-base clear sky radiance can be neglected or not without actually inserting a cloud into the model. After all, some of that above-cloud radiance would be absorbed by the cloud itself. As of now, cloud properties have not been included in the model. However, a simple experiment was performed using the LBL model which provides some insight into this question.

With the IR radiometer filter included, the LBL model was first run looking from the surface up to 50 km for several different standard atmospheric profiles. Next, this process was repeated for the same profiles but looking up to levels ranging from 6 to 12 km, typical cirrus cloud heights. The radiances for the various cirrus cloud heights were compared to the radiances looking to 50 km to determine the percentage of downwelling radiance being emitted from each cloud level:

$$\text{Above Cloud Percent} = \frac{\text{Radiance (50 km)} - \text{Radiance (cloud level)}}{\text{Radiance (50 km)}} \times 100. \quad (5.7)$$

The above cloud contributions for several different profiles are shown in Fig. 5.8. As expected the largest above cloud contribution occurred in the SAW and USS profiles where ozone is most abundant. In these profiles clouds are generally lower too, which contributes even more to the above cloud contribution. Figure 5.8 shows that for a very thin cirrus cloud in a subarctic winter environment, above cloud emittance could account for as much as half of the total downwelling radiance! Certainly, it would be foolish to neglect this component. Even in a US Standard atmospheric profile, above cloud emission could contribute as much as 20% of the total. For warm moist environments such as the TRO and MLS profiles, the above-cloud emission accounted for only 5-10% of the total. In these conditions it might be appropriate to neglect downwelling emission from above the cirrus cloud base. The results of this experiment show that some sort of parameterization will be necessary to account for the above-cloud downwelling radiance contributions.

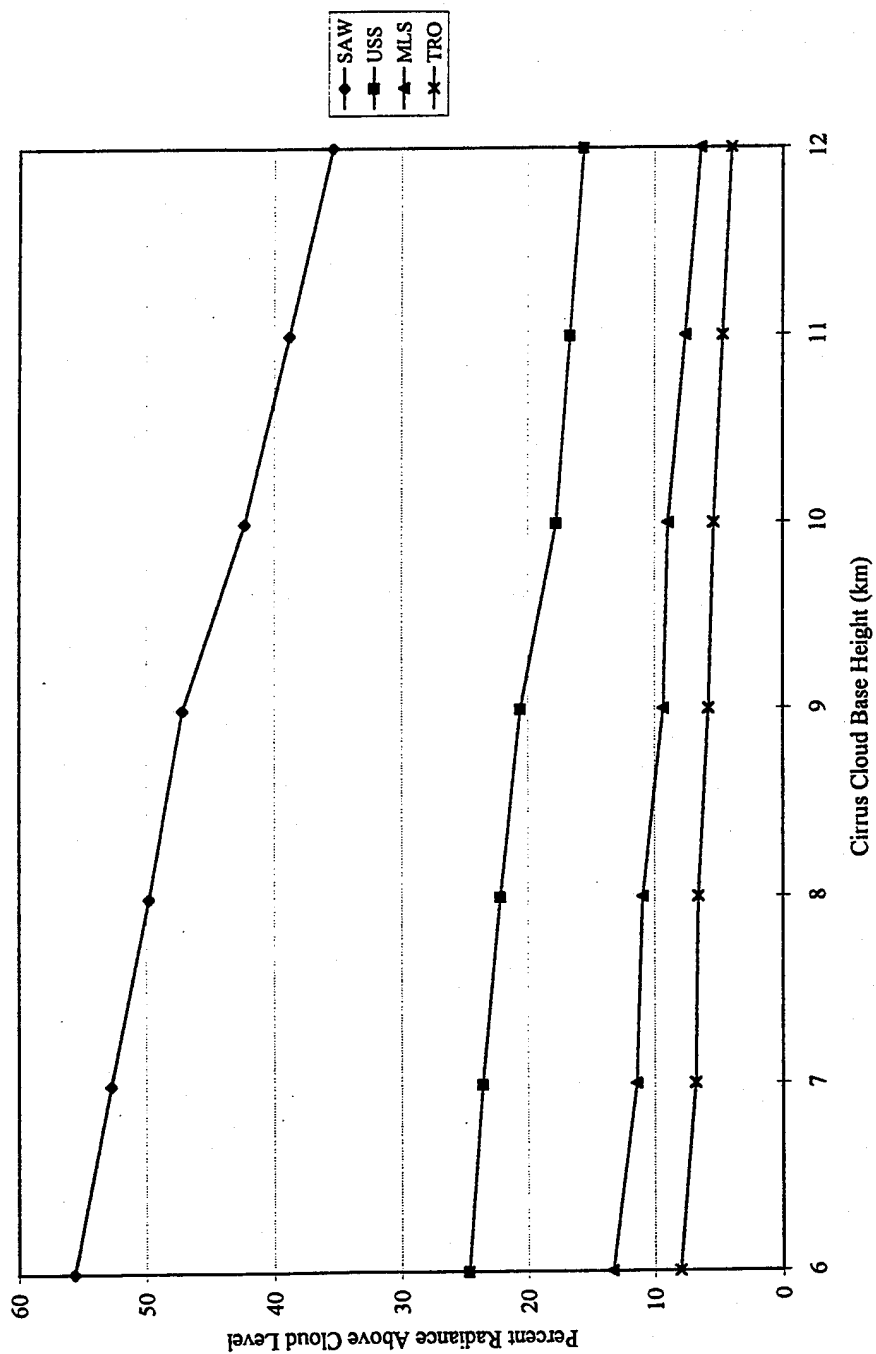


Figure 5.8. Contribution of downwelling vertical radiance form above cirrus cloud base for several different atmospheric profiles. Contributions are in percentage of total downwelling vertical radiance.

## CHAPTER 6

### CONCLUSIONS

This thesis has presented an efficient radiative transfer scheme that was used to calculate downwelling and upwelling infrared radiance in the window region of the infrared spectrum. This work, however, is only the beginning of a model that will include cirrus cloud scattering phase functions, and that will be used to interpret infrared radiometer observations. These observations have been taken as part of an experiment that will eventually lead to the determination of emittances for various types of cirrus clouds. In this thesis, the method of measuring the emittances was discussed. This LIRAD method was devised by C.M.R. Platt and colleagues over 25 years ago, but it remains valid and important in a time of growing concern over the earth's climate.

The FARS CKD model utilized the correlated k-distribution method to calculate transmittance functions. Although not widely used as a means of dealing with radiative transfer in nonhomogeneous atmospheres, the CKD method has been proven by Goody et al. (1989), Lacis and Oinas (1991), Fu (1991) and others, to be a useful substitute to other band models, particularly in the ozone band. This study has reinforced the usefulness of the CKD method. With the exception of the tropical environment, the CKD model calculated by the transmittance functions to within 0.5% of the popular and highly accurate FASCOD3P line-by-line model. Even the tropical environment had errors of less than 2% at all altitudes up to 30 km.

Applying these transmittance functions to a radiative transfer scheme again produced excellent results. The model calculated downwelling radiances to within 2% of the LBL model for all altitudes up to 30 km, the model ceiling. The only exception to this

was the subarctic winter atmosphere, where errors reached 8% in the lower troposphere, but rapidly tapered off to around 1% at the model ceiling. Much of this error was due to the Planck function approximation necessitated by the wide bandwidth of the radiometer and the use of the CKD method g-space substitution for  $\nu$  space.

A test of the FARS CKD model emittance accuracy also provided encouraging results. The model was able to calculate emittances with less than 1% error for optically thick clouds and less than 12-15% for very high thin cirrus clouds. The only exception here was for high thin cirrus clouds in a tropical environment, where errors were significantly larger.

The FARS CKD model maintained this high degree of accuracy while running over 100 times faster than the FASCOD3P LBL model. When further optimization tests are run, the speed should increase even more.

This study also produced results that may lead to significant improvements over previous LIRAD studies. The significant emission contributions from carbon dioxide and particularly ozone proved that models calculating cirrus cloud emittances in the IR window may have to include these two gases. Ozone proved to be the dominant emitter in the colder and drier atmospheres near the poles. The experiment described at the end of Chapter 5 showed that emission from above cirrus cloud bases should also be included when calculating clear sky contributions to radiance measured by the FARS IR radiometer. For colder and drier environments, when only thin cirrus clouds are overhead, this component could be responsible for as much as 50% of the measured downwelling radiance.

Before this FARS CKD model can be completely used in the LIRAD study, many more milestones must be passed. First, the radiometer filter function must be included in all aspects. This will be challenging, since the g space versus  $\nu$  space must be dealt with as in the Planck function. Next the model will need to be optimized for vertical and g-space resolution. A more sophisticated radiative transfer approach may even be necessary.



The model will then need to be tested against the LBL model using actual soundings and clear sky radiance measurements from the FARS PRT-5 radiometer. Considering the arid and sometimes cold environment in which many of the radiometer observations are taken, it would be prudent to determine if and how aerosols may contribute to the total radiance. Including the aerosols in the model, would present an interesting challenge since aerosols are highly variable in time and space and not measured at the FARS facility. During intensive observation periods such as the ARM RCS IOP at Lamont, OK, in 1994, detailed aerosol measurements and soundings were taken. Data from these field experiments may prove to be most valuable. Once all of these tasks are accomplished, a cloud model can be added.

The backscattered radiance from cirrus clouds is a secondary but important contributor to the IR radiometers measured downwelling radiance. But it is still an important contributor. These aerosol and backscatter factors will need to be weighed when adding the cloud effects to the overall model. Will an accurate but very time consuming scattering scheme be necessary, or will a relatively simple phase function be satisfactory? In addition to this issue, the above-cloud clear sky emittance will need to be parameterized somehow.

Much still lies ahead before the FARS CKD model can be used to help calculate downwelling cloud radiance for the FARS IR radiometer, but this study has taken a significant step towards reaching this goal.

## REFERENCES

- Anderson, G.P. et. al, 1986: AFGL atmospheric constituent profiles (0-120km). AFGL Technical Reference-86-0110.
- Chou, M. and L. Kouvaris, 1986: Monochromatic calculations of atmospheric radiative transfer due to molecular line absorption. *J. Geophys. Res.*, **91**, 4047-4055.
- Clough, S. A., F. X. Kneizys, L. Rothman, and W. Gallery, 1981: Atmospheric spectral transmittance and radiance: FASCOD1B. *Soc. of Photo-Optical Eng.*, **277**, 152-166.
- Clough, S. A., F. X. Kneizys, E. Shettle, and G. Anderson, 1986: Atmospheric radiance and transmittance: FASCOD2. *Preprints Sixth Conf. Atmospheric Radiation*, Williamsburg, Amer. Meteor. Soc., 141-144.
- Clough, S. A., et al., 1988: FASCOD3: Spectral simulation. *Preprints Current Problems Atmospheric Radiation*, DEEPAK Publishing, 372-375.
- Davis, P. A.: The analysis of lidar signatures of cirrus clouds. *Appl. Opt.*, **8**, 2099-2102.
- Fu, Q., 1991: Parameterization of radiative processes in vertically nonhomogeneous multiple scattering atmospheres. Ph.D. Dissertation, University of Utah, 259 pp.
- Fu, Q. and K.N. Liou, 1992: On the correlated k-distribution method for radiative transfer in nonhomogeneous atmospheres. *J. Atmos. Sci.*, **49**, 2139-2156.
- Gallery, W.O., F. X. Kneizys, and S. A. Clough, 1983: Air mass computer program for atmospheric transmittance/radiance calculation: FSCATM. AFGL Technical Reference-83-0065.
- Goody, R., R. West, L. Chen, and D. Crisp, 1989: The correlated k-distribution method for radiation calculations in nonhomogeneous atmospheres. *J. Quant. Spectrosc. Radiat. Transfer*, **42**, 539-550.
- Herman, G., M. C. Wu, and W. Johnson, 1980: The effect of clouds on the earth's solar and infrared radiation budgets. *J. Atmos. Sci.*, **37**, 1251-1261.

- Lacis, O. A., W. C. Wang, and J. Hansen, 1979: Correlated k-distribution method for radiative transfer in climate models: Application to effect of cirrus clouds on climate. *NASA Conf. Publ.*, 2076.
- Lacis, A. and V. Oinas, 1991: A description of the correlated k-distribution method for modeling nongray gaseous absorption, thermal emission, and multiple scattering in vertically inhomogeneous atmospheres. *J. Geophys. Res.*, **96**, 9027-9063.
- Liou, K. N., 1980: *An Introduction to Atmospheric Radiation*. Academic Press, 404 pp.
- Liou, K. N., 1986: Influence of cirrus clouds on weather and climate processes: a global perspective. *Mon. Wea. Rev.*, **114**, 1167-1197.
- Liou, K. N., 1992: *Radiation and Cloud Processes in the Atmosphere*. Oxford Univ. Press, 487 pp.
- Platt, C. M. R., and D. J. Gambling, 1971: Emissivity of high layer clouds by combined lidar and radiometric techniques. *Quart. J. Roy. Met. Soc.*, **97**, 322-325.
- Platt, C. M. R., 1973: Lidar and radiometric observations of cirrus clouds. *J. Atmos. Sci.*, **30**, 1191-1204.
- Platt, C. M. R., 1979: Remote sounding of high clouds: I. Calculation of visible and infrared optical properties from lidar and radiometer measurements. *J. App. Meteor.*, **18**, 1130-1143.
- Platt, C. M. R., and A. C. Dilley, 1979: Remote sounding of high clouds II: emissivity of cirrostratus. *J. App. Meteor.*, **18**, 1144-1150.
- Platt, C. M. R., and G. L. Stephens, 1980: The interpretation of remotely sensed high cloud emittances. *J. Atmos. Sci.*, **37**, 2314-2322.
- Platt, C. M. R., 1981: Remote sensing of high clouds III: monte carlo calculations of multiple-scattered lidar returns. *J. Atmos. Sci.*, **38**, 156-167.
- Platt, C. M. R. and A. C. Dilley, 1981: Remote sounding of high clouds IV: Observed temperature variations in cirrus optical properties. *J. Atmos. Sci.*, **38**, 1069-1082.
- Platt, C. M. R., J. Scott, and A. C. Dilley, 1987: Remote sounding of high clouds VI: Optical properties of midlatitude and tropical cirrus. *J. Atmos. Sci.*, **44**, 729-747.
- Roberts, R., J. Selby, and L. Biberman, 1976: Infrared continuum absorption by atmospheric water vapor in the 8-12  $\mu\text{m}$  window. *J. Appl. Opt.*, **15**, 2065-2069.

Sassen, K., 1991: The polarization lidar technique for cloud research: a review and current assessment. *Bull. Amer. Met. Soc.*, **72**, 1848-1862.

Sassen, K., and B. S. Cho, 1992: Subvisual-thin cirrus lidar dataset for satellite verification and climatological research. *J. Appl. Meteor.*, **31**, 1275-1285.

Wang, W. and P. B. Ryan, 1983: Overlapping effect of atmospheric  $H_2O$ ,  $CO_2$ , and  $O_3$  on the  $CO_2$  radiative effect. *Tellus*, **35B**, 81-91.

West, R. D., D. Crisp, and L. Chen, 1990: Mapping transformations for broadband atmospheric radiation calculations. *J. Quant. Spectrosc. Radiat. Transfer*, **43**, 191-199.